

UNIVERSITÀ DEGLI STUDI DI MODENA E REGGIO EMILIA

DOTTORATO DI RICERCA IN FISICA

SCUOLA DI DOTTORATO: PHYSICS AND NANOSCIENCES

XXVII Ciclo

TESI PER IL CONSEGUIMENTO DEL TITOLO DI DOTTORE DI RICERCA

Coupling metals with zinc oxide:
structure, morphology
and optical properties

Candidata:

Ilaria Valenti

Relatore:

Prof. Sergio Valeri

Correlatore:

Dott. Stefania Benedetti

Direttore della Scuola di Dottorato:

Prof. Marco Affronte

*"Non il possesso della conoscenza,
della verità irrefutabile,
fa l'uomo di scienza,
ma la ricerca critica,
persistente e inquieta."*

Karl Popper,
Logica della scoperta scientifica

Ad Alessandro

A Mia Madre

A Mio Padre

Contents

| | |
|---|-----------|
| Introduction | 1 |
| 1 Metal-ZnO systems for solar energy conversion | 5 |
| 1.1 Zinc oxide | 7 |
| 1.2 Plasmonics in metal nanoparticles | 14 |
| 2 ZnO thin films on Mo(001) | 21 |
| 2.1 ZnO thin films | 21 |
| 2.2 Experiments @SESAMo Laboratory | 25 |
| 2.3 Film composition and growth | 28 |
| 2.3.1 Modeling of film growth | 30 |
| 2.3.2 Modification of oxidizing conditions | 31 |
| 2.4 Film defectivity | 33 |
| 2.5 Crystalline structure | 35 |
| 2.6 Conclusions | 37 |
| 3 Al-doped ZnO films | 39 |
| 3.1 Al-doped ZnO as a TCO material | 40 |
| 3.1.1 The quest for best performances | 45 |
| 3.1.2 Unraveling conduction mechanism | 51 |
| 3.2 Al-doped ZnO as an alternative plasmonic material | 56 |
| 3.2.1 Infrared analysis @Elettra Synchrotron | 58 |
| 3.2.2 Optoelectronic properties | 62 |
| 3.3 Conclusions | 66 |
| 4 Ag NP/Oxides | 69 |
| 4.1 Ag/ZrO ₂ : a case study for morphological analysis | 70 |
| 4.1.1 Experimental apparatus @IAP Tu-Wien | 72 |
| 4.1.2 STM analysis procedure | 72 |
| 4.1.3 Morphology and structure | 82 |

| | | |
|-------|---|------------|
| 4.2 | Ag/MgO | 86 |
| 4.2.1 | Electron-Energy Loss Spectroscopy | 89 |
| 4.2.2 | Growth of Ag NP on MgO | 92 |
| 4.2.3 | The role of temperature | 104 |
| 4.2.4 | Fe/MgO as a template to grow Ag NPs | 106 |
| 4.3 | Ag/ZnO | 109 |
| 4.3.1 | Growth of Ag NP on ZnO | 110 |
| 4.3.2 | The role of temperature | 118 |
| 4.4 | Conclusions | 121 |
| | Conclusions | 122 |
| | Bibliography | 124 |
| | Acknowledgements | 134 |
| | Curriculum and list of publications | 137 |

Introduction

The exploitation of sustainable energy sources is one of the most challenging topics in latest research, due to the increasing energy requirements and rising prices of fossil-based fuels, so far as the required low environmental impact. The quest for new and more efficient renewable and sustainable energy supplies has become a major issue in present scientific research, which affects all fields of study, from Physics, to Chemistry and Engineering.

In the past decades, the powerful connubium created in metal-oxide systems has risen more and more interest, thanks to the applications in a vaste variety of fields, including energy production and storage. Many devices have been developed, which exploit the association of a metal and an oxide, such as photovoltaic cells (inorganic, organic and dye-sensitized solar cells), electrochemical energy conversion (solid oxide fuel cells) and storage devices (lithium-ion batteries and supercapacitors). Nanostructured metal-oxide systems, in particular, have proved to show peculiar properties, which arise at the nanoscale and can improve the performances of various devices. Most of the fundamental processes involved in these devices take place at the surface or, more generally, at the interface between different materials. Due to the break of symmetry induced by the presence of the interface, properties of surface atoms are quite different to the bulk ones, since they are related to the number of neighbours to which each atom can bond and interact. In nanostructures, where surface-to-volume ratio is large, size-dependent properties become particularly significant. Size effects can be either surface effects, quantum confinement effects, plasmon resonances or superparamagnetism. It has to be noted that in common language "nanostructures" or "nanoscale" refers to the size range between 1 and 100 nm, but a more correct definition would take as a reference the size at which peculiar properties show up, which means when diameter of nanoparticles is of the same order of magnitude of the exciting wavelength.

The coupling of a metal with an oxide can present different forms. Metal material can act as a substrate to deposit oxide film to investigate growth mechanism of the latter and the processes occurring at the interface; vice versa, the focus moves to metallic properties, such as plasmonic properties, when the oxide is the substrate where metal nanoparticles (NP) are grown. A third possibility is to use metal as a dopant for the oxide, which deeply changes not only chemical, but also optoelectronic and electrical material properties.

This work investigates different systems, where the coupling of a metal and a particular oxide, zinc oxide (ZnO), promotes the rising of interesting properties with application in energy conversion devices and in various other fields. The associations of zinc oxide in different form: sub-nanometer thin film, mesoscopic film and bulk crystal, with different metals as a substrate, dopant and nanoparticles deposited on the surface has been studied with a variety of techniques for a deeper comprehension both of the fundamental processes involved and the improvement of devices performances.

The study opens with a brief introduction concerning metal-oxide systems applications in solar energy production and the description of a recently developed new generation of solar cells, the Dye-Sensitized Solar Cell (DSSC). The motivation of the choice of zinc oxide-based metal-oxide systems is given with the description of ZnO crystal structure. The second part of the chapter is focused on metal NPs plasmonic properties, arising from the association of metal clusters with an oxide substrate, which can enhance the performances of many energy-related devices. Plasmonic response strongly depend on morphology and geometry of the particles, thus the influence of single parameters on the optical response has been discussed, followed by a short description of possible applications.

In Chapter 2 the study of ZnO in the form of a thin film deposited on a molibdenum single crystal is presented. The film, prepared and analyzed in Ultra-High Vacuum (UHV) represents a model system to investigate the first stages of growth of the oxide in a controlled environment and to determine the influence of different parameters on morphological, chemical and structural properties. After a short state of the art concerning ZnO thin films grown on different substrates and the description of the experimental apparatus at the University of Modena and Reggio Emilia, where most of the analysis described in this work have been performed, results are discussed. ZnO/Mo system has been probed by means of Scanning Tunneling Microscopy (STM), X-ray Photoemission Spectroscopy (XPS), Low-Energy Electron Diffraction (LEED) and X-Ray Diffraction (XRD), and a deep analysis of film growth, defectivity and structure has been conducted.

In Chapter 3 the focus moves to a different metal-ZnO system, where metal acts as a dopant for the oxide: Al-doped ZnO (AZO) films grown on MgO by magnetron sputtering. In this case the preparation technique chosen is a scalable one, which allows to get close to the real device. The possibility to use AZO both as a promising component of solar cells and optoelectronic devices, as a transparent conductive oxide (TCO) and as an alternative plasmonic materials to noble metal is discussed in Sec.3.1 and 3.2, respectively. AZO films in a wide doping range (0-14 at.%) have been grown and analyzed by means of a variety of techniques, not only to determine best performances of the material as a function of Al content, but also to relate all the different properties and obtain a complete picture of the system. A relevant part of the study, presented in Sec.3.1.2, is dedicated to enlighten the conduction mechanism, which is still debated despite the vaste number

of studies performed on AZO: electronic properties have been analyzed by means of XPS and Hard X-ray PhotoEmission Spectroscopy (HAXPES). The second section focuses on plasmonic properties of Al-doped ZnO, investigated with InfraRed (IR) measurement. The last part of the work is dedicated to the coupling of silver NPs, with zinc oxide, focusing on the optical response of the system and how it is related to morphological properties. For a better understanding of this complex system, Ag NPs have also been grown and analyzed on different oxides, to develop a suitable and reliable procedure to determine and inter-relate the different properties. The STM morphological analysis procedure, developed at Vienna University of Technology, is presented in Sec.4.1, with application on Ag/ZrO₂ as a case study. The consolidated experience of the research group at the University of Modena on MgO/Mo has led the choice of this system as a prototypical substrate for the study of Ag NPs self-assembly on the oxide surface and the relation between particle geometry and optical response. The analysis, conducted with STM and Electron Energy-Loss Spectroscopy (EELS) is presented in Sec.4.2, where the modeling of NPs growth from the first stages has been obtained by comparing experimental data with a model simulation of optical response performed with *GranFilm* software. The skills acquired by the study of the Ag/ZrO₂ and Ag/MgO/Mo systems have been exploited in the analysis of Ag/ZnO system, described in Sec.4.3. Growth of silver NPs on the oxide has been modeled both at room temperature (RT) and at 673 K and the effects of temperature by annealing has been investigated, both from morphological, structural, chemical (by XPS) and optical point of view. Finally, overall main conclusions and future perspectives are discussed.

Chapter 1

Metal-ZnO systems for solar energy conversion

Metal-oxide systems have proven to possess suitable properties to be exploited in various fields, particularly in energy conversion. Among the energy sources, solar energy conversion has shown one of the highest potential: the energy from sunlight reaching Earth each hour is more than the energy amount globally consumed in a year. Solar cells are powerful devices, to date reaching almost 45% of conversion efficiency (see Fig.1.1 [1]). However, to obtain such high performances, expensive production procedures and toxic materials are required in most cases.

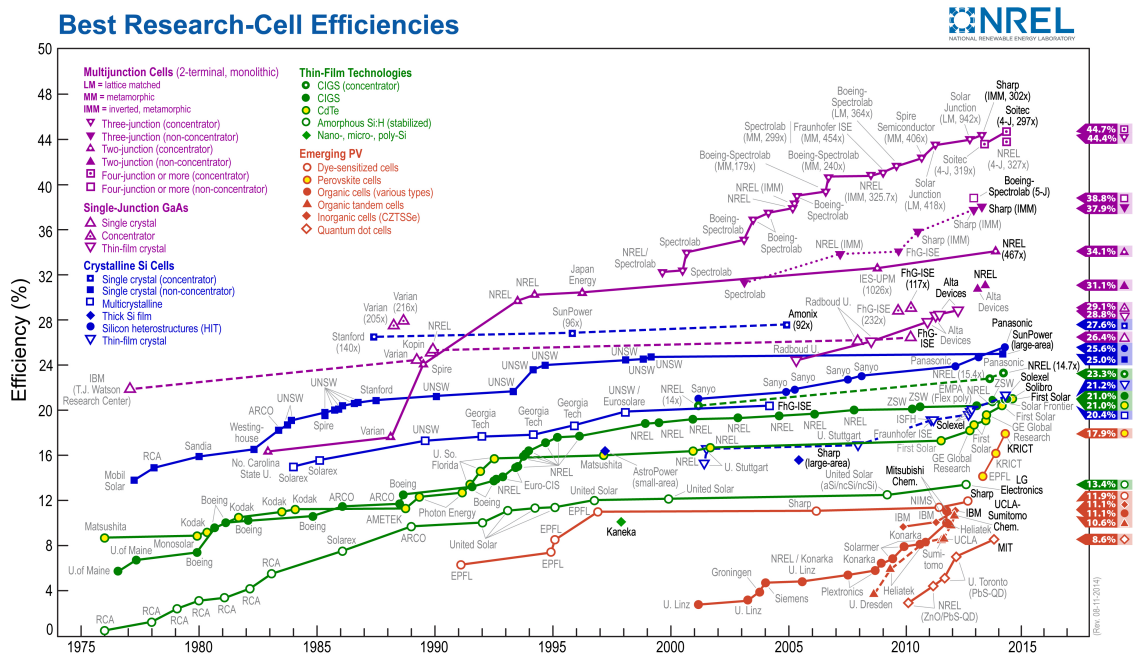


Figure 1.1: Conversion efficiencies of best research solar cells worldwide for various photovoltaic technologies from 1976 to 2014 (11th of August) as tracked by National Renewable Energy Laboratory [1].

To overcome these problems, a different kind of device has been proposed: the Dye-Sensitized Solar Cell (DSSC), which realizes optical absorption and charge separation by association of an organic dye with a wide band gap semiconductor oxide. DSSC cells, also called Grätzel cells, represent promising devices, not only thanks to the lower costs of materials with respect to conventional Si-based solar cells and the use of non-toxic compounds, but also for their light weight, transparency, flexibility and high power conversion efficiencies under cloudy and artificial light conditions.

In DSSC cells (Fig.1.2), when the organic dye is photoexcited by solar radiation, an electron is injected into the semiconducting oxide Conduction Band (CB) and transported to the electrode. The dye is then regenerated by a redox system, usually composed by a liquid electrolyte, and the whole system is in turn regenerated by the electrons closing the circuit. The regeneration of the dye by the redox system is faster than the electron-hole pair recombination, so electrical current is generated [2].

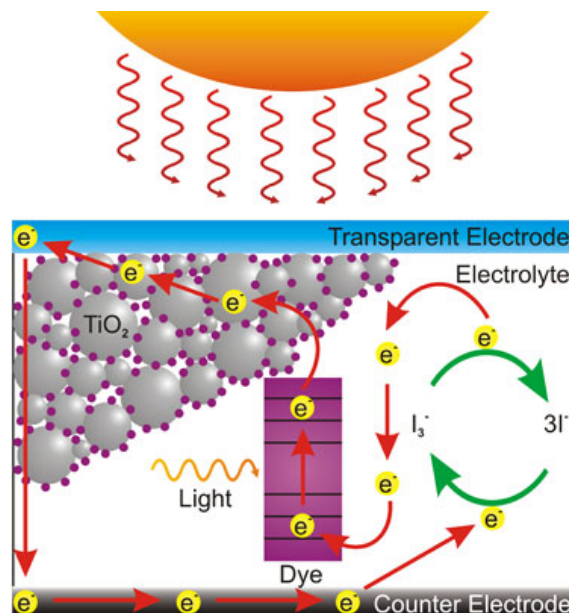


Figure 1.2: *Schematic of the principle of operation of a DSSC.*

The heart of the DSSC is represented by a nanostructured semiconductor oxide film, which has to expose a large surface area, to be stable and to have a high carrier mobility. Best performances have been reached with TiO₂ ($\sim 11\%$ [3]), which has been largely studied, but also ZnO and Nb₂O₅ show suitable properties to this purpose.

The anode of the cell is made of a transparent conductive oxide (TCO), which acts as an ohmic contact for carrier transport and at the same time allows the sunlight to reach the active material. Transparent conductive oxides are metal doped oxides which are widely used not only in DSSC, but also in organic and inorganic photovoltaic devices, surface mount devices and as flat panel display in electronics. For the applications in optoelectronics, high transmittance in the visible range and low resistivity are required.

To date, the best performances have been reached with tin-doped indium oxide (ITO), which represents the present industrial standard. However, the scarcity and consequent high cost and the toxic nature of indium have promoted the search for alternative compounds, which have been found in fluorine doped tin oxide (FTO) and in ZnO doped with IIIA group elements, like Al, Ga and In itself.

Recently, a new type of DSSC has been developed, where a hybrid perovskite acts as a light harvester and an organic hole transport material replaces the cell's liquid electrolyte, thus overcoming the problems related to the difficult assembly of the cell and its consequent short life. With these solid-state DSSC, 15% conversion efficiency was reached in 2013 [4] and further improvements are expected.

The fascinating properties of metal-oxide coupling which find applications in solar power generation are various, in DSSC, for example, they arise from the association of the nanostructured semiconductor oxide film with the metal electrode, but also from the doping of an oxide by a metal creating a TCO. Additionally, metal nanoparticles can be added to the system, introducing plasmonic properties (see Sec.1.2), which strongly improve performances of devices.

1.1 Zinc oxide

ZnO is a wide band gap semiconductor (Eg 3.6 eV at 300 K), with large exciton binding energy (60 meV) and high mobility ($120 \text{ cm}^2/\text{V}$); it is a good thermal and electric conductor and a very stable material. It becomes ferromagnetic when doped with transition metals and a transparent conductive oxide when doped with III group metal. Zinc oxide forms a wide variety of different nanostructures depending on the preparation adopted and it is a common, bio-compatible and inexpensive material. The large amount of ZnO applications include piezoelectric transducers (thanks to its high piezoelectric tensor), space applications (for the high resistance to high energy radiation), catalysis (in methanol synthesis in association with Pd), surface acoustic waves devices, microelectronics and photovoltaics [5].

Thanks to its properties, ZnO has proved to be a promising material for solar energy conversion devices, where it can be used both as nanostructured oxide films and, when doped with III group metals, as TCO. In the first case, ZnO represents a valid alternative to TiO_2 , being the second material for performances and with lower costs and a wide variety of available nanostructures (nanowires, nanotubes, hierarchical nanostructures) with respect to titania. Among transparent conductive oxides, Al-doped ZnO (AZO) is the best candidate to replace ITO, since aluminum and zinc are common, inexpensive and non-toxic materials, the compound is highly stable and has shown valuable properties in term of high transparency, low resistivity and high carrier concentration [6].

ZnO crystal structure

In bulk form ZnO presents a hexagonal wurtzite crystal structure (Fig.1.3), where Zn and O atoms form a hexagonal close-pack (hcp) sublattice. Each atom is tetrahedrally coordinated: each Zn^{2+} ion occupies the center of a tetrahedron on whose vertexes O^{2-} ions are located and vice versa. Tetrahedral coordination is due to the presence of covalent bondings between sp^3 hybrid orbitals, while the strong oxygen electronegativity generates an ionic character in these bondings [5]. In this configuration, lattice parameters are $a = 3.25 \text{ \AA}$ and $c = 5.21 \text{ \AA}$ [7]. Beside the most termodinamically stable phase, the wurtzite, ZnO can also present zincblende form, which can be seen as two compenetrated face centered cubic (fcc) lattices. This form is stable if the crystal is grown on a substrate with cubic symmetry [8]. At very high pressures (10 GPa) ZnO can also assume rocksalt structure, which is also composed by two compenetrated cubic lattices but, differently from zincblende structure, coordination is octahedral [5].

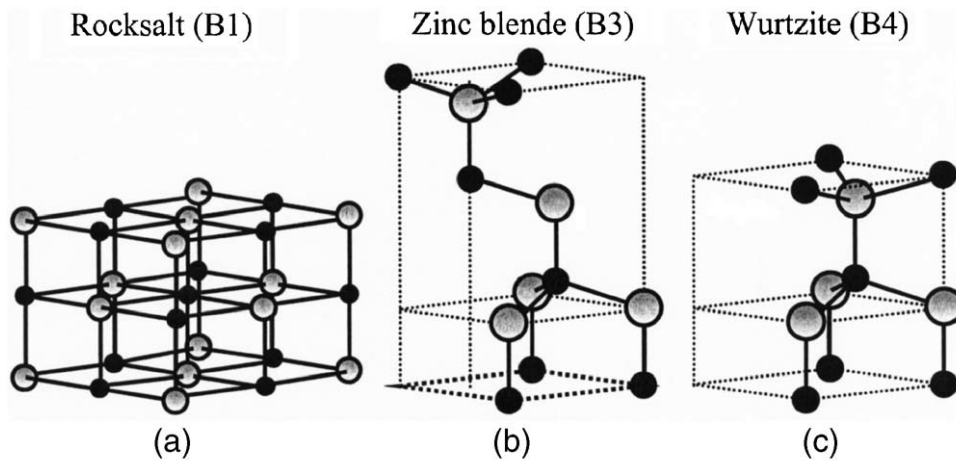


Figure 1.3: Schematic of ZnO crystal structures: (a) cubic rocksalt, (b) cubic zincblende and (c) hexagonal wurtzite. The shaded gray and black spheres denote Zn and O atoms, respectively [5].

ZnO wurtzite structure can be described as a succession of alternate O and Zn planes, perpendicular to the c -axis. The low index surfaces of interest are the non-polar $(10\bar{1}0)$ and $(11\bar{2}0)$ and the polar $(0001)\text{-Zn}$ e $(000\bar{1})\text{-O}$ [Fig.1.4(a)]. Non-polar $(10\bar{1}0)$ and $(11\bar{2}0)$ surfaces (a- and m-planes, respectively) are obtained by breaking the same number of oxygen and zinc bounds, so that each plane contains an equal number of O^{2-} and Zn^{2+} ions; the polar planes (c-planes) are created by cutting the crystal perpendicularly to the c -axis: since wurtzite structure does not show inversion symmetry, the two obtained surfaces are structurally different and can be either O or Zn terminated [Fig.1.4(b)].

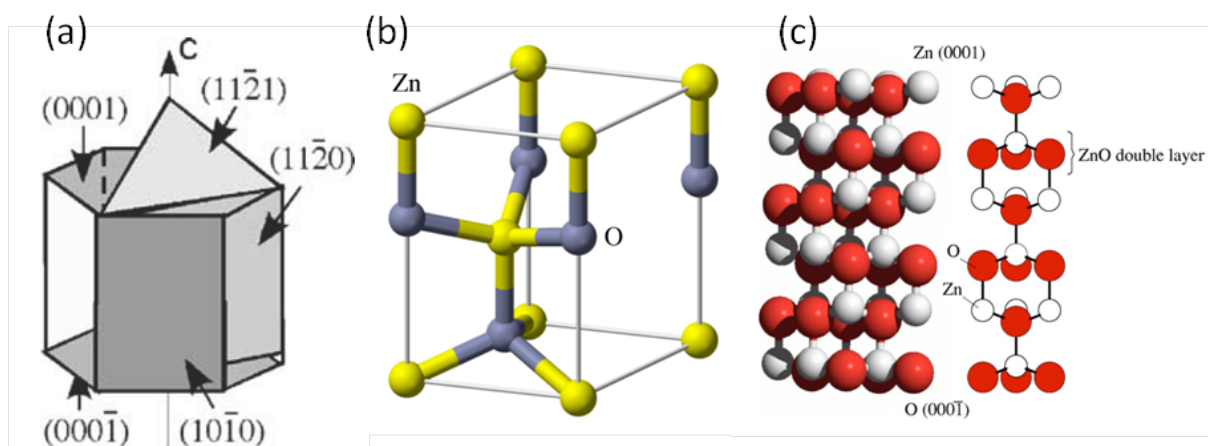


Figure 1.4: Schematic representation of ZnO wurtzite structure. (a) Low index surfaces [9], (b) unit cell and (c) polar surfaces: (0001)-Zn and (000-1)-O [10].

Polar Surfaces: (0001)-Zn and (000-1)-O

Polar surfaces are the most interesting from both fundamental properties and applications point of view and have been largely studied. The most investigated topic is related to their stabilization mechanism. Polar surfaces show the formation of a non-zero dipole moment perpendicular to the surface, thus they should be unstable [11]: the observed stability has been explained for wurtzite structure by a reduction of surface charge by a factor 1/4, which cancels macroscopic dipole [12]. This change in surface charge can be obtained in 3 different ways: through (1) creation of new surface states, (2) adsorption of impurity, like H [12], or (3) removing surface atoms [13]. It is possible to verify surfaces stability by Low-Energy Electron Diffraction (LEED) by the absence of reconstruction pattern [7].

Scanning Tunneling Microscopy (STM) images in Fig.1.5(a) show the morphology of the polar surfaces. (0001)-Zn planes are covered by monoatomic triangular terraces, forming two domains with 180° rotation angle. On the terraces many monoatomic triangular islands and holes are present; cavities on a plane show a rotation of 180° with respect to the upper plane. Both islands and holes are oxygen terminated: the deriving non-stoichiometry stabilizes the polar surface [14]. Morphology of the surfaces can be modified by annealing: increasing temperature, terraces become larger while holes smaller.

(000-1)-O surfaces [Fig.1.5(b)] are characterized by the presence of hexagonal terraces two monolayers high (5.2 \AA), with 120° borders on which both Zn and O atoms are located. No islands or holes have been observed, only occasionally deep and large hexagonal islands are formed ($\sim 170 \div 250 \text{ \AA}$). Terraces borders are stoichiometric: in this case stability derives from H adsorption [15].

Fig.1.5(b) and 1.5(d) show an atomic model compatible with experimental data [7].

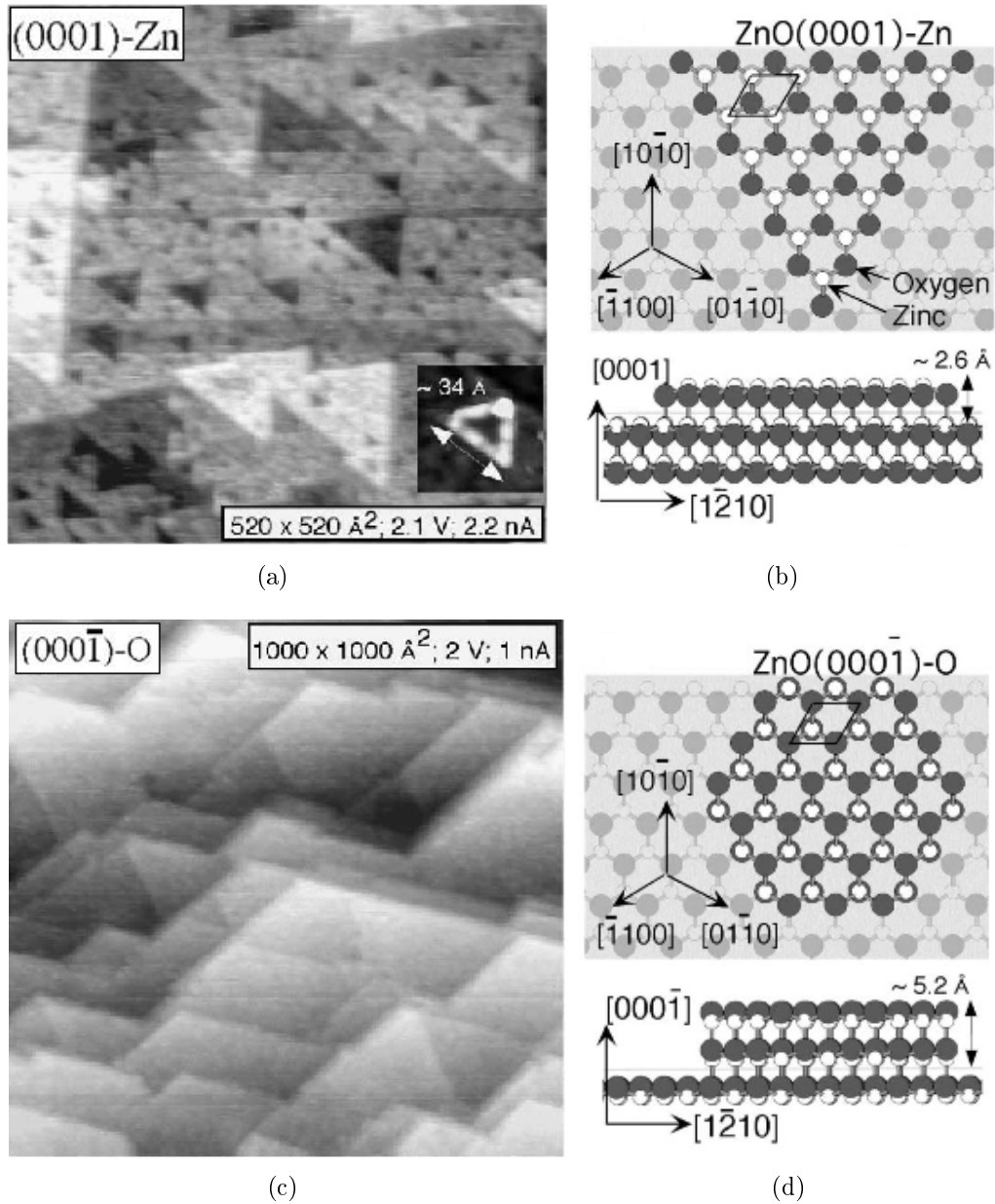


Figure 1.5: (0001) -Zn surface. (a) $(52 \times 52) \text{ nm}^2$ STM image, $(8 \times 8) \text{ nm}^2$ inset shows triangular islands; (b) top and side views of atomic model. $(000\bar{1})$ -O surface. (c) $(100 \times 100) \text{ nm}^2$ STM image and (d) top and side views of atomic model [7].

Non-Polar Surfaces: $(11\bar{2}0)$ and $(10\bar{1}0)$

Zinc oxide applications require in some cases high optical efficiency in quantum well and in-plane piezoelectric effects, which makes a growth along non-polar direction preferable [16, 17]. Besides, non-polar surfaces are preferentially exposed in nanostructures such as nanotubes or nanowires [18] and thus the study of these surfaces is particularly relevant especially for photovoltaic applications where nanostructures are the core of DSSC cells. LEED images in Fig.1.6 report a total absence of reconstruction for these two surfaces, confirming face stability [7].

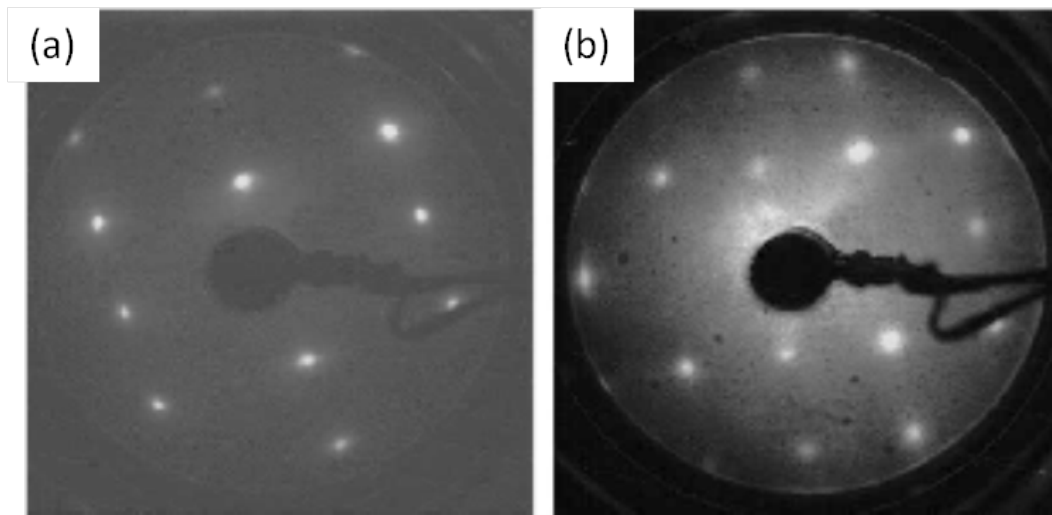


Figure 1.6: *LEED patterns of (a) $(10\bar{1}0)$ and (b) $(11\bar{2}0)$ surfaces, measured at 71 eV and 67 eV, respectively [7].*

A higher roughness for $(11\bar{2}0)$ surface (also called a-plane) is suggested by a higher background intensity and confirmed by STM images (Fig.1.7). Roughness was measured to be 2.5 Å for $(11\bar{2}0)$ plane, 0.7 Å for $(10\bar{1}0)$ and 0.4 Å for the polar ones [7].

$(11\bar{2}0)$ shows large (200-300 Å) and deep (35-65 Å) grooves, aligned along the $[\bar{1}100]$ direction. The borders are parallel to the polar planes (0001) e $(000\bar{1})$ and thus chemically non-equivalent; they form terraces separated by high steps [7, 9].

STM images for $(10\bar{1}0)$ surface (m-plane) report rectangular flat terraces, with 1 monolayer steps along the $[0001]$ or $[\bar{1}2\bar{1}0]$ directions; medium step height of 3 Å is compatible with the vertical separation between two consequent planes 2.6 Å. High resolution images present atomic rows along the $[\bar{1}2\bar{1}0]$ direction, associated to ZnO dimers (Fig.1.8) [7, 19]. $(10\bar{1}0)$ surface is easier to prepare, it shows a lower roughness even at high temperatures and it is very stable: for these reasons it represents a suitable surface to study ZnO as a model system and its interaction with thin films or nanoparticles.

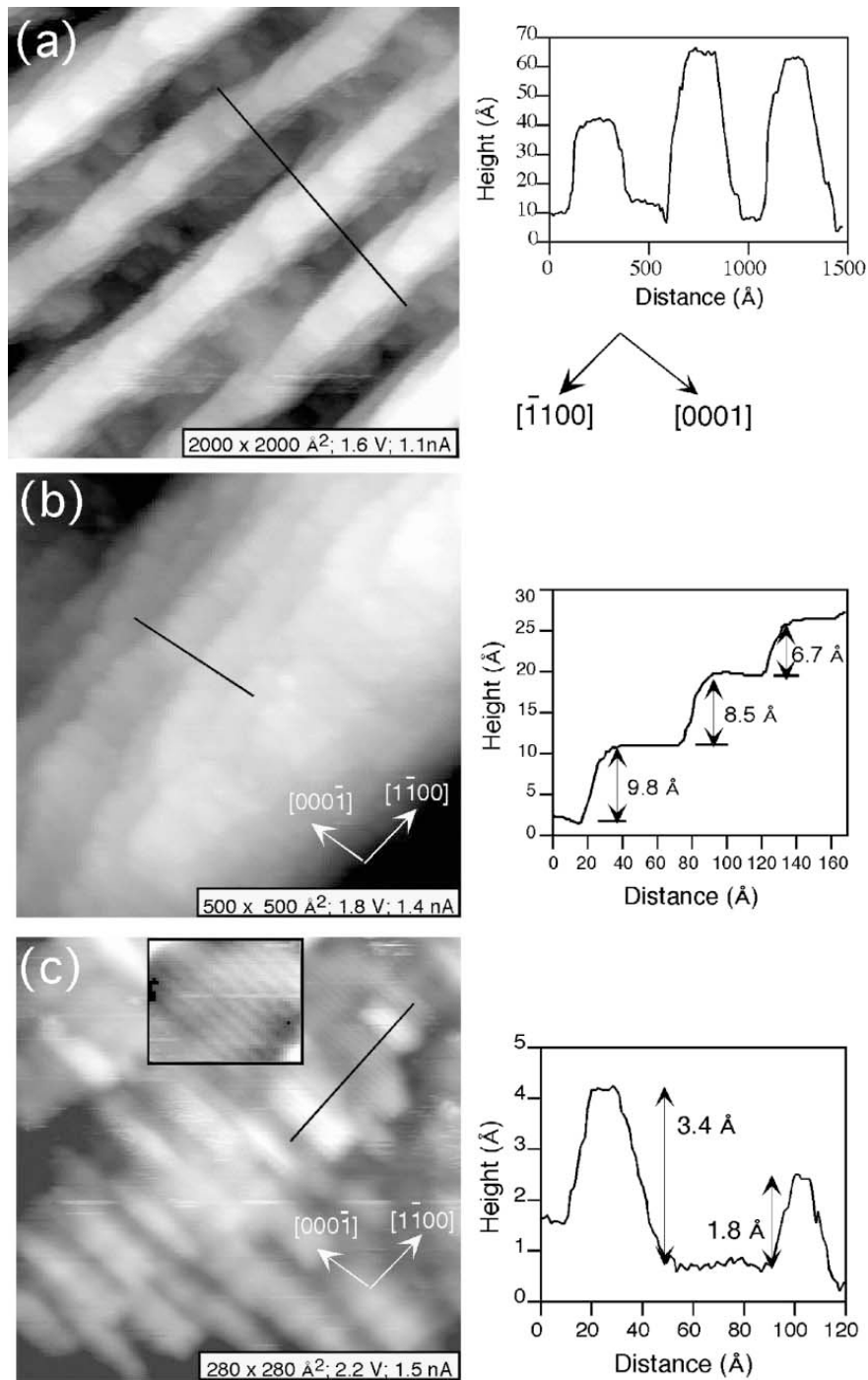


Figure 1.7: *STM images for $(11\bar{2}0)$ surface with corresponding morphological profile. (a) The $(200 \times 200) \text{ nm}^2$ image shows the wide and deep grooves running along $[\bar{1}100]$ direction. (b) Groover borders create terraces as high as many atomic planes. (c) The $(28 \times 28) \text{ nm}^2$ image displays a high density of small terraces along the atomic rows. Inset reports a high resolution image, with atoms along $[0001]$ direction [7].*

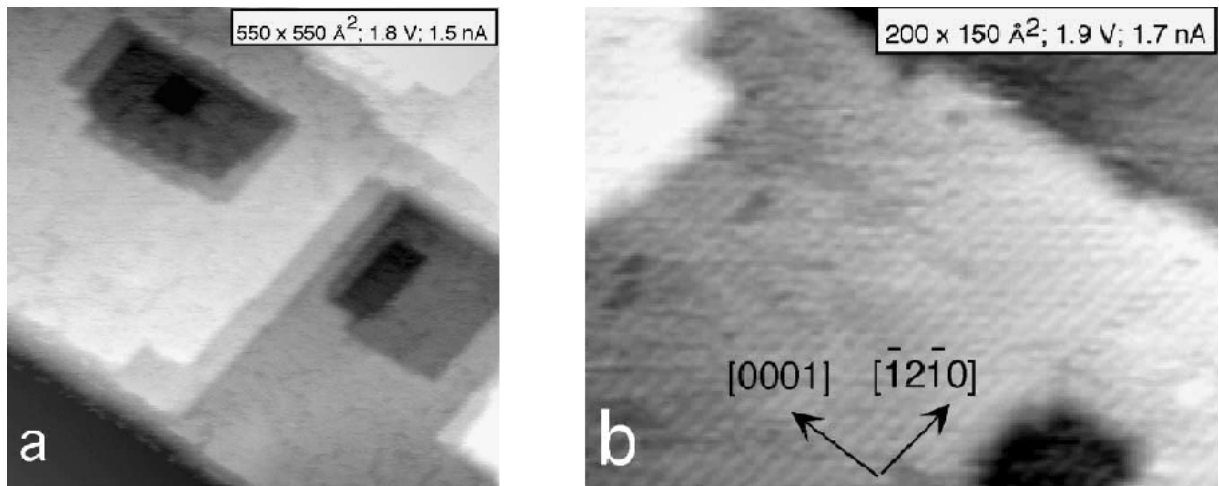


Figure 1.8: *STM images for $(10\bar{1}0)$ surface. (a) (55×55) nm² image shows flat rectangular terraces, separated by one monolayer step height. (b) High resolution image displays atomic rows along $[\bar{1}2\bar{1}0]$ direction [7].*

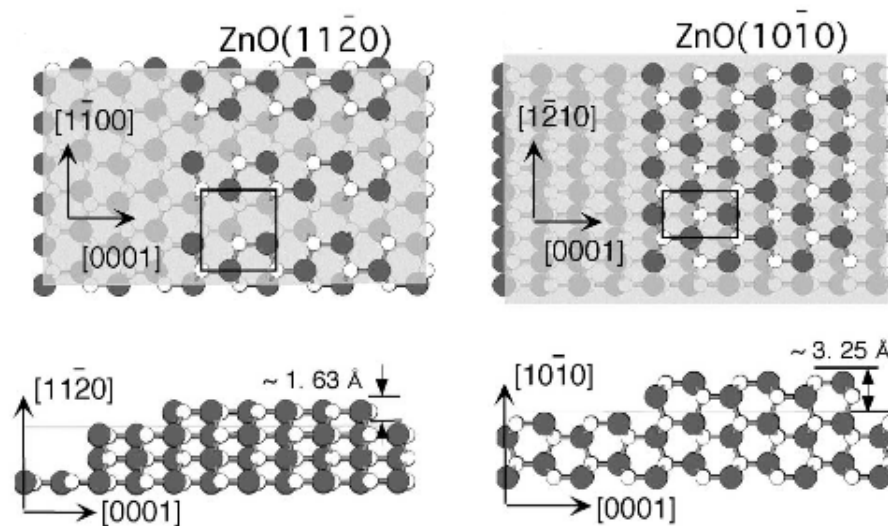


Figure 1.9: *Atomic model for non-polar surfaces $(11\bar{2}0)$ and $(10\bar{1}0)$: top and side view [7].*

1.2 Plasmonics in metal nanoparticles

Metal nanoparticles show peculiar optical properties which significantly differ from the bulk ones, arising from collective oscillations of conduction electrons inside the particles themselves, the Mie plasmons, or Localized Surface Plasmon Resonances (LSPR) [20, 21]. To describe plasmonic resonances, it is possible to consider the material as a homogeneous continuum, with a relative complex dielectric constant which depends on frequency. Depending on NP dimensions, two regimes of interaction of the particle with electromagnetic waves can be distinguished. The quasi-static regime can be considered when the exciting wavelength λ is much higher than particle diameter d ($\lambda \gg d$): in this case the NP responds to a homogeneous polarization during the excitation and the response is affected only by time dependence of the field and not by the spatial dependence. In this regime, the excited plasmonic mode has dipole character. If instead $\lambda \leq d$, a modulation of electromagnetic field inside the particle occurs, which is reflected in a multipolar polarization and in retarding effects in the electromagnetic field.

The optical response of small metallic clusters in the quasi-static regime has been well described by Mie theory [22]. Mie scattering represents a complete and exact mathematical solution of the problem of the scattering of an electromagnetic wave on a sphere, with appropriate boundary conditions and taking into account particle size and dielectric function of NP and surrounding material. Conduction electrons are confined in the small particle volume and thus are forced to move in phase when a forcing radiation is present; polarization charge is thus accumulated on the surface of the NP and acts as restoring force, allowing the resonance to a specific frequency. In the simple case of spherical particle with radius R , polarizability α is expressed by the formula:

$$\alpha = 4\pi\epsilon_0 R^3 \frac{\epsilon(\omega) - \epsilon_m}{\epsilon + 2\epsilon_m} \quad (1.1)$$

where ϵ is the NP dielectric constant and ϵ_m is the dielectric constant of the surrounding material. The isotropic optical response is characterized by an absorbance peak at $\epsilon = -2\epsilon_m$, corresponding to the resonance plasmonic condition.

The optical extinction cross section θ_{ext} for metal particles in the quasi-static regime is related to the polarizability by the relation:

$$\theta_{ext} = kIm[\alpha] + \frac{k^4}{6\pi}|\alpha|^2 \quad (1.2)$$

where k is the wave vector ($k = 2\pi/\lambda$), $Im[\alpha]$ and $|\alpha|^2$ denote the imaginary part and the square modulus of α , respectively.

The first term of eq.1.2 is related to light absorption and describes electron energy losses, such as in Electron Energy Loss Spectroscopy (EELS) measurements; the second term describes losses due to scattering.

This model is a simplified one which is valid for a spherical NP completely surrounded by a dielectric, and so characterized by an isotropic polarization. If the system is anisotropic, a breaking in degeneracy occurs. This happens for example when the nanoparticle is located on a substrate, and the anisotropy of the polarizability is induced by the Van der Waals coupling between the polarized sphere and the induced image charge in the substrate. The coupling along the axis perpendicular to the substrate (z-axis) is different from the in-plane one (x,y): the former is constructive, while the latter is destructive. For this reason, the coupling reduces the polarization parallel to the substrate, while increasing the perpendicular one, so two distinct Mie plasmons modes appear (Fig.1.10). The perpendicular and parallel modes are labeled, respectively, as (1,0) and (1,1) modes according to (L,m) description, where L is the order of multipoles: here $L = 1$ for dipole modes. There are $L+1$ eigenmodes distinguished by the value of m . An approximate idea on the inverse relationship between the plasmon resonance frequency ω_p and the particle polarizability can be obtained from the simplified equation:

$$\omega_p^2 = \frac{Ne^2}{m_e \alpha} \quad (1.3)$$

where N denotes the total number of conduction electrons and m_e and e are the electron mass and charge, respectively. Thus, according to this description, the perpendicular (1,0) and parallel (1,1) modes in a supported particle are respectively red and blue shifted with respect to the fundamental Mie plasmon energy of an isolated sphere, as shown in Fig.1.10(b).

Another anisotropy factor is particle shape. If the NP is not a perfect sphere, like in most real cases, polarizability depends on particle axis ratio. For the simple case of an ellipsoidal particle, polarizability can be expressed as:

$$\alpha = \frac{4}{3} a_i \epsilon_0 \frac{\epsilon(\omega) - \epsilon_m}{\epsilon_m + [\epsilon(\omega) - \epsilon_m] L_i} \quad (1.4)$$

where a_i is particle axis and L_i is depolarization factor depending on particle shape, where $\sum L_i = 1$. The depolarization factors for the perfect sphere are identical and equal to $1/3$. Anisotropy in particle shape is described by the aspect ratio, which is generally defined as the ratio between the particle axis. Particle axis can be different either if NP wets substrate or if shape is not a sphere but a spheroid or an ellipsoid. To simplify, if a spheroidal NP is considered, which means a NP with equal in-plane axis ($a = b$), aspect ratio is defined as the ratio between one of the in-plane axis and the third out-of-plane axis c : a/c . If $a < c$ particle is called a prolate spheroid, viceversa if $a > c$ it is an oblate.

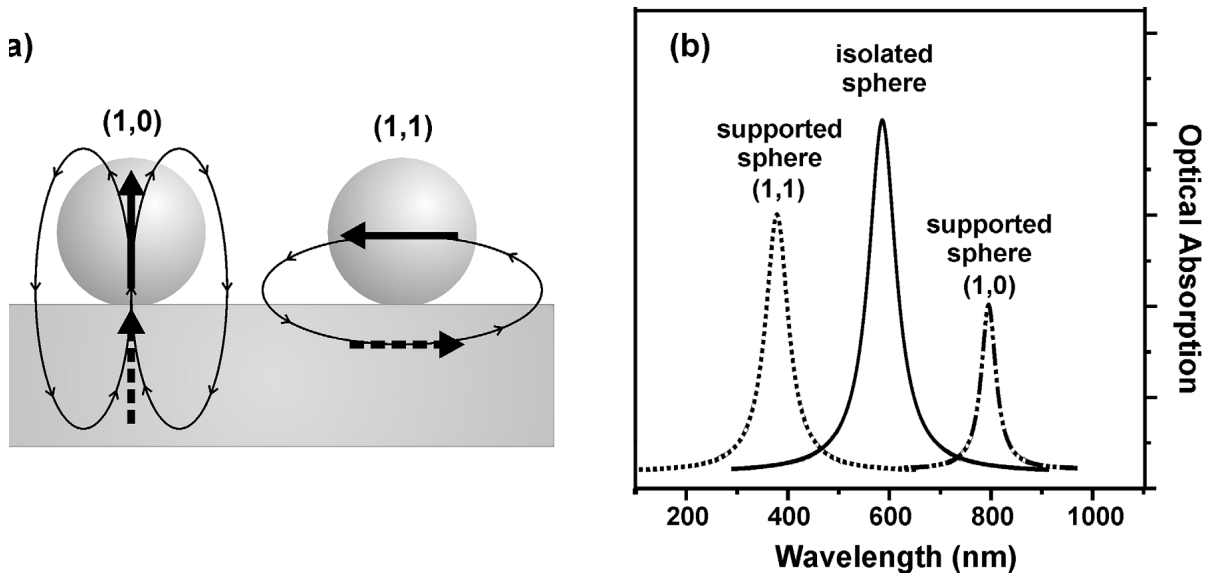


Figure 1.10: (a) Representation of the interaction between $(1,0)$ and $(1,1)$ dipole modes and their induced image dipoles in the substrate (dotted arrow). The interaction strengthens the $(1,0)$ mode (increase in polarizability, corresponding to redshift) and weakens the $(1,1)$ mode (reduction of polarizability, corresponding to blueshift). Field lines for both dipole modes are drawn with weaker lines. (b) Optical absorption cross section for an isolated and a supported spherical NP showing the split into $(1,0)$ and $(1,1)$ modes, due to the presence of substrate.

For a spheroidal particle on a substrate usually the dimension perpendicular to the substrate is called height (h), while the identical in-plane axis are labeled diameter (d), and aspect ratio is defined as d/h . Same definition also accounts for a spherical particle which wets substrate and whose height is lower than diameter.

If particle shape is not spherical and anisotropy increases, the single peak, which is the result of superposition of parallel and perpendicular modes, splits into two distinct peaks. In this case the two peaks shift, increasing the difference in their energy positions [20, 23, 24]. For instance, for an oblate particle, an increase in aspect ratio, which in this case means an increase in anisotropy, leads to decrease of L_c and an increase of L_a and L_b , thus the parallel $(1,1)$ and the perpendicular $(1,0)$ modes are red- and blue-shifted, respectively (see Fig.1.11). Vice versa, for a prolate particle a decrease in aspect ratio induces an increase in anisotropy, with consequent decrease of L_a and L_b , increase of L_c and opposite shift with respect to the oblate shape. Note that these shifts are respectively in opposite (for oblate particle) and same (for prolate particle) direction with respect to the ones induced by the presence of a substrate.

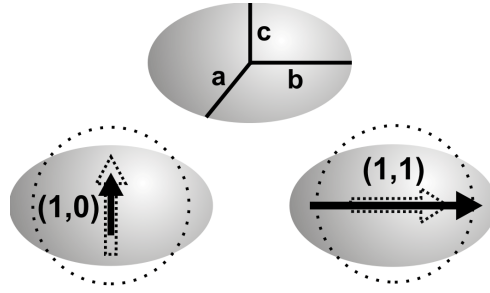


Figure 1.11: *Strength of the $(1,0)$ and $(1,1)$ dipoles in an oblate particle compared to those of a spherical particle with identical volume (dotted lines). The increase of the aspect ratio a/c induces a variation of the particle polarizability, increasing along the particle principle axis a and b , and decreasing along the c axis. This results in the blue- and the red-shift of the perpendicular $(1,0)$ and the parallel $(1,1)$ modes, respectively.*

Particles distribution influences LSPRs too. The dipole-dipole interparticle interaction, which strongly depends on interparticle distance, induces an increase of polarizability along the particle-connection line and a decrease on the perpendicular direction, which determines a shift of plasmonic modes, in this case blueshift for perpendicular mode and redshift for parallel one (Fig.1.12) [20, 21].

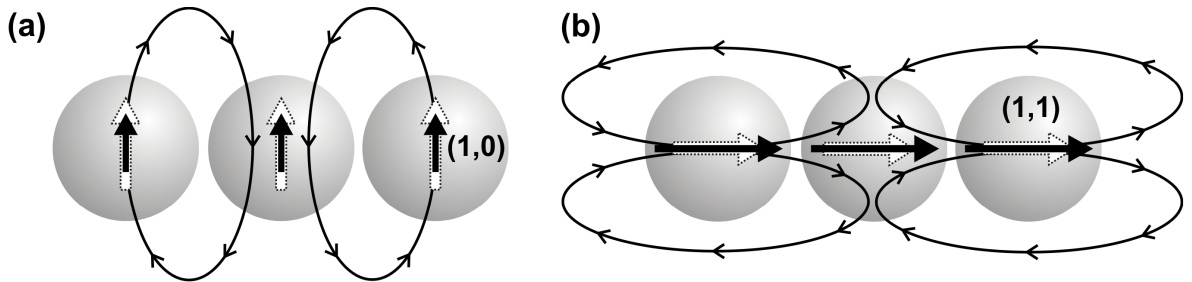


Figure 1.12: *Illustration of the two different dipolar couplings in a chain of NPs. While the $(1,0)$ experience destructive coupling (a), the interaction along the chain is constructive (b). White dotted arrows represent the dipole strength for the isolated particle. The resulting total polarizabilities lead to a shift of the $(1,0)$ mode to higher energy (blueshift) and of the $(1,1)$ mode to lower energy (redshift).*

Plasmonic resonances are affected by particle size: a blueshift is observed with decreasing particle dimensions for both parallel and perpendicular modes. For Ag, which is one of the mainly studied plasmonic materials, the blueshift is due to the fact that $5s$ and $4d$ electrons electrostatic interaction extends only up to a certain distance from the surface, and, in particular, it is absent in the region where $5s$ electrons spill out into the vacuum. So electrons oscillate with unscreened plasma frequency and the surface-plasmon frequency increases. This effect becomes more relevant with decreasing particle diameter because of the greater relative surface-to-volume ratio [25].

It is trivial to state that plasmonic properties depend on nanoparticles material; it is however important to underline the significant role played by the substrate material, which acts both directly and indirectly: on one hand, dielectric constant of the substrate influences polarizability of the system as shown in Fig.1.10, on the other hand a different substrate can induce the growth of particles with different size, shape and distribution, which, in turn, has an effect on LSPRs. For instance, adhesion has been reported to increase for material with a narrow band gap, thus NP with higher aspect ratio are expected to form on a less insulating material [26]. On the other hand, when an oxide with higher dielectric function is involved the absorbance peak at $\epsilon = -2\epsilon_m$ moves to lower energy, inducing a redshift of both plasmonic modes.

In real systems all the previously mentioned factors play a role in determining the plasmonic response. By varying materials involved, particle size, shape and distribution it is possible to tune plasmonic properties and obtain different LSPRs.

Plasmonics applications

The most relevant effect of the formation of a LSPR is the induced strong field enhancement in the proximity of the NP (see Fig.1.13), which increases light absorption in the surrounding semiconductor material and opens the way to a wide range of applications such as solar cells, photocatalysis, optical antennas, plasmonic switches, optical biosensors, lasers and LED [27]. The strong improvement in light absorption and photocarrier generation due to the presence of metal NPs in both Dye-Sensitized solar cells [28–30] and in Si-based solar cells [31,32] has been reported from various studies. The exploitation of plasmonic properties to improve performance of photovoltaic devices allows to reduce the amount of active material needed, thus substantially diminishing the costs and opening the way to a wide diffusion of this technology.

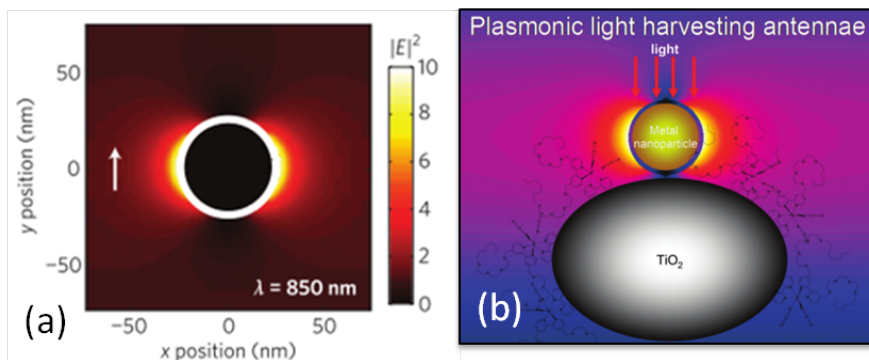


Figure 1.13: (a) Intensity enhancement around a 25-nm-diameter Au particle embedded in a medium with $n=1.5$ under 850 nm incident light. The magnitude of the enhanced electric-field intensity is indicated by the colour scale [28]. (b) Schematic representation of a NP/oxide system, which can act as a plasmonic antenna [29].

Among metals, the most studied for plasmonic purpose are Ag and Au. They are relatively air-stable and their LSPR absorption bands can be tuned in the visible and near-ultraviolet spectral regions, which are the suitable range for applications [33]. In particular, Ag represents an interesting case study, since the presence of d-bands significantly reduces plasma frequency from the expected 9.05 eV to 3.78 eV: at this frequency the imaginary part of the dielectric function ϵ_2 is low, and thus losses are reduced [34].

Thanks to the wide range of peculiar properties, possible applications and variety of nanostructures formed, zinc oxide represents a very interesting material not only in the field of applied nanotechnologies, but also for the study of fundamental processes involved. For this reason three zinc oxide-based metal-oxide systems have been prepared and analyzed, where different metals play different roles. The growth and analysis of ZnO thin films deposited on a Mo substrate are described in Chap.2; the effect of Al doping on zinc oxide films is depicted in Chap.3; the plasmonic properties of Ag nanoparticles deposited on a ZnO bulk crystal are presented in Chap.4.

Chapter 2

ZnO thin films on Mo(001)

The first part of the study is focused on a model system composed by ZnO thin films deposited on a Mo substrate, in order to unravel the growth mechanism from the first stages and to relate various properties to deposition parameters.

The results have been obtained by combining different techniques to shed light on ZnO film growth by Molecular Beam Epitaxy. Scanning tunneling microscopy, x-ray photoelectron spectroscopy and x-ray diffraction have been employed to investigate the role of deposition parameters, like O pressure, Zn rate and temperature treatments, and to determine a model for the growth evolution of the ZnO film, the role of the interface with the substrate and the evolution of the defects in the film. By means of LEED and XRD the structure of the film has been investigated. These results improve the understanding of ZnO thin films growth and properties, that can be relevant as model systems for the comprehension of widely studied ZnO nanostructures in various fields.

State of the Art about ZnO thin films grown on bulk crystals is presented in the first section, followed by a brief description of the UHV apparatus at University of Modena and Reggio Emilia, where most of the systems treated in this work have been prepared and analyzed. Then, the study of the growth of ZnO/Mo(001) is presented.

2.1 ZnO thin films

The study of the material as a thin film is a powerful method to analyze a model system and at the same time getting closer to the real system.

Zinc oxide thin films have been prepared considering a wide range of substrates and techniques, chosen to match the desired characteristic of the material or the possible applications. While magnetron sputtering is a suitable scalable deposition technique to prepare a material which can be used to assemble a prototype solar cell, molecular beam epitaxy (MBE) is a more suitable method to obtain a model system and get a deeper

insight into the fundamental properties of the material, since it permit to obtain highly controlled films with excellent crystal quality.

In the majority of studies ZnO have been grown by MBE on fcc(111) or hcp(0001) oriented substrates, and the expected growth along c-axis was observed [5, 35–38].

The most used substrate to grow ZnO films is $\text{Al}_2\text{O}_3(0001)$ (sapphire), on which epitaxial growth occurs, despite the high lattice mismatch of 18% [9]. However, the quality of the film obtained is low and the formation of rotational domains has been observed [5]. To reduce the mismatch and eliminate domains, a buffer layer can be used, like $\text{MgO}(111)$: the presence of MgO seems to reduce surface energy and defects density and to increase the number of nucleation centers for ZnO; additionally, diffusion of the zinc in MgO promotes the formation of a ternary compound, $\text{Zn}_x\text{Mg}_{1-x}\text{O}$, which gradually reduces the mismatch between ZnO and MgO and favours epitaxial growth of the film [39, 40]. The formation of the ternary compound is however undesirable to the purpose of understanding the growth of material and its properties. Additionally, facets are formed on the surface (Fig.2.1).

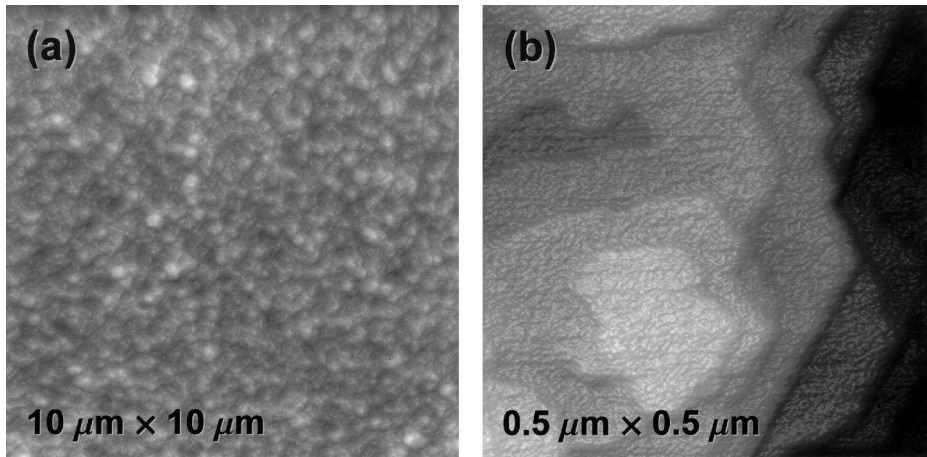


Figure 2.1: (a) $(10 \times 10) \mu\text{m}^2$ AFM image shows the surface of a $1.0 \mu\text{m}$ thick ZnO epilayer grown on $\text{Al}_2\text{O}_3(0001)$ with $\text{MgO}(111)$ buffer layer. The RMS value of the surface roughness is about 0.8 nm . (b) $(5 \times 5) \mu\text{m}^2$ AFM image of the same sample shows the 2D islands. Steps with height of either 2.6 \AA or 5.2 \AA are observed [39].

The possibility to perform electronic spectroscopies and the interest in applications which involve the association of the zinc oxide with a metal material make metals particularly suitable as a substrate for the growth of ZnO films. ZnO has been deposited on Pd(111) to improve the catalytic properties of the metal through the formation of PdZn alloys, which is an active catalyzer in methanol synthesis [36, 37]. Weirum et al. reported that ZnO film morphology, structure and stoichiometry strongly depend on the preparation conditions, oxygen pressure and zinc coverage in particular [36].

Ag(111) [35] and Au(111) [38, 41] have also been chosen as a substrate to grow a well oriented ZnO(0001) film and study fundamental phenomena such as depolarization of the polar surfaces and the role of intrinsic defects (Fig.2.3).

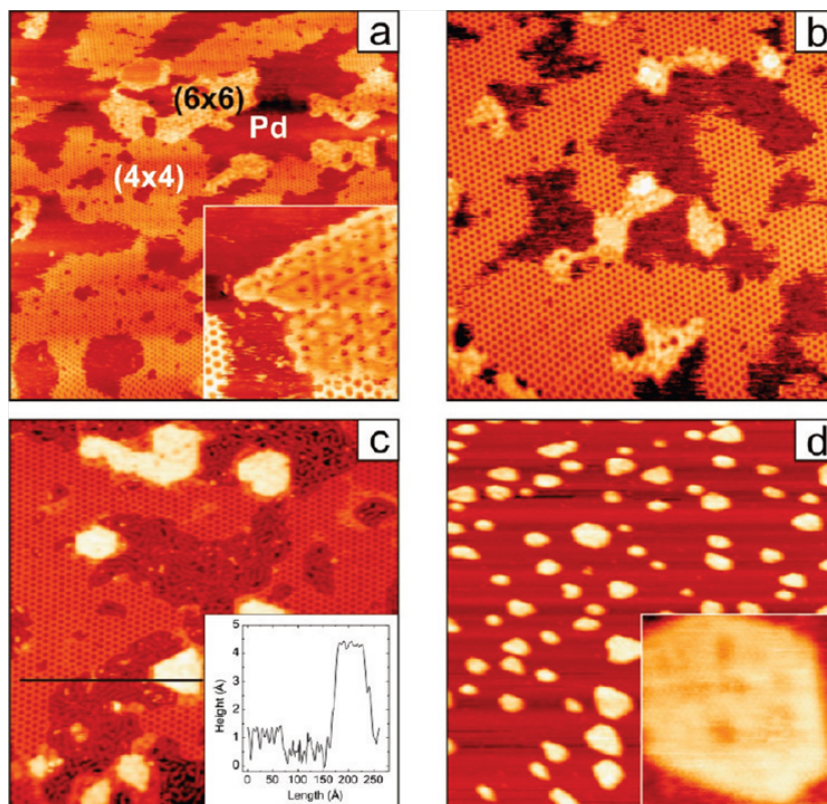


Figure 2.2: STM images of sub-monolayer (0.6-0.7 ML) ZnO prepared on Pd(111) at different oxygen pressures: (a) 5×10^{-8} mbar O_2 (100×100) nm^2 (1 V, 0.4 nA), inset: (20×20) nm^2 (30 mV, 1.5 nA); (b) 1×10^{-7} mbar O_2 (50×50) nm^2 (1 V, 1 nA); (c) 1×10^{-7} mbar O_2 (50×50) nm^2 (1 V, 1 nA), inset: line profile taken along the line (black), indicated on the image; (d) 5×10^{-6} mbar O_2 (150×150) nm^2 (1 V, 0.4 nA), inset: bilayer island surface (20×20) nm^2 (0.5 V, 1 nA) [36].

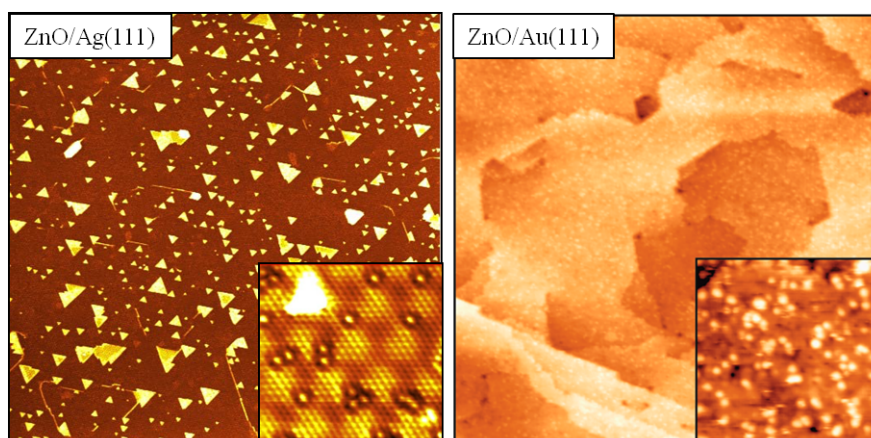


Figure 2.3: (200×200) nm^2 STM images. (a) 2.2 ML ZnO on Ag(111) (1.6 V, 0.5 nA); inset: high resolution (9×9) nm^2 image (1.2 V, 0.2 nA) [35]. (b) 25 ML ZnO grown on Au(111) (3.8 V, 1 nA); inset shows nanosized protrusions that are assigned to hydroxyl groups on O-terminated ZnO [41].

Cubic (001) and (110) surfaces have been used in few cases, to favour the growth on non-polar surfaces, both on insulators (MgO [42–44]) and metals (Rh [45], Cu [46] and Mo [47, 48]). The majority of these studies report the coexistence of different orientations, a c-axis growth or the formation of polycrystalline film, while the growth on a-plane and m-plane have been successfully obtained on (1 $\bar{1}$ 02) r-plane sapphire [49, 50] and MgO(001) [42], which are both insulators.

Together with the interest for the stabilization of different surfaces in thin films, some points concerning ZnO growth remain unclear and in particular the initial growth mechanisms and the control of defects concentration. Initial growth mechanisms can deeply influence composition, chemical properties of films and structural evolution, through interfacial interactions [51]. Furthermore, defects control is fundamental for catalytic activity of material and deeply influences the luminescence response of the system [41, 52].

ZnO/Mo(001)

For the growth of ZnO films on the non-polar surface, a good candidate is represented by Mo(001). Molybdenum body centered cubic (bcc) structure with lattice parameter of 3.15 Å shows a small lattice mismatch (3%) with the rectangular (10 $\bar{1}$ 0) surface and a 5/3 matching with the quasi-square (11 $\bar{2}$ 0) plane, whose parameters are $a = 5.63$ Å and $b = 5.21$ Å, thus it can favour the growth on a- or m-plane [47].

Differently from what observed for other cubic substrate like MgO, Mo does not form alloys with Zn for temperature lower than 1600 K, and thus no ternary compounds are expected to form at the interface between film and substrate [53]. The high thermal stability of molybdenum allows high temperature treatments, which can improve crystal quality of the film. Additionally, a metal substrate permits the use of electronic spectroscopies and analysis techniques, which can not be performed on insulators like MgO or sapphire.

In the work by Zheng et al. a polycrystalline ZnO film has been obtained by post-oxidation through annealing in O₂ atmosphere (pressure: 3×10^{-7} - 3×10^{-6} mbar) of a 30 Å metallic zinc previously deposited on a Mo(100) bulk crystal [47]. Results show that the atomic ratio between oxygen and zinc in the film strongly depends on annealing temperature and O₂ pressure. A stoichiometric film has been obtained with 3×10^{-6} mbar O₂ pressure and 400 K. Zn results hard to be oxidized by partial O₂ in UHV at temperatures lower than 400 K, while, above 400 K O desorption from the oxide occurs.

To my knowledge any studies on ZnO film grown on Mo(001) by deposition of Zn in O₂ atmosphere have not been performed and a good understanding of the first stages of zinc oxide film in general is still missing.

In the next sections a deep investigation of the growth mechanism of ZnO films on Mo(001) substrate is reported, analysing the dependence of composition, morphology and crystal structure on deposition parameter and Zn thickness.

2.2 Experiments @SESAMo Laboratory

UHV system

The majority of the experiments in this work, including the preparation and analysis of ZnO/Mo system, have been performed at University of Modena and Reggio Emilia, using the UHV apparatus at SESAMo Laboratory.

The UHV system, available for cleaning procedures, growth and analysis of the samples *in situ* is shown in Fig.2.4. It is composed of three chambers, connected in UHV conditions with transfer drivers that permit to carry the samples from one chamber to the other. The main chamber is equipped for chemical and structural analysis and for the preparation of the clean substrates. A typical background pressure for this chamber is 1×10^{-10} mbar. A high precision manipulator with five degrees of freedom, three for translation (x , y , z) and two for rotation (θ , around the manipulator axis, and ϕ , around the normal to the sample) provides the movements through the chamber. All the manipulator movements are driven by stepping motors controlled by a computer. The manipulator is equipped with a filament to heat the sample up to 1200 K. Facilities to prepare the surface are also available, like an ion gun for sample cleaning and a gas line to introduce O_2 in the chamber.

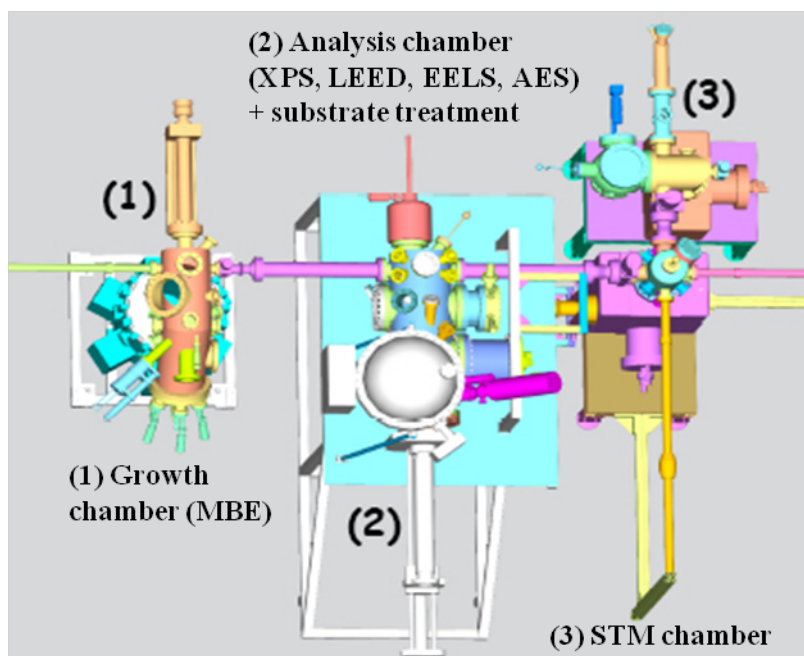


Figure 2.4: Top view of the UHV system at SESAMo Laboratory. (1) Deposition chamber equipped with Knudsen cells for MBE. (2) Analysis chamber, where XPS, EELS, LEED and AES techniques are performed; in this chamber substrate are prepared and thermal treatments take place. (3) STM chamber.

The chamber is equipped for analysis with:

- a cylindrical mirror analyser (PHI 590A) operating in the first derivative mode, with a coaxial electron gun (LaB₆ filament). This analyser is used for Auger Electron Spectroscopy. The centre of the sample is automatically kept in the focus of the electron beam, during sample rotation, via software
- a conventional non-monochromatic Mg-Al twin anode X-ray source, used for X-ray Photoemission Spectroscopy (XPS)
- a Concentric Hemispherical Analyser Omicron EA125 for XPS and EELS, which has a set of seven channel electron multipliers
- a three-grid Omicron LEED apparatus with a LaB₆ filament. Diffraction patterns are recorded on a computer controlled 16 bit CCD camera (Apogee ALTA U2000). The sample surface can be positioned at the LEED working distance with an accuracy of ± 0.01 mm
- an electron gun used for EELS technique

The main part of the materials grown for this work, both metals and oxides (apart from AZO films and the Ag/ZrO₂ system), have been prepared in the growth chamber. This is kept in UHV at a typical pressure of 1×10^{-10} mbar by means of an ion pump. A manipulator with five degrees of freedom moves the sample from the transfer position to the evaporation position in front of the cells and is equipped with a filament to heat the sample up to 1200 K. The chamber contains six Knudsen cells for the evaporation of metals. They are equipped with a shutter, that can be mechanically opened to start and stop abruptly the metal deposition. A quartz microbalance is used to calibrate the metal flux. The oxide deposition rate is estimated by the measured metal flux and taking into account the density of metal atoms in the oxide. A further check of the deposition rate can be made by quantitative XPS analysis. A gas inlet terminated by a nozzle provides the O₂ for oxide deposition. A thermal cracking system is also available to obtain atomic oxygen from O₂, with an estimated 70% efficiency.

A separate chamber has been built for the Omicron RT STM-AFM apparatus. The chamber has a typical pressure of 5×10^{-10} mbar. The STM-AFM is equipped with a stage for the storage of samples and tips. The STM is insulated by external vibrations by suspension with springs and Eddie currents. For the STM images acquired with this apparatus etched W tips have been used.

This apparatus has been used to prepare ZnO/Mo, Ag/ZnO and Ag/MgO/Mo systems and to perform XPS, EELS, LEED and STM techniques.

ZnO/Mo(001) experimentals

For ZnO growth a Mo(001) single crystal has been chosen as a substrate, prepared under UHV conditions by cycles of Ar⁺ ion bombardment at room temperature (RT), followed by sputtering at 1150 K. The obtained surface is almost free of O and C and a (1×1) LEED pattern is visible. ZnO films have been grown by evaporating Zn with an effusion cell on the clean Mo surface kept at different temperatures in a O₂ partial pressure varying from 1×10⁻⁷ mbar to 5×10⁻⁶ mbar, introducing the gas by means of a nozzle placed 1 cm far from the sample surface. The O₂-to-Zn flux ratio will be referred to as N and has been varied between 44 and 8900. The number of O₂ molecules introduced in the growth system per unit time has been estimated by the product of the O₂ partial pressure and the pumping speed of the system (500 l/s). Since a nozzle was used to direct the gas flow to the sample surface, we assume that all the introduced molecules impinge on the surface. The Zn atomic flux has been measured with a quartz crystal microbalance placed in the same position of the sample during growth and has been changed between 7×10⁻³ and 3×10⁻² Å/s.

XPS and Auger spectra were recorded using a non-monochromatized Al-K α X-ray source and an hemispherical electrostatic analyzer, with an angular acceptance of +/-8° to smear out possible diffraction effects. The overall energy resolution, dominated by the width of the Al-K α line, is about 1 eV. Electron collection has been performed in normal emission (NE), i.e. with a 0° angle with respect to the normal to the sample surface, or grazing emission (GE), i.e. with an angle of 65°. XPS intensities have been determined by measuring the areas of the peaks after Shirley background subtraction. Standard XPS reference spectra have been measured on a ZnO crystal cleaned by sputtering and annealing for Zn²⁺ reference and on a thick Zn film grown on Mo(001) for Zn⁰ reference. The morphology of ZnO films has been investigated by an in situ UHV RT Omicron STM, working in constant current mode, with the W tip kept grounded and a positive bias voltage applied to the sample. STM images have been analyzed by means of WSxM program [54]. X-Ray Diffraction plots have been measured by means of a Cu-K α X-ray source and a diffractometer X'Pert PRO with θ -2 θ geometry, flat monochromator and parallel plate.

2.3 Film composition and growth

Increasing amounts of metal Zn have been deposited on Mo(001) at RT in a O_2 partial pressure of 1×10^{-6} mbar, with a Zn rate of 3×10^{-2} Å/s, with $N=440$.

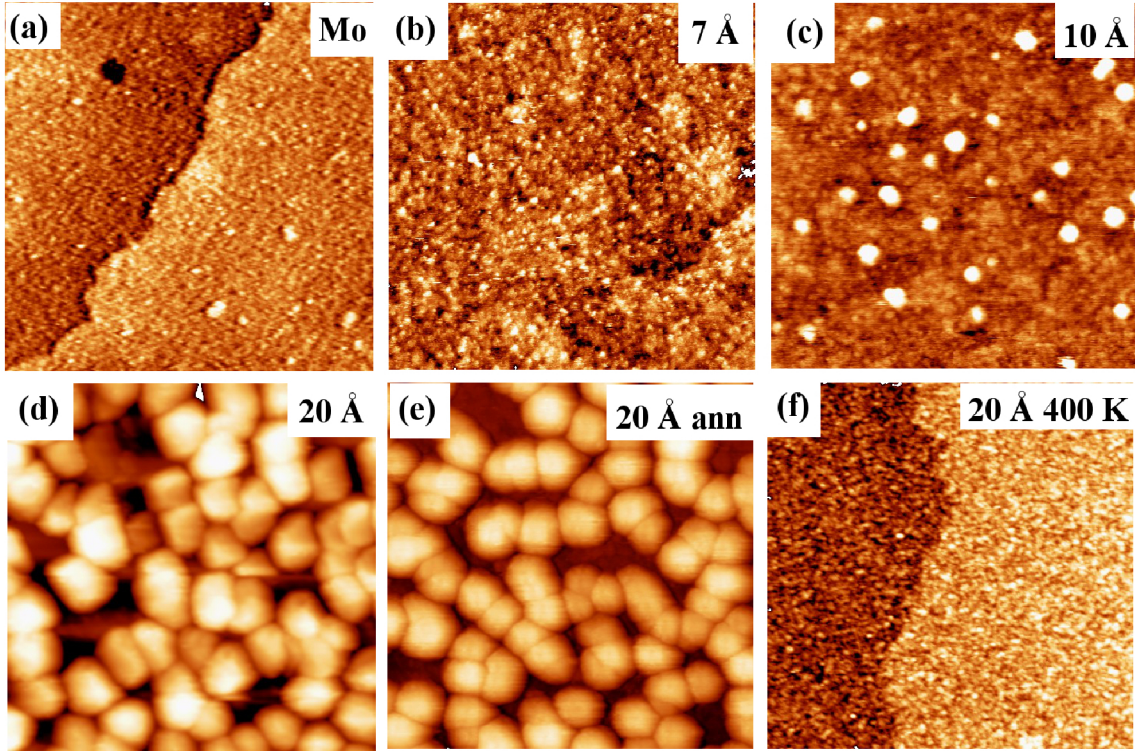


Figure 2.5: $(100 \times 100) \text{ nm}^2$ STM images of (a) clean Mo(001), (b) 7 Å (1 V, 0.4 nA), (c) 10 Å (1.5 V, 0.1 nA), (d) 20 Å ZnO (2 V, 0.12 nA) deposited at RT on Mo(001) at $p(O_2) = 1 \times 10^{-6}$ mbar and $N=440$. (e) Same sample as (d) after annealing at 500 K in O_2 ($V=2$ V, 0.05 nA); (f) 20 Å nominal ZnO deposited at 400 K (2 V, 0.05 nA).

STM images of Mo surface show monoatomic terraces and some impurities [Fig.2.5(a)]. Below 10 Å of ZnO equivalent thickness a continuous granular film is obtained that entirely covers Mo surface, with a rms roughness of about 1 Å [Fig.2.5(b)]. Above the thickness threshold of 10 Å, islands appear on top of the continuous film with a diameter of 3-5 nm [Fig.2.5(c)]. Increasing thickness, an increasing number of larger islands are visible on the surface, with a diameter of 10-15 nm, reaching a complete coverage above 30 Å [Fig.2.5(d)]. A mild annealing at 500 K in O_2 partial pressure (1×10^{-6} mbar) does not modify islands shape, dimension and coverage [Fig.2.5(e)].

On the contrary deposition with a substrate temperature of 400 K modifies the ZnO growth [Fig.2.5(f)]. Deposition of 20 Å nominal thickness of ZnO [same thickness as Fig.2.5(d)] results in a closed film of 5 Å effective thickness (as evidenced by XPS quantitative evaluation), with no islands detected. The low effective thickness, as compared

to the nominal one, indicates that at temperature higher than RT Zn is not efficiently sticking to the Mo surface, due to the low vapor tension at the investigated temperatures. Increasing the deposition temperature further reduces the total amount of deposited ZnO, without improving quality.

The films have been studied by means of XPS to determine the composition in the different steps of growth. Fig.2.6 reports the Zn L₃M₄₅M₄₅ Auger line measured with Al-K α photons. This peak enables the observation of different Zn oxidation states, due to the marked difference between positions and lineshapes for e.g. Zn⁰ and Zn²⁺ in ZnO. Clearly up to 10 Å the energy position and lineshape of the Auger main peak is very similar to the bulk ZnO reference spectrum, characterized by a main feature at 989 eV kinetic energy and a less pronounced shoulder at about 992 eV. This allows to assign the compact film observed in STM images to ZnO [Fig.2.5(b,c)]. For thin films a broadening of the Auger peaks partially hides the high kinetic energy shoulder, due to the higher defectivity and the presence of different Zn sites as compared to bulk oxide. Above 10 Å a component of increasing intensity is detectable at 992 eV on the high kinetic energy side of the main peak, with a smaller component at 995.5 eV.

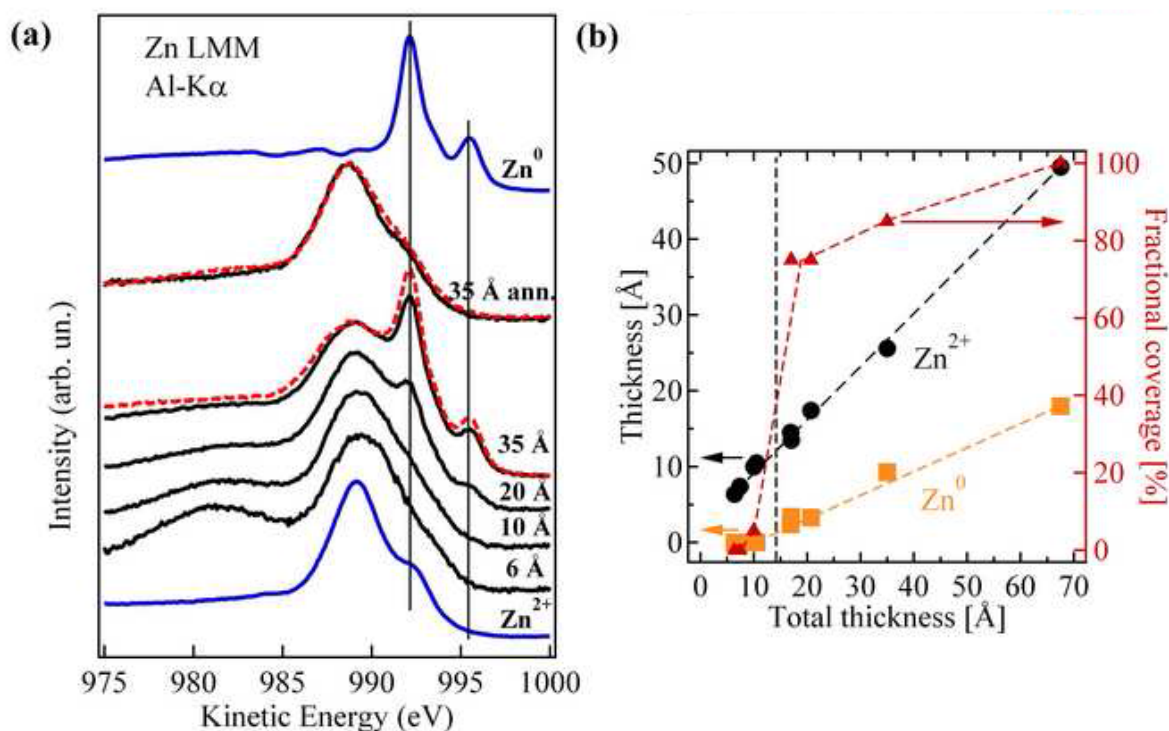


Figure 2.6: (a) XPS ZnLMM peaks measured with Al-K α photon for increasing total thickness. Black curves are measured at normal emission (NE), red dashed curves at grazing emission (GE), blue curves are bulk reference spectra. (b) Zn⁰, Zn²⁺ thickness (estimated by exponential attenuation model) and coverage (obtained by STM images) as a function of total thickness.

The components at 992 eV and 995.5 eV KE correspond to the position of the $L_3M_{45}M_{45}$ Auger transition of Zn^0 . This additional metallic component is increasing in intensity when spectra are measured in grazing emission configuration and can be therefore assigned to a surface phase. Annealing at 500 K in oxygen partial pressure of 1×10^{-6} mbar for 10 minutes completely oxidizes the ZnO film, in spite of the absence of variation in surface morphology. The absence of residual metallic phase is evident from the grazing emission spectrum, that is exactly superimposed to the normal emission one. This indicates that temperature stimulates the oxidation but it is not sufficient to rearrange the surface or to induce long range ordering (no spots are detected in LEED patterns, not shown here). The same effect is evident for films deposited at temperatures between RT and 500 K, that result completely oxidized after deposition. However, both deposition and annealing at temperatures higher than 500 K leads to a reduced sticking or to a desorption of the film from Mo surface.

2.3.1 Modeling of film growth

Experimental evidences from XPS allow to qualitatively assign the morphological features, namely islands, observed in STM images to the appearance of a surface metallic Zn component on ZnO film above 10 Å total thickness. To quantitatively confirm this model and clarify the first stages of growth, ZnLMM lineshapes have been obtained by summing Zn^0 and Zn^{2+} contributions, together with the Mo3s peak visible at 982 eV, that must be taken into account to correctly fit the ZnLMM lineshape. A fitting procedure has provided the quantitative evaluation of the separated contributions. An exponential attenuation model has been used to estimate the $Zn_{LMM}^{2+}/Mo3d$ intensity ratio to quantify ZnO amount, while for the estimation of metal quantity the Zn_{LMM}^0/Zn_{LMM}^{2+} intensity ratio has been evaluated. The model consists of metallic Zn islands covering a fraction of a continuous zinc oxide film. The fractional coverage of the metallic islands is obtained by STM images and assumed as an input data for the model. The output of the model are the thickness of the ZnO continuous film and the equivalent thickness of the Zn islands (intended as the thickness Zn would have if grown in a layer-by-layer mode). The coverage from STM images and the obtained Zn^{2+} and Zn^0 thicknesses are reported in Fig.2.6(b) as a function of total deposited amount, namely the sum of ZnO and Zn equivalent thickness (in the following named simply total thickness). Inelastic Mean Free Paths (IMFPs) have been determined using the Tanuma-Powell-Penn model, corresponding to 20 Å for Zn LMM and 24 Å for Mo3d electrons [55]. The oxide film thickness is linearly increasing with total deposited amount and above a threshold of 10-15 Å an increasing quantity of metallic Zn is present, reaching 18 Å for 70 Å total thickness. The correspondence with the threshold observed in STM is evidenced by the comparison with the increasing fractional coverage of STM images. Oxygen partial pressure employed is insufficient to completely oxidize Zn, therefore during growth some part of the Zn atoms remains in a

metallic state and acts as a surfactant on the oxide surface, due to a lower surface free energy of 0.94 J/m^2 , as compared to values between 1 and 2.2 J/m^2 for the oxide [56, 57].

2.3.2 Modification of oxidizing conditions

The morphology and composition of a 30 \AA film has been investigated as a function of (1) N and (2) different oxidizing agent during deposition.

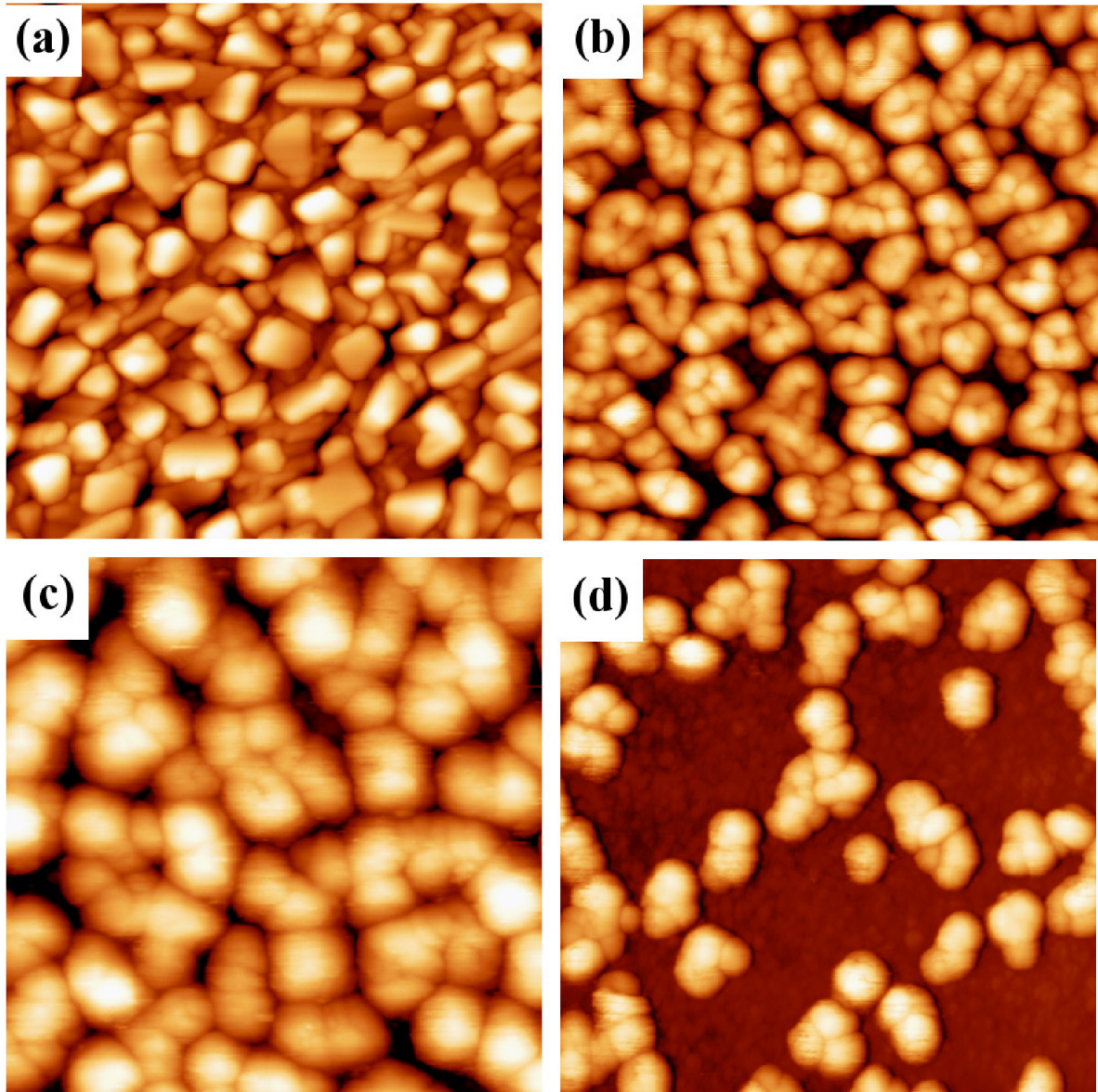


Figure 2.7: $(100 \times 100) \text{ nm}^2$ STM images of 30 \AA ZnO (a) grown at $N = 44$ (0.5 V , 0.1 nA), (b) same as (a) after annealing in O_2 atmosphere (1 V , 0.1 nA), (c) $N=440$ (2 V , 0.07 nA), (d) $N=1780$ (2.2 V , 0.06 nA).

Reducing N to 44 [reducing $p(\text{O}_2)$ to 1×10^{-7} mbar] a complex behavior is observed: i) metal covers entirely the ZnO film [Fig.2.7(a)] and ii) after annealing nanostructures of peculiar shape are formed [Fig.2.7(b)], probably related to a structural reordering due to oxidation during annealing. The use of a stronger oxidizing agent, namely a monoatomic O source based on thermal cracking, does not modify neither the surface morphology nor the chemical composition of the film (not shown here). Increasing N to 440 (increasing pressure to 1×10^{-6} mbar) and 1780 (by a reduction of the Zn deposition rate to 7×10^{-3} Å/s) a reduction in the fractional coverage of the islands from 0.9 to 0.4 is observed in STM images [Fig.2.7(c) and (d) respectively]. ZnLMM Auger peak evidences a decrease of the metallic component, as shown in Fig.2.8(a). Increasing N to 8900 [$p(\text{O}_2) = 5 \times 10^{-6}$ mbar, $R_{\text{Zn}} = 7 \times 10^{-3}$ Å/s] Zn shoulder almost disappears. Fig.2.8(b) reports the trend in metallic Zn thickness as a function of total deposited material. This clearly evidences the progressive oxidation of the film with N and the corresponding required growth conditions.

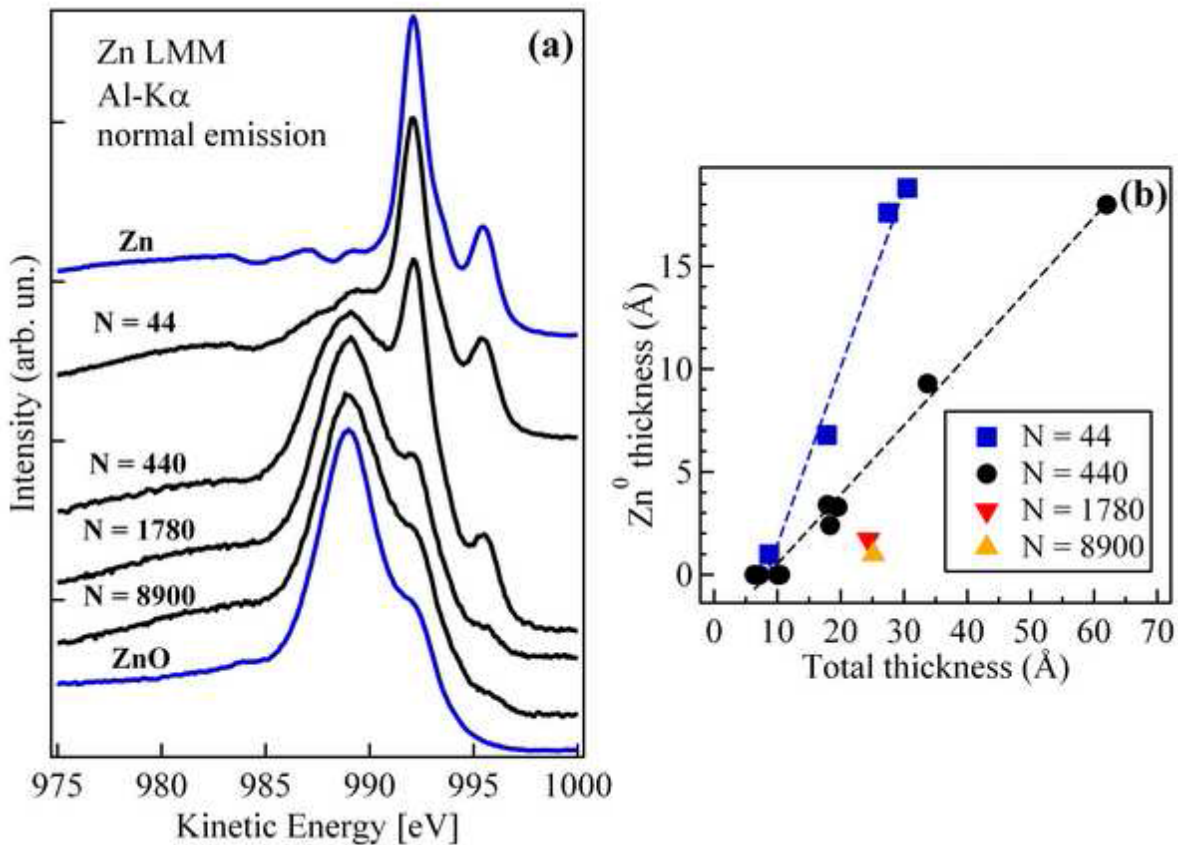


Figure 2.8: (a) XPS ZnLMM peaks measured with Al-K α photon for increasing N during deposition. (b) Quantitative evaluation of metallic Zn after deposition as a function of total thickness for the different O:Zn ratios.

2.4 Film defectivity

Finally, to clarify the mechanism of oxide growth, the lineshape of O1s peak has been evaluated.

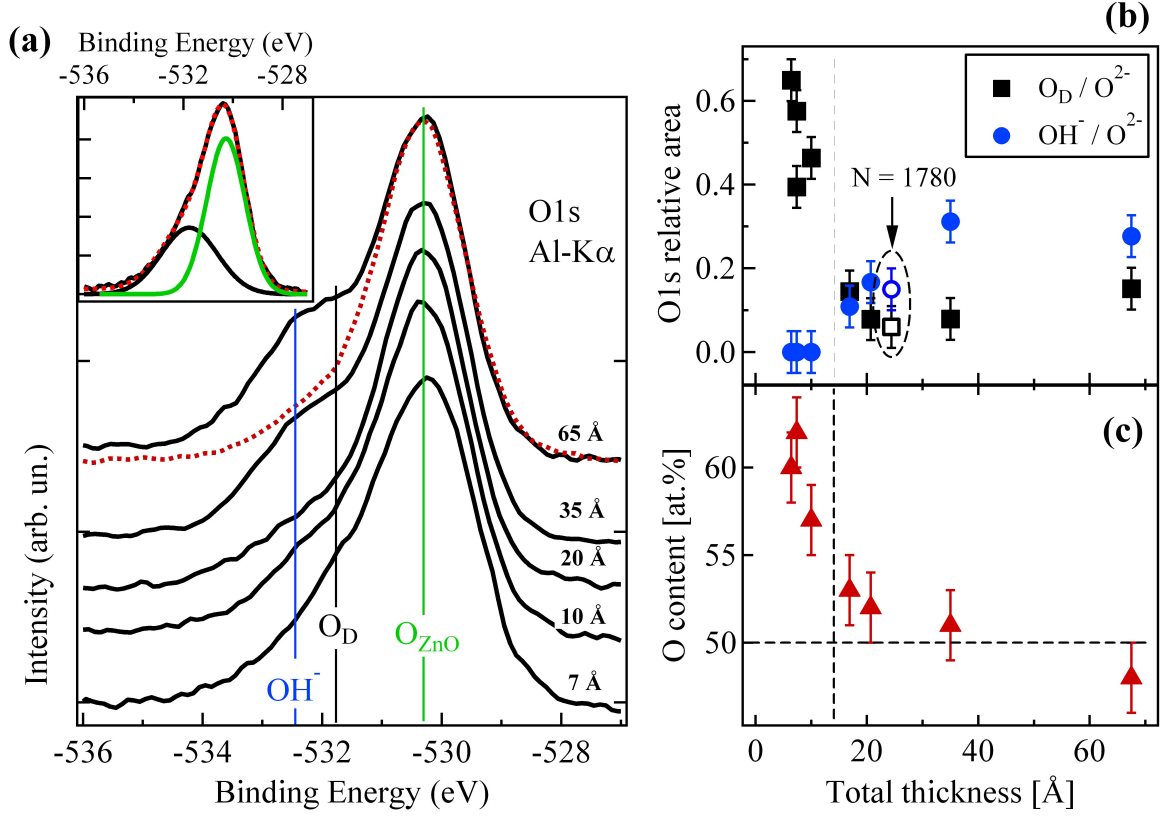


Figure 2.9: (a) XPS O1s peak for ZnO film of increasing thickness, measured at NE. Dotted red curve reports spectrum after annealing in O₂. Inset shows O1s Gaussian deconvolution for 7 Å. (b) O1s components relative area (black square: O_D/O²⁻; blue dot: OH⁻/O₂⁻) for N=440 and 1780 (empty markers) and (c) O content in ZnO film versus total thickness.

As evidenced in Fig.2.9(a), O1s peak is not symmetric and besides the main component at 530.2 eV, assigned to O²⁻ in ZnO regular lattice (O_{ZnO}) or to O in Mo surface oxidation, an additional feature is present at about 1.5 eV higher binding energy. This component is often assigned to O sites with a lower coordination (O_D), sign of the presence of defects in the ZnO lattice, as previously reported in literature [58]. The lineshape of O1s peak changes with increasing thickness, as the shoulder shifts to higher binding energy. The best fit of the spectra is obtained adding a third Gaussian component at 2.3 eV, compatible with OH⁻ groups, that is not present at thickness lower than 10 Å [59]. Fig.2.9(b) reports the relative intensity of the O_D and the OH⁻ component area with respect to the main component O_{ZnO}. O_D/O_{ZnO} ratio decreases and OH⁻/O_{ZnO} ratio increases with increasing total thickness, compatible with the shift of the shoulder.

Annealing at 500 K does not substantially modify the O_D relative area, while it decreases significantly that of OH^- , that desorbs from the surface. Finally, from the intensity ratio of Zn^{2+} component of ZnLMM and O1s, an estimation of the stoichiometry evidences that the oxide is over-stoichiometric in O before threshold and approaches 50 at.% with increasing thickness, following the behavior of O_D/O_{ZnO} ratio [Fig.2.9(c)].

Since the O_D/O_{ZnO} ratio is associated to the relative abundance of defects in the film, the picture of growth evolution of the film can be completed. In the first stages of growth of Zn on Mo surface in presence of oxygen, a ZnO film is formed, stimulated by the Mo surface oxidation or by the availability of O dissociated by Mo, indicating therefore an interface rich in oxygen. In fact when Mo surface is pre-exposed to 1×10^{-6} mbar for few minutes and metallic Zn is subsequently deposited without oxygen atmosphere, a film of ZnO is obtained with about the same quantity of defects and stoichiometry as compared to Zn grown in oxygen, but with a larger amount of metallic Zn on the surface. With increasing total thickness and going far from the interface the effect diminishes and the film starts to become oxidized with a lower amount of defects and with a stoichiometry that approaches 1:1. Defects are related to Zn vacancies, O and Zn interstitials, typical of ZnO films [60,61], or to structural deformations. The process continues until the threshold thickness is reached: when the interface is too far, the O reservoir effect of Mo disappears and Zn is not sufficiently oxidized by the insufficient oxygen partial pressure. Then, part of the Zn atoms remain on the surface in a metallic state, while the stoichiometry of the oxidized part of the film remains substantially unchanged at 1:1.1 for 70 Å total film thickness.

Annealing determines oxidation of the surface metal, but no substantial changes in defects concentration or film stoichiometry, extending the compositional properties of the ZnO continuous film to the surface Zn islands. On the contrary OH^- , that increases in quantity in correspondence to the appearance of islands on the surface, is strongly reduced by post-growth annealing. To improve significantly the quality of the film in terms of composition, higher oxidizing conditions are necessary during growth to lower metallic Zn quantity and increase the corresponding threshold thickness, as reported in Fig.2.8. However, oxide defects are unchanged [Fig.2.9(b)], indicating that they are intrinsic of the film and not related to oxidation conditions during growth.

2.5 Crystalline structure

No LEED pattern is visible for the ZnO films in the investigated conditions and temperature treatments up to 500 K do not improve crystalline quality from this point of view. XRD scans have been performed to deepen the comprehension of crystalline structure of the film. Fig.2.10 reports the scans measured on a 60 Å ZnO film grown at O:Zn = 440 after annealing at 500 K.

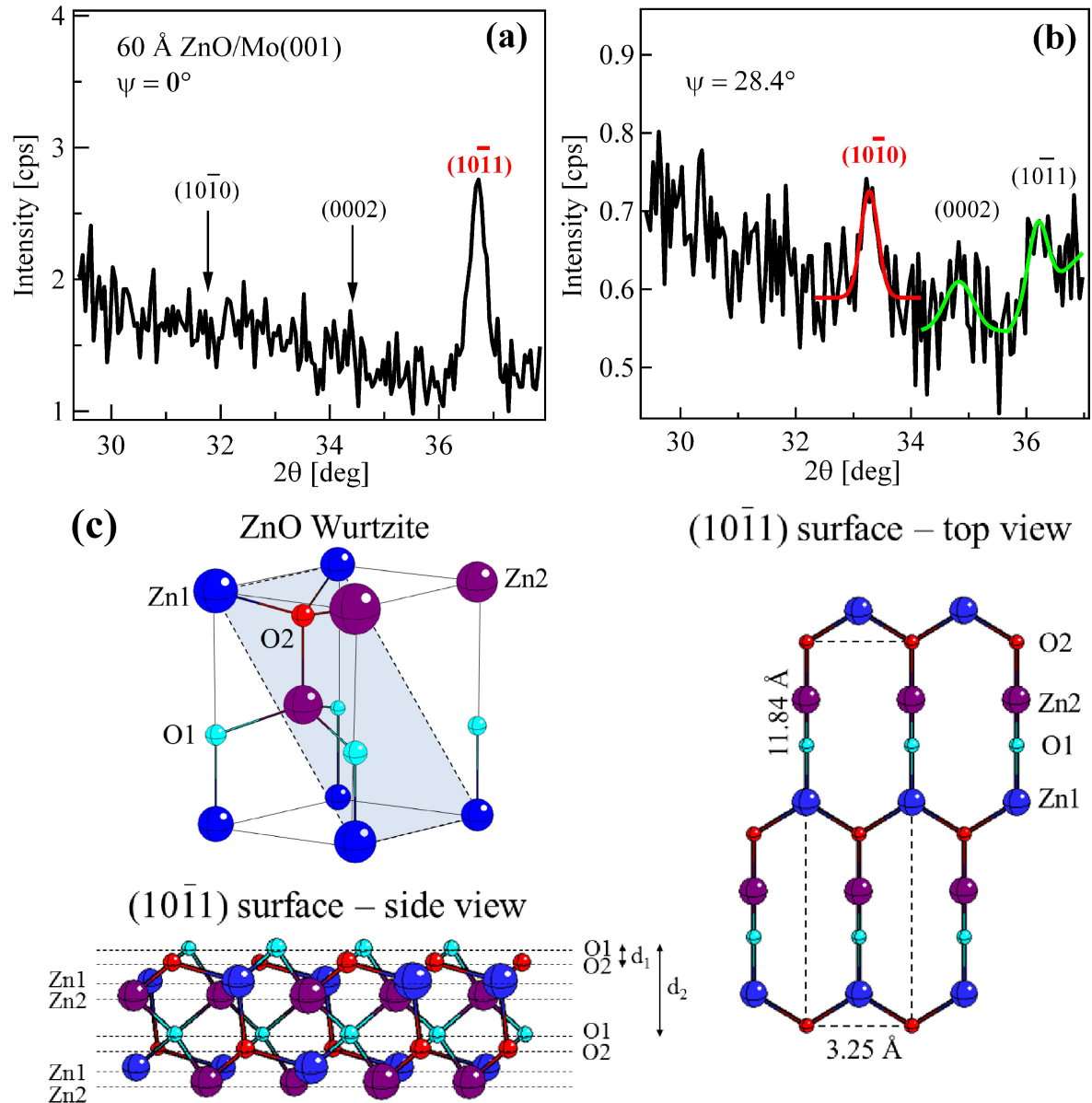


Figure 2.10: XRD scans with (a) $\psi = 0^\circ$ and (b) $\psi = 28.4^\circ$ with respect to surface normal, where ψ is the tilt angle. In bold red peaks of the single crystalline ZnO phase are indicated, while the other peaks are from bulk reference position or polycrystalline phase. (c) ZnO bulk wurtzite crystal structure with $(10\bar{1}1)$ surface evidenced and top and side view of crystal cut along $(10\bar{1}1)$.

Fig.2.10(a) shows the radial θ - 2θ scan (with tilt angle $\psi=0^\circ$), which investigates the orientation of film grains along the surface normal. In this case only one peak is clearly visible at 36.71° , corresponding to the position of Bragg diffraction from $(10\bar{1}1)$ planes in wurtzite ZnO structure (bulk 36.253°) [62]. No other peaks are detectable at the positions expected for the bulk wurtzite [arrows in Fig.2.10(a)]. The growth along the normal to $(10\bar{1}1)$ plane can be explained by a small lattice mismatch with the Mo substrate [Fig.2.10(c)]. The unit cell of this surface is rectangular, with $a = 3.25 \text{ \AA}$ and $b = 11.84 \text{ \AA}$, corresponding to a mismatch with Mo(001) of 3% and 6%, respectively. A surface energy of 1.73 J/m^2 has been calculated for $(10\bar{1}1)$, with $E_{(11\bar{2}0)} < E_{(10\bar{1}0)} < E_{(10\bar{1}1)} < E_{(0001)-Zn}$ [57]. It is therefore lower than the surface free energy of the most commonly exposed surface (0001) -Zn in thin films and the growth on other surfaces will be especially unfavored by epitaxy. Exposure of such oblique surfaces have been already reported in literature for nanostructure growth [63]. For atomic arrangement in the bulk crystal lattice, it is obtained that growth rates are in such relation: $V_{(10\bar{1}0)} < V_{(0001)} < V_{(10\bar{1}1)} < V_{(11\bar{2}0)}$ [64], therefore the $(10\bar{1}1)$ is favored with respect to the other small mismatch surface, namely $(11\bar{2}0)$. To confirm orientation of the grains, other reflections expected for a wurtzite with such orientation have been checked, in the hypothesis of single crystalline film. Near tilt angle of 28° (keeping the substrate rotation angle constant), a peak is present at 33.28° , referring to the Bragg reflection from $(10\bar{1}0)$ of ZnO film (expected at 31.770° in bulk wurtzite), corresponding to a reduction of 0.12 \AA of the distance between planes [Fig.2.10(b)] [62].

The shift to higher angles of the Bragg peaks is compatible with a compression in the atomic distances. A small distortion to accommodate strain or an extremely small compression of the O1-O2 or Zn1-Zn2 planes [$d_1 = 0.4127 \text{ \AA}$, $d_2 = 2.4764 \text{ \AA}$, Fig.2.10(c)] to make them more planar could lead to a larger reduction in the $(10\bar{1}0)$ plane distance, compatible with a larger shift. No information is available concerning the in-plane orientation of the grains, because of the small signal, however it is possible to speculate the alignment of the $(10\bar{1}1)$ unit cell reported in Fig.2.10(c) with the Mo[100] directions. In Fig.2.10(b) two other peaks are barely detectable in the noise at 34.78° and 36.28° , corresponding to (0002) and $(10\bar{1}1)$, almost coincident with bulk wurtzite values [62]. The small signal coming from these Bragg reflections and the position unaffected by strain could testify the presence of a polycrystalline phase, probably related to the less abundant metallic Zn oxidized in the annealing, while the main part of the ZnO film underneath is single crystal but with grains too small to give a LEED pattern.

2.6 Conclusions

ZnO thin films between 5 and 70 Å have been grown on Mo(001) by means of molecular beam epitaxy. The influence of the growth parameters, namely oxidizing pressure and agent, temperature, and evolution with thickness on oxidation state, morphology and structure have been investigated.

ZnO grows fully oxidized up to a thickness threshold of 10 Å. The oxidized Mo surface acts as a reservoir of oxygen for Zn. Increasing the amount of deposited Zn and going far from the interface, a fraction of metallic Zn remains in form of islands on the surface, that can be completely oxidized by subsequent annealing. This evidences not only the poor oxidizing conditions during growth, but also the active role played by the Mo substrate. ZnO shows a high quantity of defects, probably related to structural deformations and point defects in the lattice, especially in the first stages of growth. Zn full oxidation can be improved reducing Zn deposition rate or increasing O pressure or substrate temperature up to 500 K. Further increase of temperature induces poor sticking and film desorption from Mo surface. The film shows no long range order in LEED and is composed of small grains with a wurtzite (10 $\bar{1}$ 1) preferential orientation, with a reduced lattice mismatch with Mo(001) unit cell.

Chapter 3

Al-doped ZnO films

In this chapter the focus moves to a different metal-ZnO system, where the metal acts as dopant for the oxide. ZnO doping with III group elements, Al in particular, leads to a material which is both highly transparent and strongly conductive, opening the way to applications as TCO in photovoltaic devices. Additionally, Al-doped ZnO represents an alternative plasmonic material, thanks to its suitable dielectric function value and low losses. Despite the high number of studies concerning optimal performances of the material, both on the applications and on the fundamental properties point of view, some issues remain unclear. First, a systematic work on a wide doping range and with the combination of different techniques is still missing, including the inter-relation between different properties and their dependence on Al-content. Second, the origin of material conductivity is still matter of discussion.

To enlighten both this aspects, Al-doped ZnO films in a wide doping range have been prepared and analyzed with a large variety of techniques, probing electrical, optical and electronic properties. In this chapter the effect of doping on ZnO with the creation of a TCO and a plasmonic material is described. The results concerning electrical, electronic and optical properties as a function of doping with focus on TCO applications are presented in Sec.3.1. In Sec.3.2 an in-depht examination of optical properties by Infrared measurements is reported, showing the high performances of the material for plasmonic applications.

3.1 Al-doped ZnO as a TCO material

Transparent Conductive Oxides (TCO) materials have raised a large interest in recent years for a wide variety of applications as opto-electronic devices components, such as transparent electrodes in solar cells [65, 66], OLEDs [67–69], photonic and plasmonic devices [70, 71] and thin film transistors [72], thanks to their simultaneous high conductivity and high transmittance in the visible range [73]. To date, the best performances have been reached with tin-doped indium oxide (ITO), which represents the present industrial standard with a resistivity of the order of $10^{-5} \Omega \text{ cm}$ and a carrier concentration of the order of 10^{21} cm^{-3} [74, 75]. However, the scarcity and consequent high cost and the toxic nature of indium have promoted the search for alternative compounds, which have been found in ZnO doped with IIIA group elements, like Al [68, 76, 77], Ga [6, 78] and In itself [6, 69], where doping produces a transparent material ($E_g = 3.2 - 3.9 \text{ eV}$) with a high carrier concentration of about 10^{20} cm^{-3} . Among these, Al-doped ZnO (AZO) represents the best choice for this purpose, since aluminum and zinc are common, inexpensive and non-toxic materials, the compound is highly stable and has shown the lowest resistivity and highest carrier concentration [6]. Up to now, best performances for AZO films, prepared by various techniques (magnetron sputtering [67, 68, 77, 79–85], metalorganic vapor phase epitaxy [86], atomic layer deposition [65, 76], spray pyrolysis [87–90] and pulsed laser deposition [91–95] among the others), have been obtained in the 3-4 at.% doping range, with a 90% transmittance in the visible region, a $10^{-4} \Omega \text{ cm}$ resistivity and a 10^{20} cm^{-3} carrier concentration.

Pure and doped ZnO conductivity and optical properties are directly related to electronic structure at Fermi level (FL), which strongly depends on doping [77]. Many studies concerning AZO properties and optimal performances in terms of low resistivity and high transmittance have been performed, however the mechanism which determines AZO conductivity is still matter of discussion. The most accepted picture depicts a shift of the FL above the conduction band (CB) minimum due to the occupation of CB states by electron donated by the dopant, with the consequent appearance of occupied states at FL that allow conduction while preserving transparency (Fig.3.1, model 1) [96, 97]. On the other hand, recent works, both experimental and theoretical, point out the importance of the defects in determining the electrical and optical properties of AZO [91, 98, 99]. These studies investigate the possibility that structural/chemical defects of the AZO matrix can induce an electron population in the vicinity of the Fermi level that leads to effects similar to CBM filling, i.e. drop in resistivity (Fig.3.1, model 2).

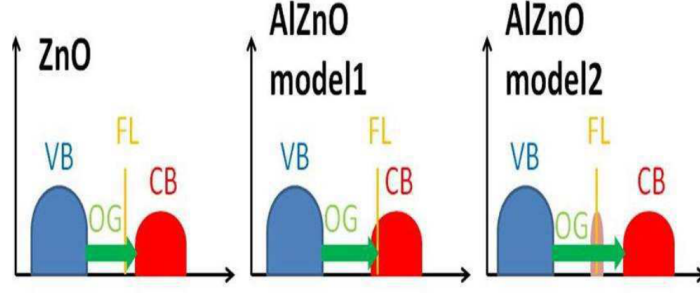


Figure 3.1: Sketch representing (left) ZnO DOS, (central) model 1 for AZO DOS: CB filling and (right) model 2 for AZO DOS: appearance of FL states.

It is very difficult to disentangle between the two different mechanisms because the measurable effects of the two phenomena are very similar. Moreover, in real systems the two phenomena can occur at the same time that complicates even further the investigation. From an electrical point of view it is quite indifferent if the electrons that determine the transport properties belong to conduction band or to impurity states; on the opposite, from optical properties some hints can be obtained. First of all, if the doping induces the appearance of a band in the gap, it should be possible to observe the transitions between this state and the CB. Moreover, optical band gap, defined as minimum energy necessary to excite an electron from valence band (VB) to CB, increases as a result of the Burstein-Moss effect [100,101]: when donors electrons occupy states at the bottom of CB, due to Pauli principle lowest-energy transitions are blocked and optical gap is thus enhanced. A more complete picture of the effect also includes a counteracting narrowing of the gap due to the scattering between charge carriers and ionized impurities: this effect is less relevant than the Burstein-Moss, so the overall effect is a widening of the optical band-gap with increasing electron density [83]. Therefore, if the governing mechanism is the CB filling mode, the optical gap should increase steady with doping. Last but not least, it is possible to investigate the occupied part of the DOS with X-ray Photoemission Spectroscopy (XPS), and, even more interesting, it is now possible to directly observe the DOS at Fermi level and its evolution with doping with Hard X-ray Photoemission Spectroscopy (HAXPES) [102]. In a photoemission experiment the observable effects of doping are mainly two: the appearance of a peak at Fermi energy upon doping and an energy shift of the core levels. If model 1 is correct, due to CB filling in photoemission spectra a peak at FL should appear when ZnO is doped, whose intensity increases as a function of Al content. The occupation of CB by free electron causes a shift of Fermi level, with a consequent shift to higher binding energy (blueshift) of all peaks and VB edge. On the contrary, if donor doping induces the formation of a localized impurity band, following model 2, the energy shift of the core level peaks and of the VB is possible but not intrinsically related to the intensity of this impurity state.

In this debate another point has risen considerable interest: the conductivity of the pure material. In fact, despite being a wide bang gap semiconductor, pure ZnO itself does not show an insulating nature even if expected: a considerable high carrier density up to 10^{21} cm^{-3} and low resistivity (1-50 $\Omega \text{ cm}$) have been reported from various experimental studies [79, 86]. The source of ZnO conductivity has been widely investigated and it has been attributed to the presence of donors such as hydrogen [103], zinc interstitials and oxygen vacancies [104, 105]. While it has been clearly shown that ZnO conductivity exists even when H is absent [104, 105], both theoretical and experimental results highlight the key role of native defects, oxygen vacancies in particular [91, 99, 104, 105]. All these works point out the relevance of defects in determining the electronic properties of pure ZnO and some extend the study also to the doped ZnO films finding, also in this case, a major role of the defects [77, 106].

AZO films have been prepared with a variety of techniques ranging from radio frequency (RF) magnetron sputtering, to metalorganic vapor phase epitaxy, atomic layer deposition, spray pyrolysis and pulsed laser deposition, showing that Al-doped ZnO properties strongly depend on preparation conditions [73]. Best performances in terms of optical and electrical properties for different AZO films are reported in Table 3.1.

| ρ ($\Omega \text{ cm}$) | N (cm^{-3}) | μ_H ($\text{cm}^2\text{V}^{-1}\text{s}^{-1}$) | T (%) | Al content (at.%) | Dep.method (year)[ref.] |
|-----------------------------------|-----------------------------|--|------------|----------------------|--------------------------------|
| 1.9×10^{-4} | 1.5×10^{21} | 22.0 | > 85 | 3 | RF magn. sputt. (1984) [107] |
| 8.2×10^{-4} | 6.2×10^{20} | 9 | > 90 | 4 | RF magn. sputt. (2006) [77] |
| 1.3×10^{-2} | 6.0×10^{20} | 1 | > 85 | 3 | Chem. spray dep. (2002) [87] |
| 8.5×10^{-5} | 1.5×10^{21} | 47.6 | > 88 | 3 | Pulsed laser dep. (2003) [108] |
| 7.3×10^{-4} | 5.2×10^{20} | 16.2 | > 90 | 2 | Atomic layer dep. (2013) [76] |

Table 3.1: *Electrical and optical properties of AZO films. Best values for resistivity ρ , carrier concentration N , Hall mobility μ_H and transmittance T are reported with indication of Al-doping amount and deposition method used.*

Electrical and optical performances also strongly depend on Al content. Resistivity decreases with increasing doping and reaches a minimum at about 3 at.%, then increases again, while carriers number exhibits an opposite trend; mobility, instead, shows a monotonic decrease with increasing Al content (Fig.3.2). The worsening of electrical performances, highlighted by the increasing resistivity for high doping amount has been related to a degradation in crystal quality, confirmed by XRD measurements. This trends have been observed for films prepared both by magnetron sputtering [77, 84] and pulsed laser deposition [93].

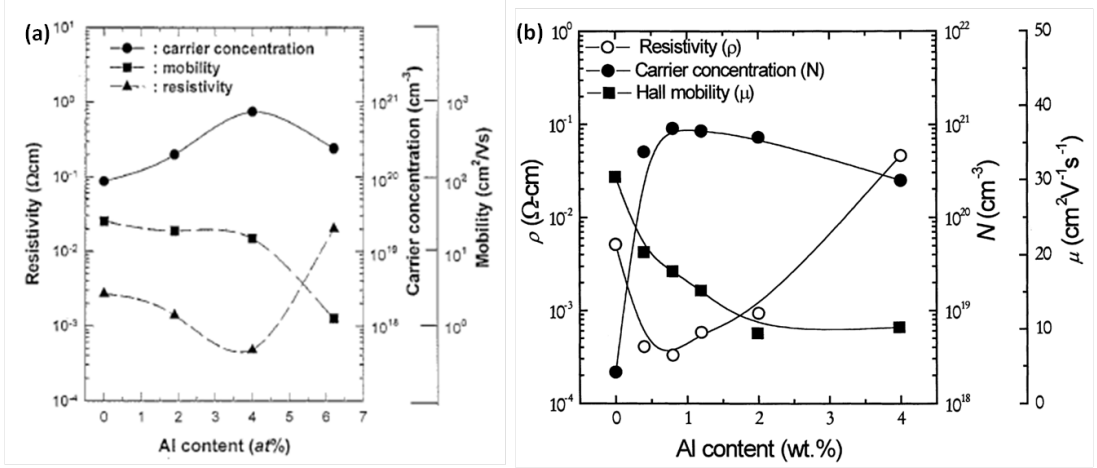


Figure 3.2: *Electrical properties of AZO films as a function of Al doping, deposited by (a) RF magnetron sputtering [84] and (b) pulsed laser deposition [93]. 1 wt.% corresponds to about 3 at.% .*

Optical gap, defined as the minimum energy needed to excite an electron from the valence band to the conduction band, has been reported to increase with increasing Al content. This has been related to the *Burstein-Moss effect*, which consists of the blocking of the low energy transitions due to Pauli principle, which enhances the optical gap by the energy:

$$\Delta E_g^{BM} = \frac{\hbar^2 k_F^2}{2} \left(\frac{1}{m_e} + \frac{1}{m_h} \right) \quad (3.1)$$

where k_F is the Fermi wave vector and m_e and m_h are the effective masses for electrons and holes respectively [100, 101]. Monotonic widening of optical band gap with increasing doping has been reported in various studies [80, 83, 109].

Best performances have been obtained for films deposited by pulsed laser deposition and magnetron sputtering. Both these techniques show high reproducibility, can be performed at low deposition temperature and provide good crystal quality of the deposited films. However, the latter is the most used because of its scalability and cost-to-efficiency ratio, which makes magnetron sputtering a suitable technique also at the industrial level.

AZO films with Al doping ranging from 0 to 14 at.% have been deposited by RF magnetron sputtering on a MgO(001) substrate. Resistivity and optical band gap have been determined as a function of Al content; AZO valence band has been investigated by means of X-ray Photoemission Spectroscopy and Hard X-ray Photoemission Spectroscopy. The wide doping range analyzed and the combined use of different techniques have allowed to directly interrelate the different properties to obtain a complete picture of the system and to gain insight in the mechanisms that governs the behavior of this material, in which so many parameters play a role at the same time.

Experimentals

AZO films have been obtained by co-deposition from a 3" RF magnetron source (ZnO) and a 3" DC magnetron source (Al) operating in confocal geometry at approximately 15 cm from the MgO 2-side polished substrate. A constant 0.7 Å/s ZnO deposition rate was reached at RF power of 120 W. The DC power was varied in order to obtain the desired doping level, ranging from 0 to 14 at.%. Deposition was performed at room temperature with base pressure of 1×10^{-5} mbar, in a 5×10^{-3} mbar argon gas atmosphere; a rotating sample holder has been used to obtain an uniform deposition.

Films have been analyzed by means of electrical measurements, InfraRed (IR) absorption analysis, optical measurements (Ultra-Violet and visible range), X-ray Photoemission Spectroscopy (XPS) and Hard X-ray Photoemission Spectroscopy (HAXPES). Electrical measurements have been performed with a 4-point probes system (SourceMeter Keithley 2400 with W probes) applying a 1-10 mA current for doped films, while a 2-point probe system with 100 V source (SourceMeter Keithley 6517) was used for pure ZnO and 0.4 at.% AZO films, because of their high resistivity values. Prior to measurements Al contacts have been deposited on the films by a shadow mask (pads diam.: 400 μm , pitch 1400 μm , square array). IR absorption measurements have been performed at SISSI beamline at Elettra Synchrotron in Trieste by means of a Bruker 70v Michelson interferometer. Spectra have been acquired at a base pressure of 2.4 mbar, by using different sources, beamsplitters and detectors to cover the range between 100 and 17000 cm^{-1} (corresponding to 600 - 100000 nm). Four regions have been analyzed: Far Infrared (FIR, 10-600 cm^{-1}), by a global source, Si beamsplitter and pyroelectric detector, Mid Infrared (MIR, 400-6000 cm^{-1}) by a global source, KBr beamsplitter and pyroelectric detector, Near Infrared (NIR, 2000-10000 cm^{-1}) by a quartz source, CaF_2 beamsplitter and pyroelectric detector and Visible region (VIS, 10000-17000 cm^{-1}) by a quartz source, CaF_2 beamsplitter and Si diode detector. Aperture has been set to 1 mm, except for VIS range, where 0.25 mm aperture has been preferred due to detector saturation problems. Spectra have been matched to obtain a single curve and measurements have been performed both in transmission and reflection mode and normalized with respect to a reference: blank spectrum for transmission and gold mirror for reflection. IR spectra have been analyzed using a fitting procedure based on Drude-Lorentz Model, by RefFIT software [110]. Optical properties of Al-doped ZnO films have been analyzed by means of an optical setup with quartz lenses. Films have been measured in visible, ultra-violet and near infrared region by using an UV-VIS monochromatic source (Xe discharge lamp 75 W f/4 with 250 mm monochromator and sorting filters to eliminate superior diffraction orders) and Si and InGaAs sensors which allow to cover a range of 300-1100 nm. Spectra obtained in different wavelength ranges with different sensors have been matched to obtain a single curve. Measurements have been performed both in transmission and reflection mode and

each set of data has been normalized with respect to a blank spectrum measured in transmission mode. The measurements of XPS signals were performed in an ultra-high vacuum chamber with base pressure of 1×10^{-10} mbar (see Sec.2.2) using a non-monochromatized Al-K α X-ray source and a hemispherical electrostatic analyzer with an angular acceptance of $\pm 8^\circ$. The overall energy resolution, dominated by the width of the Al-K α line, is about 1 eV. HAXPES measurements have been performed at Galaxies beamline at Soleil Synchrotron in Paris [111, 112]; spectra have been acquired with fixed photon energy of 2.5 keV and the analyzer has been set to pass energy 50 eV. In the adopted experimental conditions the overall energy resolution was about 0.15 eV. The beam was impinging on the sample forming an angle of 87° with the normal to the surface and photoelectrons were collected around normal emission. Films were transported to synchrotrons in a dryer and always kept in a controlled atmosphere when not measured. No treatment in vacuum was performed prior to the experiments.

Doping level has been determined either by XPS and Energy-Dispersive X-ray Spectroscopy (EDS) techniques. EDS spectra have been taken at 20 kV with a X-EDS Oxford INCA-350 system equipped with a Si(Li) detector. In the XPS case, doping has been calculated by measuring intensity ratio of Al2s and Zn3s peaks weighted for cross section values. In EDS analysis, Al content has been determined comparing measured spectra with simulations results (by DTSA-II Gemini software [113]). Since XPS gives a surface measurement (2 nm), EDS values can be considered more reliable, so we refer to the second as doping values. Anyway, for low doping amount ($d < 4$ at.%), data are compatible. Uncertainty on doping values has been set to 0.5% [77].

Results and discussion

Electrical, optical and electronic properties of Al-doped ZnO films have been analyzed. The results will be presented and discussed in the following sections. Main numerical results are summarized in Table 3.2.

3.1.1 The quest for best performances

Electrical and optical properties are crucial for TCO applications in optoelectronic devices. ZnO and AZO films have been analyzed to determine long range resistivity, while IR absorption analysis has allowed to obtain a local measurement of conductivity and thus to compare the results obtained with the previous ones. Optical properties in UV-VIS range have been analyzed to evaluate transmission coefficient and optical band gap. An estimate of films performances have been given by calculating figure of merit values.

| Al content (at.%) | R_s (Ω/\square) | ρ_{4p} ($\Omega\text{ cm}$) | $E_{opt.gap}$ (eV) | BE_{VB-XPS} (eV) | $BE_{VB-HAXPES}$ (eV) |
|----------------------|-------------------------------|---------------------------------------|-----------------------|-----------------------|--------------------------|
| 0 | 5.4×10^9 | 1.46×10^5 | 3.10 | 2.69 | 3.47 |
| 0.4 | 7.1×10^7 | 1.93×10^3 | 3.07 | 2.82 | - |
| 1.6 | 3.4×10^1 | 9.2×10^{-4} | 3.29 | 3.30 | - |
| 1.8 | 4.9×10^1 | 1.32×10^{-3} | 3.30 | 3.37 | 3.64 |
| 3.6 | 2.2×10^1 | 6.1×10^{-4} | 3.45 | 3.47 | 3.68 |
| 5.3 | 4.3×10^1 | 1.16×10^{-3} | 3.48 | 3.27 | - |
| 5.9 | 4.2×10^1 | 1.13×10^{-3} | 3.48 | 3.33 | - |
| 8.0 | 9.3×10^1 | 2.50×10^{-3} | - | 3.30 | - |
| 14.2 | 1.1×10^3 | 2.84×10^{-2} | 3.53 | 3.29 | - |

Table 3.2: Values obtained for electrical, optical and electronic properties of Al-doped ZnO films as a function of doping: sheet resistance R_s and resistivity ρ_{4p} obtained by 4-point probes method, energy gap $E_{opt.gap}$ calculated by optical measurement, VB edge determined with respect to Fermi level by means of XPS and HAXPES techniques BE_{VB} .

Electrical properties

Long range electrical properties of Al-doped ZnO films have been analyzed measuring sheet resistance R_s and calculating resistivity ρ by the simple relation $\rho = R_s t$, where t is film thickness measured by a stylus profiler (270 nm). Resistivity as a function of Al content in the 1.6 - 14.2 at.% doping range is displayed in Fig.3.3.

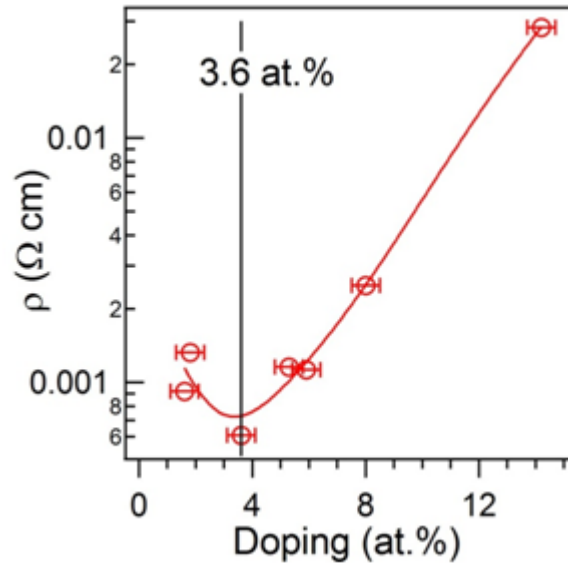


Figure 3.3: Resistivity values for 270 nm AZO films in the 1.6 - 14.2 at.% doping range as determined by 4-point probes method. Resistivity scale is logarithmic. Solid curve acts as guide for the eye.

Pure and 0.4 at.% doping films show a high resistivity value, respectively 8 and 6 orders of magnitude higher than minimum value and therefore not reported in Fig.3.3. This uncommonly high resistance for pure and low doped ZnO, in contrast with the results obtained in previous studies [79, 80, 86], can be related to the stoichiometry of the material: it has been reported that native defects, O vacancies in particular, play a fundamental role in ZnO conductivity [91, 99, 104, 105]. The ZnO and 0.4 at.% AZO films are almost stoichiometric (Zn/O ratio 1.02/1.00, as determined by XPS measurements), which is compatible with a high resistance. To our knowledge only one study [82] reports similar value for pure ZnO film resistivity ($2 \times 10^6 \Omega \text{ cm}$): in that case enhanced insulating properties were attributed to a high oxygen content (1.4%) during deposition, obtained by diluting argon sputtering gas with oxygen. In our case, pure argon was used as sputtering gas and no evidence of a such high oxygen content during deposition has been observed. The origin of this unusual high resistivity can be attributed to an exceptional low defects concentration in our film, even if the reason for this result is not totally clear. This observation is nonetheless remarkable because it shows that high resistivity can be achieved in pure ZnO thin films and therefore these films are suitable for applications where strong insulators are needed.

Al-doped films resistivity is compatible with the values and trends reported in literature [67, 77, 84, 93]: resistivity decreases with increasing doping, reaching an optimal value of $6.1 \times 10^{-4} \Omega \text{ cm}$ around 3.6 at.% and then increases again. The increase of resistivity when Al content exceeds 4 at.% has been related to degradation in crystal quality due to segregation at grain-boundary, where electrically inactive Al atoms act as “electron killers” causing donor passivation and a decrease in mobility [77, 84, 94, 95]. When solubility limit (3-4 at.%) is overcome, interstitial Al defects may appear together with localized filled states in ZnO gap, which increase in number with increasing doping and act as traps for electrons, as shown both by theoretical [95] and experimental [84, 87] works.

Infrared measurements

Local electronic properties have been probed by IR spectroscopy. The measurements have been performed both in Transmittance [T , see Fig.3.4(a)] and Reflection (R , not shown) geometries. The spectra have been analyzed by a simultaneous fit of both T and R [110], based on the phenomenological Drude-Lorentz Model [114, 115], where the dielectric function resulting from all the relevant excitations, both from free (Drude-like) and bound (Lorentz-like) electrons, is described in terms of a sum of harmonic oscillators. The fit of the measured MgO substrate allows to obtain n and k , real and imaginary part of the refractive index of the material, which are then used in a multilayer fit for ZnO and AZO films.

From the fit parameters it is possible to calculate the real part of optical conductivity σ_1 as a function of the wavenumber ω , by the relation:

$$\sigma_1(\omega) = \frac{\omega_p^2 \gamma \omega^2}{(\omega_0^2 - \omega^2)^2 + \gamma^2 \omega^2} \quad (3.2)$$

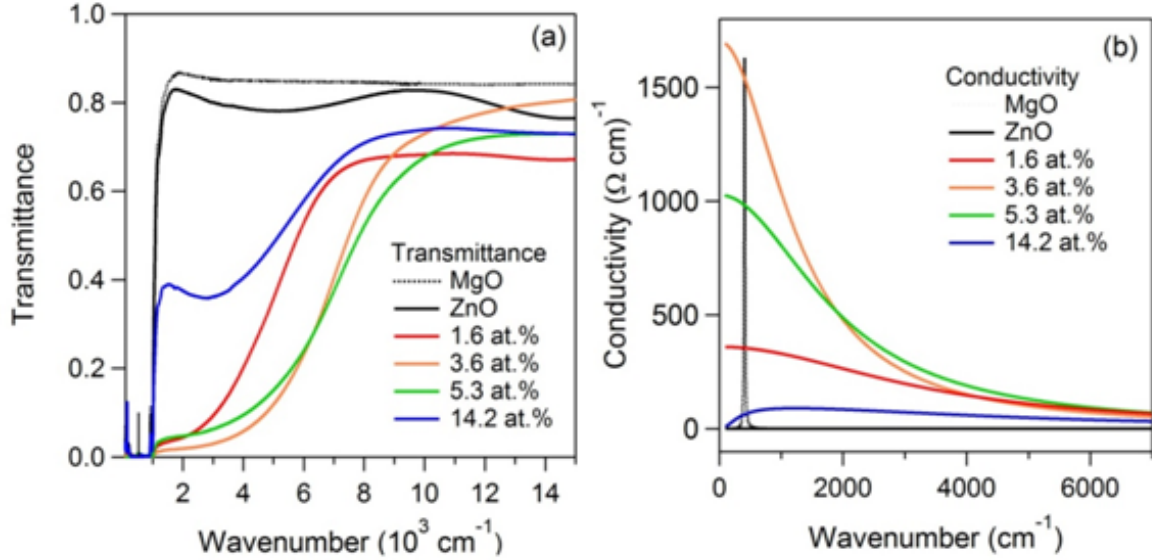


Figure 3.4: (a) Transmittance and (b) conductivity curves for AZO films in the 0 - 14 at.% doping range, obtained from IR absorption spectra analysis.

Fig.3.4(b) displays the optical conductivity σ_1 of the 1.6, 3.6, 5.3 and 14.2 at.% doping films, as well as that of pure ZnO and of the MgO substrate. AZO films with doping 3.6 at.% and 5.3 at.% can be satisfactorily fitted by employing one single Drude term, typical of conventional metallic behavior. The conductivity value at zero frequency corresponds to the electrical conductivity of the film. For 3.6 and 5.3 at.% films, the values obtained are, respectively, 1692 and 1025 ($\Omega \text{ cm}^{-1}$), which correspond to resistivity values $\rho = \sigma^{-1}$ of $5.9 \times 10^{-4} \Omega \text{ cm}$ and $9.8 \times 10^{-4} \Omega \text{ cm}$. These results are in excellent agreement with values obtained by 4-point probes technique, $6.1 \times 10^{-4} \Omega \text{ cm}$ (3.6 at.%) and $1.16 \times 10^{-3} \Omega \text{ cm}$ (5.3 at.%) showing a direct correspondence between local and long range electrical properties. We conclude that the transport properties of the AZO films are dominated by the electronic properties of the bulk AZO and not from morphological configuration (grain size, grain boundaries, etc.). For the 1.6 at.% film, infrared data indicate the presence of an infrared conductivity which is strongly depressed with respect to the 3.6 and 5.3 at.% cases. As in the previous compounds, infrared data can be reasonably well described by employing one single fitting component, even though we cannot conclusively assert whether this term is Drude-like or a finite frequency Lorentzian component.

In order to better reconcile the optical results with resistivity data we decide for the former option. However, even in this case, the dc conductivity [$\sigma = 370 (\Omega \text{ cm})^{-1}$; $\rho = 2.8 \times 10^{-3} \Omega \text{ cm}$] is still off by a factor of 3, with respect to the resistivity measurement ($\rho = 9.2 \times 10^{-4} \Omega \text{ cm}$). The case of the most doped film (14.2 at.%) is even more intriguing: by one side it does not show any Drude oscillator, which is in agreement with the low conductivity value measured with 4-point probes [$\rho_{4p} = 2.8 \times 10^{-2} \Omega \text{ cm}$, $\sigma_{4p} = 35 (\Omega \text{ cm})^{-1}$] but at the same time infrared data provide evidence for the presence of a broad conductivity in the whole infrared range. We rationalize these observations as follows: for high doping values electrons in conduction bands are abundant, but their mobility is likely to be low due to structural disorder, as reported in various studies [77, 93–95, 106]. The pure ZnO film which shows insulator properties, displays no structures in agreement with transport measurements.

It is important to notice that while some localized states are present in the 14.2 at.% and (possibly) in 1.6 at.% compounds, for what concerns the optimally doped compounds (3.6 and 5.3 at.%) IR measurements do not provide evidence for the presence of interband transitions. Thus, within the sensitivity of this technique, no transitions between an in-gap state and the conduction band have been detected. This observation points to a continuous distribution of energetic levels at Fermi level, supporting the CB filling model.

Optical properties

To investigate the evolution of the optical band gap and to determine the value of the optical transmission in the visible range (which is relevant for application purpose) optical measurement in the UV and visible range have been performed.

Absorbance spectra are reported in Fig.3.5 as obtained by the relation: $1 = R + T + A$, where R is reflectance, T is transmittance and A is absorbance. For each doping value, for wavelength λ higher than 450 nm, transmission sets to a maximum at almost 80-90% in the visible range (not shown here), in agreement with other studies [67, 87, 106]. Maximum T value of 87% is reached for 1.8 at.% at 550 nm.

Absorbance spectra show a shift of absorption cut to lower wavelength with increasing doping, as already reported in previous works [87]. Optical bandgap energies can be calculated from the relation $E_{gap} = hc/\lambda_{cut}$, where λ_{cut} is the value of wavelength obtained by linear approximation procedure, as the wavelength value where background line intersects linear fit for absorbance cut (see Fig.3.5). This method is obviously a rough approximation that can lead to some errors in the quantitative estimation of the band gap, however the use of the same procedure for all the analyzed films gives us a good confidence about the evaluation of the relative changes in the optical bandgap value.

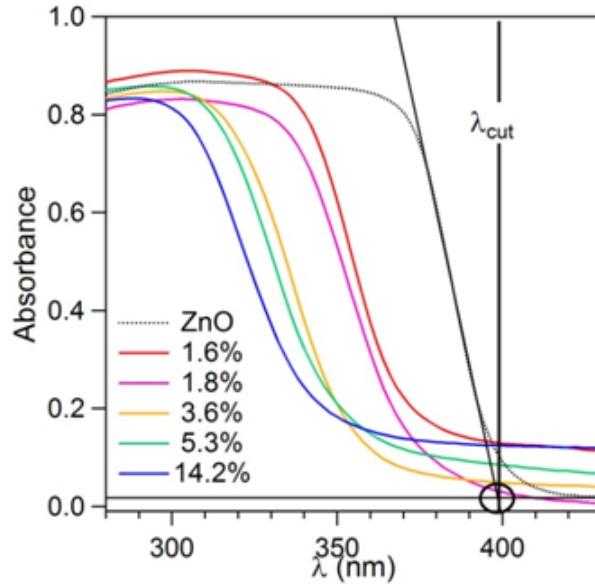


Figure 3.5: Absorbance spectra for AZO films in the 0 to 14 at.% doping range. λ_{cut} determination for pure ZnO film is shown.

As previously mentioned, optical bandgap increases with increasing doping (blueshift) due to Burstein-Moss effect [100, 101], that predicts a widening of optical gap caused by blocking the lowest-energy transitions, as a consequence of the increasing number of donor electrons in CB, as reported in different works [80, 83, 85, 116]. The widening of optical bandgap with increasing doping is thus compatible with the hypothesis of CB filling.

A quick overview of the performances of the analyzed AZO films from an applicative point of view can be given. To rapidly compare the performances of different films as a TCO, a figure of merit (FOM) that takes into account the optical and electric behavior of the material has been developed by Haacke [117]. Figure of merit Φ_H was defined by the relation: $\Phi_H = T_{550}^{10}/R_s$, where T_{550} is transmittance value at 550 nm and R_s is the sheet resistance. With this definition the higher is the FOM, the better are the performances. The highest figure of merit, with a value of $8.3 \times 10^{-3} \Omega^{-1}$ has been obtained for 3.6 at.% film. This value is quite high if compared with other studies ($3 \times 10^{-3} \Omega^{-1}$ [66] and $6.7 \times 10^{-3} \Omega^{-1}$ [76]). Other works prefer a different definition of FOM, proposed by Jain and Kulshreshtha [118]: $\Phi_{JK} = -1/(\rho \ln T_{av})$, where T_{av} is the average transmission value in the 450-800 nm range. Also in this case, the highest figure of merit of $9040 (\Omega \text{ cm})^{-1}$ has been obtained for 3.6 at.% film that has to be compared with films obtained in similar conditions: $9853 (\Omega \text{ cm})^{-1}$ [116], $6000 (\Omega \text{ cm})^{-1}$ [82], $4196 (\Omega \text{ cm})^{-1}$ [81]. These data demonstrate that the AZO films described in this work possess some of the best characteristics ever reported for optoelectronics applications.

3.1.2 Unraveling conduction mechanism

The investigation of valence band and Fermi level regions through surface (XPS) and bulk (HAXPES) sensitive photoemission techniques represents the key issue to unravel electronic properties and determine which is the most suitable model to describe the origin of conductivity in doped ZnO films.

XPS - Surface electronic properties

Surface sensitive XPS has been used to measure Zn2p, Zn3s, Zn3d, O1s, Al2s peaks and valence band region, corresponding to the Zn4p, Zn4s and O2p peaks. The low intensity of C1s peak (barely visible) has confirmed the negligible contribution of the surface contamination to the recorded spectra. Fig.3.6(a) shows the region between -13 and 0 eV, where Zn3d and VB edge are located.

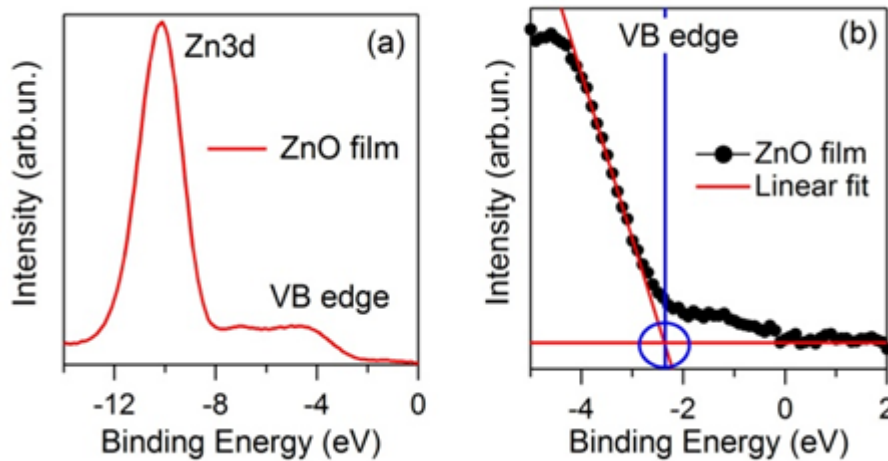


Figure 3.6: XPS spectra taken at normal emission with Al-K α photon for pure ZnO film: (a) VB edge and Zn3d region, (b) linear approximation procedure to determine VB edge energy.

Core peaks Binding Energy (BE) has been determined by using a Voigt fit with a linear background. VB shift has been evaluated by determining VB edge, identified by the value of BE where best linear fit for background line crosses best linear fit for VB edge [linear approximation procedure, shown in Fig.3.6(b)]. BE for all peaks and VB edge were then calculated by subtraction of the measured energy from Fermi Level energy. The Ag3d peak from a clean Ag(001) bulk crystal was used as Fermi energy reference [119]. Error bars on BE determination are 0.1 eV. Zn2p, Zn3s, Zn3d and O1s peaks for Al doped films show a shift to higher BE with increasing doping from 0 to 3.6 at.%, then BE sets to an almost constant value (Fig.3.7). The same trend has been observed for VB edge.

This behavior is very similar to the bandgap evolution as a function of doping level (the bandgap increases with increasing Al content and almost saturates after optimal doping amount) but differs from the observed electrical conductivity, which shows a sharp inversion of trend when the optimal doping level is overcome.

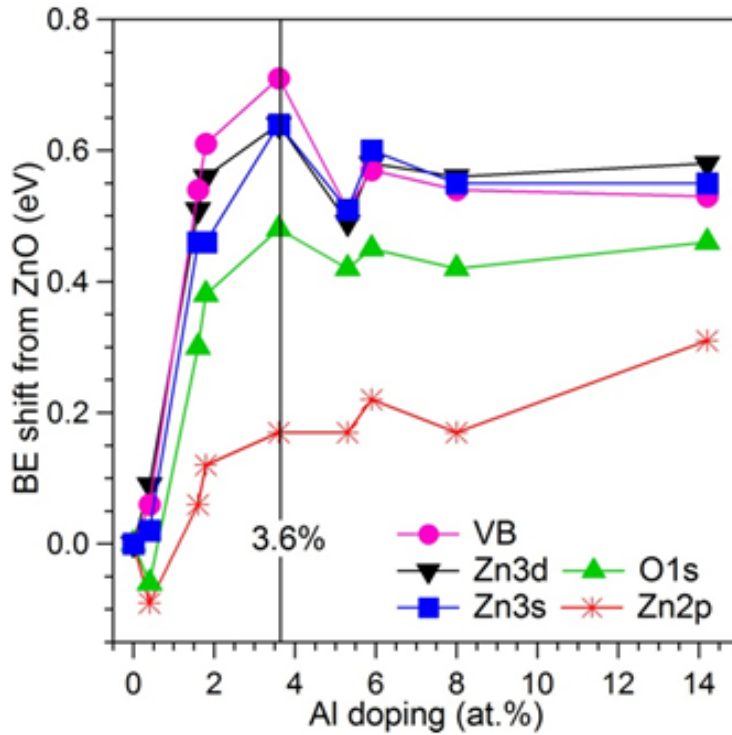


Figure 3.7: Binding energy shift with respect to pure ZnO value for different XPS peaks as a function of Al doping. Error bars on BE are 0.1 eV.

The previous combined observations can be explained as follows: the energy shift of all levels and VB edge is due to Al electrons that are donated to the system as additional free charge and populate the empty conduction band, causing a shift of FL and, consequently a shift of all the levels to higher binding energy. At the same time the filling of the conduction band causes the widening of the optical gap and the increase of the conductivity. The only incongruity in this simple picture is the decrease of the conductivity in AZO for doping values higher than the optimal one, even if all measurements indicate occupation of the conduction band. This is related to the reduced mobility induced by the degradation in crystal quality, rather than from a reduction of the CB population, as confirmed from IR measurements .

HAXPES - Bulk electronic properties

XPS represents a powerful technique for a direct measure of DOS, however, due to its surface sensitivity, it is not a suitable method to study FL region of a bulk material. HAXPES, on the contrary, is a bulk sensitive technique thanks to the employment of hard X-rays and allows to exclude, or at least strongly reduce, band bending and other surface effects or contaminations. Besides, peak at Fermi energy in metal doped semiconducting oxides has been detected so far only by this technique [91,98,120,121]. HAXPES measurements have been performed on pure, 1.8 and 3.6 at.% Al-doped ZnO and spectra of Zn3p, O1s core levels, the valence band and Fermi Level region have been recorded. A survey scan has allowed to verify the cleanliness of the surface by the negligible contribution of C1s peak to the spectra. Spectra have been normalized to the background of the peak.

Zn3p peak spectra displayed in Fig.3.8(a) show very good agreement with the spectra already reported in literature [89]: the visible multiplet structure ($3p_{1/2}$ and $3p_{3/2}$) is more defined for the undoped film, while the metallicity induced by the Al doping causes a broadening of the photoemission peaks resulting in a less defined separation between the $3p_{1/2}$ and $3p_{3/2}$ features. Zn3d peak (located at almost 2484.5 eV KE, -11 eV BE, not reported here) shows a similar broadening. VB and FL regions are shown in Fig.3.8(b). As previously mentioned, HAXPES technique allows to detect the prominent spectral feature at FL for doped films [inset in Fig.3.8(b)], whose intensity increases with doping, as already reported by other studies [91,98]. Differently to what already observed in those experiments, the spectra of pure ZnO do not display any feature at Fermi level.

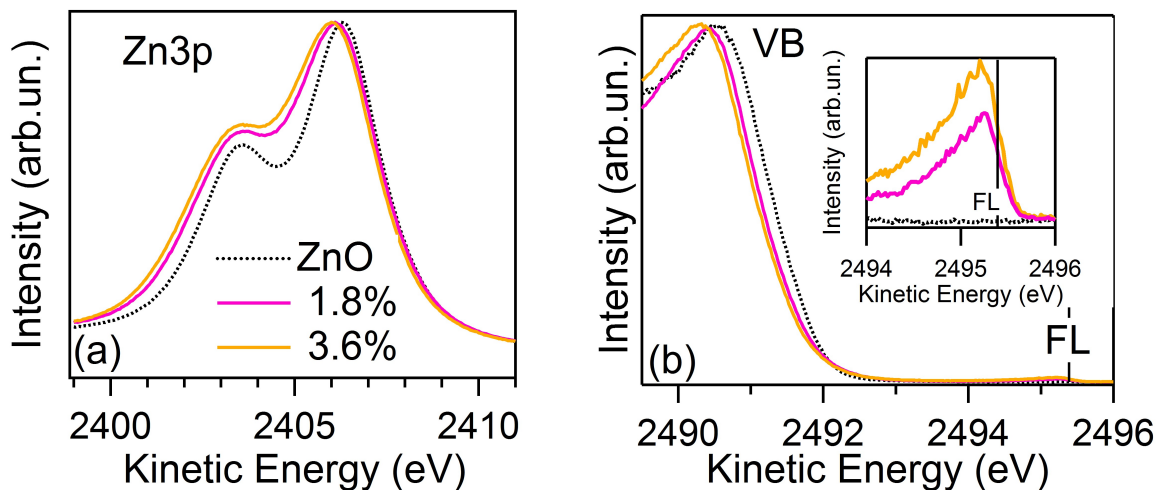


Figure 3.8: Normalized HAXPES spectra of AZO films measured at normal emission. (a) Zn3p peak and (b) VB region. Inset: zoom at FL energy shows a structure, absent in pure ZnO film, whose intensity increases with Al content.

As for XPS measurements, core peaks positions have been determined as a function of doping level. Zn3p, Zn3d, O1s peaks and VB edge show a shift to lower kinetic energies (higher BE) with increasing Al concentration, as already reported in literature [91,98] and confirmed by XPS measurements for these doping values.

Trends and relative variations determined by HAXPES are compatible and absolute values are in good agreement with those obtained with XPS but the shifts are slightly smaller. This discrepancy between the two techniques, particularly evident for O1s and Zn3d peak, can be related to surface effects, which are more relevant in XPS and reduced in HAXPES measurements.

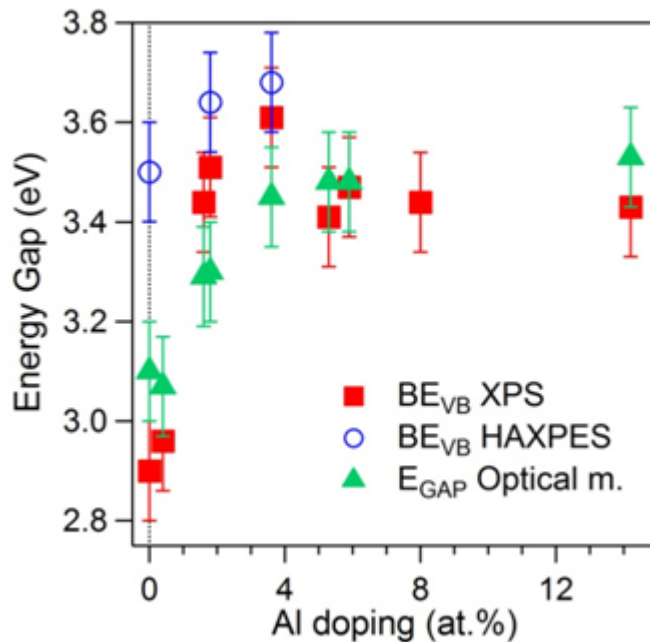


Figure 3.9: VB edge Binding Energy obtained by means of HAXPES (empty dot) and XPS (solid squares) and optical band gap determined from optical measurements (solid triangles), as a function of Al doping. Error bars are 0.1 eV. Trends and relative variations as a function of doping are compatible.

Binding energy corresponding to VB edge obtained by means of HAXPES and XPS techniques and optical band gap determined by optical measurements as a function of Al doping are displayed in Fig.3.9. Trends in the available data range are compatible and a quite good agreement has been observed also for absolute values, except for pure ZnO film. It is not possible to directly compare absolute values obtained in photoemission and optical measurements: one reason is the possible large errors introduced in the estimation of VB position and λ_{cut} values introduced by the linear approximation method; a second reason is related to other effects that could play a role because of the different contribution of empty and filled states in photoemission and optical measurements.

The hypothesis of conduction band filling is compatible with all the previously mentioned evidences in photoemission spectra. The injection of free charge in CB causes a broadening of the peak due to the induced metallicity; all peaks and VB edge shift towards higher binding energy, as a consequence of the shift of Fermi level; the increasing free charge in conduction band determines the increase in FL peak intensity. The results obtained, beside supporting the CB filling model as the most favorable, show the good agreement between different techniques to detect the properties of the material.

Role of defects

In HAXPES experiment spectra have been collected as a function of time. Figure 3.10(a) displays the VB spectra of the AZO 3.6 at.% film recorded at 100 K as a function of acquisition time and 3.10(b) the corresponding Fermi level region.

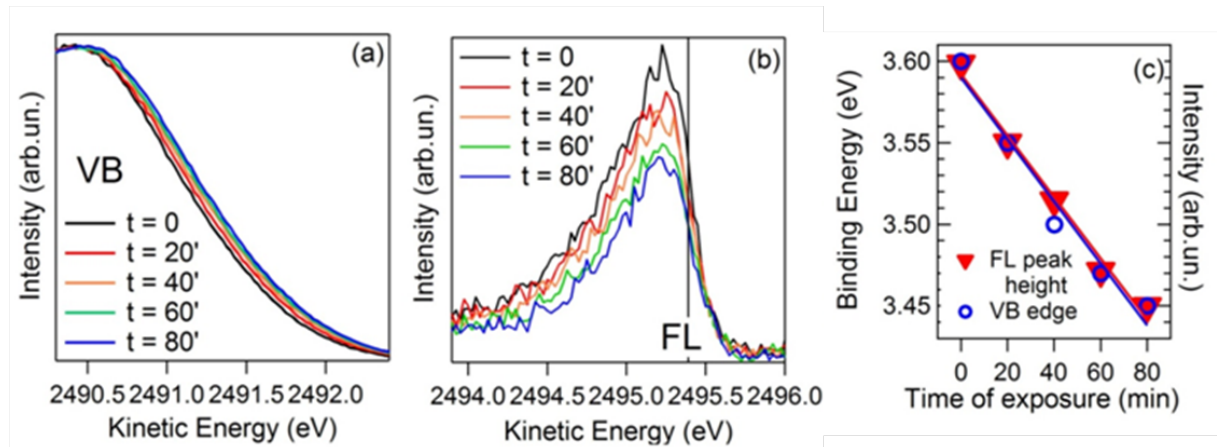


Figure 3.10: 3.6 at.% Al-doped ZnO film: (a) VB edge and (b) peak at Fermi level measured by HAXPES technique at normal emission, for increasing X-rays exposure time. (c) Shift of VB edge and decrease in intensity of FL peak as a function of X-rays exposure time: trends are quite perfectly superimposed.

The spectra show a clear shift as a function of time: in particular the VB edge shifts toward lower BE as the acquisition time increases [about 100 meV in the spectra presented in Fig.3.10(a)]; the same effect is observable for all the other peaks, not shown here. This continuous movement of the spectra toward lower BE is not an instrumental effect (or charging), since the Fermi level does not shift in any of the recorded spectra. Moreover, in addition to the energy shift, a steady reduction of the intensity of the feature at the Fermi level has been observed as a function of time, as shown in Fig.3.10(b). The exact correspondence in linear trends of VB shift and FL peak intensity as a function of time [Fig.3.10(c)] shows a clear correlation between the two effects.

This behavior can be ascribed to the fact that the beam radiation induces the formation of defects in the AZO structure (which number increases with time) that act as electron traps thus depleting the CB visible at FL and causing the shift of the whole photoemission spectrum.

These two combined observations confirm once more that the conduction band filling is the governing mechanism in AZO conductivity and that defects as well as dopants can fill or deplete the CB. It has been excluded that the observed effect is due to electronic modifications directly related to created defects because of the direct correspondence of VB edge, core level shift and FL intensity decrease, which confirm in a very straightforward and convincing way the hypothesis of CB filling.

3.2 Al-doped ZnO as an alternative plasmonic material

In recent years the domain of plasmonics has expanded significantly with the introduction of the related field of transformation optics. [122] Transformation optics applies metamaterials, which means artificial engineered materials with rationally designed compositions, which can direct choose bandwidths of electromagnetic radiation. Potential application of these systems range from imaging with subwavelength resolution, to invisibility cloaks, optical black holes, nanoscale optics and, nonetheless, light concentrators in smart solar cells [71].

The most significant problem in using metals as plasmonic materials resides in the high resistive losses at optical frequencies, which can be described in terms of dielectric function. Both real (ϵ_1) and imaginary (ϵ_2) part of dielectric function have to meet strict criteria: although a negative ϵ_1 value typical of metallic-like properties is required for any plasmonic structure, an extremely negative value is not desirable; at the same time ϵ_2 should be low. A material with purely real dielectric function, which implies zero losses ($\epsilon_2 = 0$) and metal-like behavior ($\epsilon_1 < 0$) would be an ideal candidate to replace metals in most of plasmonic and metamaterial devices. It is impossible to satisfy both this conditions simultaneously at all frequencies due to the causality condition [115], however a material with low losses in the wavelength range required for applications and negative ϵ_1 represents a satisfactory alternative to common metal plasmonic materials. Primary loss mechanism in the near-infrared (NIR), visible (VIS) and ultraviolet (UV) range can be classified as arising from phenomena related to free conduction electrons and bound electrons (interband effect). The Drude-Lorentz theory [114, 115] describes these phenomena in terms of free and bound oscillations of the electrons gas.

Dielectric response of the system is described by oscillators defined by central frequency ω_0 , plasma frequency ω_p and relaxation rate γ , by the relation:

$$\epsilon_\omega = \epsilon_1 + i\epsilon_2 = \epsilon_\infty + \frac{\omega_p^2(\omega_0^2 - \omega^2)}{(\omega_0^2 - \omega^2)^2 + \gamma^2\omega^2} + i\frac{\omega_p^2\gamma\omega}{(\omega_0^2 - \omega^2)^2 + \gamma^2\omega^2} \quad (3.3)$$

where ϵ_∞ is the polarization response from core electrons. Relaxation rate is responsible for scattering/ohmic losses and scales directly with the imaginary part of dielectric function; square of plasma frequency is proportional to carrier concentration (see eq.1.3) and also scales directly with ϵ_2 . Thus, decreasing carrier concentration in metals, or increasing it in semiconductors leads to a significant reduction in losses. From eq.3.3 it is also clear that ϵ_1 scales almost directly with ω_p^2 (or with carrier concentration): reducing carrier concentration would also help in reducing ϵ_1 magnitude. Since for application ϵ_1 has to be negative, the value at which it crosses zero line identifies the range of application of the material and is called crossover frequency, ω_c .

Doped semiconductors possess the required properties: metal-like behavior can be achieved while preserving a low losses value. Al-doped ZnO, in particular, is a suitable material for application in the near-infrared (NIR) range, showing negative real permittivity for wavelength longer than 1.84 μm and very low losses with respect to silver and gold [123,124]. Fig.3.11 displays real and imaginary part of dielectric function for different materials in the 0-2000 nm range: TCOs show better performances with respect to conventional plasmonic metals like Ag and Au and nitrides, both considering ϵ_1 and ϵ_2 . In particular, lowest ϵ_2 has been measured on Al-doped ZnO thin films.

Even if many studies have been performed on AZO, few deal with plasmonic properties, and these are mainly analyzed in the 0-5 at.% doping range [123,125] or focus only on the best performance film composition, thus a complete picture as a function of Al content is missing. Besides, the majority of studies only considers the wavelength range between 100 and 2000 nm (corresponding to a wavenumber range between 4000 and 20000 cm^{-1}) and no works investigating the low wavenumber range (far and mid-infrared regions) have been performed. The possibility to access the low frequency range opens the way to a determination of conductivity and mobility, alternative to Hall or 4-points probe measurements. Besides, IR technique gives a measurement of local properties which can be compared to long range ones obtained by electrical methods.

In this work a deep analysis of AZO plasmonic properties as a function of Al content in the 0 - 14 at.% doping range is performed by IR measurements covering the wavenumber range of Far- Mid- and Near- Infrared and visible region, for a better understanding of material properties and how they relate to film composition. Films have been deposited by magnetron sputtering, which, differently from the most encountered pulsed laser deposition, is a scalable technique also suitable at the industrial level.

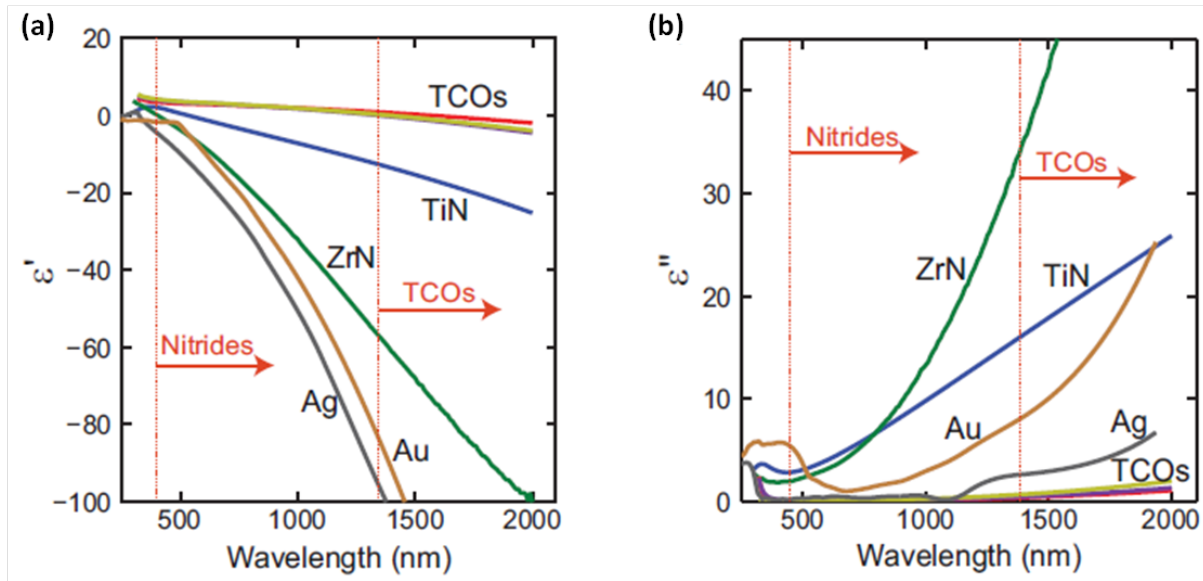


Figure 3.11: Comparison of optical properties of alternative plasmonic materials with those of conventional metals in the 0-2000 nm range. (a) Real and (b) imaginary part of dielectric function of low losses thin films of TiN, ZrN and TCOs (AZO, GZO and ITO) are plotted along with those of gold and silver. The arrows show the wavelength ranges in which nitrides and TCOs are respectively metallic. TCOs have smaller negative permittivity values than those of metals and losses are many times smaller than those in either gold or silver [123]. Red line corresponds to AZO (about 1 wt. %), yellow to ITO, black to Ga-doped ZnO (GZO) [123]

3.2.1 Infrared analysis @Elettra Synchrotron

Infrared absorption is a powerful technique to detect optical properties of the system and to indirectly determine electrical properties. Differently from the information given by techniques such as 4-point probes method or conventional optical measurements, IR absorption investigates local properties and allows to directly relate with the fundamental properties of the material at the atomic level.

IR measurements have been performed at RT in a chamber with an average pressure of 2.4 mbar. Spectra in both transmission and reflection configurations have been acquired with a Bruker 70v Michelson interferometer, by using different sources, beamsplitters and detectors to cover the range between 10 and 17000 cm^{-1} . Four regions have been analyzed: Far Infrared (FIR, 10-600 cm^{-1}), by a global source, Si beamsplitter and pyroelectric detector, Mid Infrared (MIR, 400-6000 cm^{-1}) by a global source, KBr beamsplitter and pyroelectric detector, Near Infrared (NIR, 2000-10000 cm^{-1}) by a quartz source, CaF_2 beamsplitter and pyroelectric detector and Visible region (VIS, 10000-17000 cm^{-1}) by a quartz source, CaF_2 beamsplitter and Si diode detector. Spectra have been measured on pure and Al-doped ZnO films on MgO and on clean MgO substrate, which allows to isolate substrate contribution. In the following paragraphs the procedure adopted to analyze spectra from acquisition to final data is described.

Spectra connection

As an example, spectra obtained for MgO in reflection mode has been shown in Fig.3.12(a). Spectra are partially superimposed, show high noise regions and in some cases the connection between different regions is not perfect.

First, noisy part has been cut, obtaining spectra displayed in Fig.3.12(b). The four regions, after cuts have been made, are FIR:100-1250 cm^{-1} ; MIR:500-4000 cm^{-1} ; NIR:3000-10000 cm^{-1} ; VIS:8700-17000 cm^{-1} . Then, spectra have been connected, multiplying, when required, for the proper factor to obtain a good superposition in common regions. The final level has been chosen so that reflectivity (R), transmittance (T) and their sum did not exceed 1. When $R > 1$, due to saturation of the intense MgO phonon (the structure at about 400 cm^{-1}), maximum intensity has been fixed to 0.95. When phonon intensity did not overcome the value $R = 1$, all the regions have been aligned using FIR as a reference. When the $R+T$ sum was higher than 1, T spectrum has been rescaled to obtain $R+T < 1$. The intense structure at about 1570 cm^{-1} , corresponding to the laser used for the measurements has been removed and finally curves have been interpolated to have 1 point any 1 cm^{-1} between 100 and 1000 cm^{-1} and 1 point any 10 cm^{-1} between 1000 and 17000 cm^{-1} . The final R spectra for MgO is shown in Fig.3.12(c).

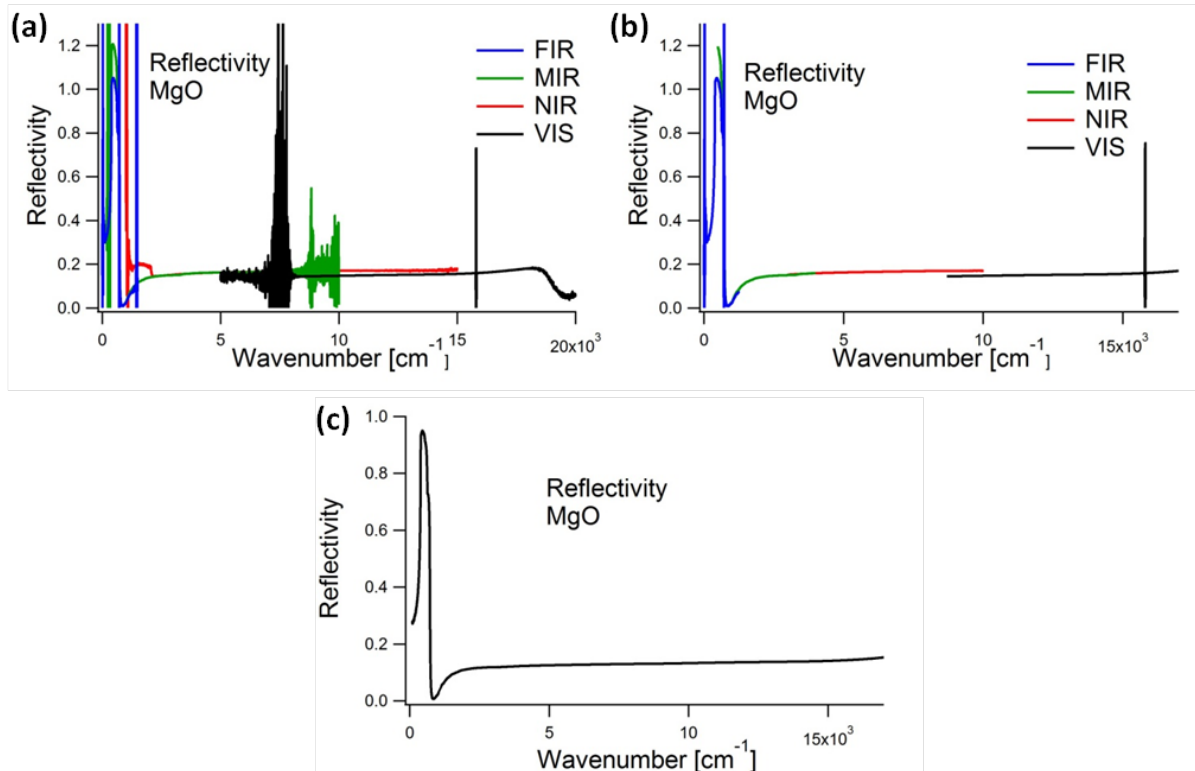


Figure 3.12: Reflectivity spectra for clean MgO substrate. (a) Spectra as collected. (b) Same spectra after removal of high noise regions. (c) Final spectrum obtained by connecting the 4 regions.

Curve fitting and determination of oscillators parameters

The obtained curves have been analyzed through a fit based on Drude-Lorentz Model [114, 115]. In this model dielectric is conceived as a system composed by electrons which are partly bound and partly free. Spectra structures are associated to oscillators, whose describing parameters are the exit data of the fit. The parameters which describe each oscillator are central frequency ω_0 , plasma frequency ω_p and collision frequency γ ; to these parameters dielectric constant at high frequency ϵ_∞ is added, which accounts for the high frequency contributions.

Oscillators with zero central frequency are referred as Drude oscillators and represent free electrons; a non-zero value for central frequency indicates, instead, bound electrons, which correspond to a Lorentz oscillator.

First, the fit has been applied to the substrate, to obtain its contribute in terms of oscillators and calculating the real and imaginary part of dielectric function ϵ and refraction index \tilde{n} . As a reference, for the MgO substrate literature oscillator parameters [126] have been used, having verified the good correspondence with experimental data. From the oscillators parameters, real and imaginary part of the dielectric function ϵ_1 and ϵ_2 can be calculated as:

$$\epsilon_1 = \epsilon_\infty + \frac{\omega_p^2 (\omega_0^2 - \omega^2)}{(\omega_0^2 - \omega^2)^2 + \gamma^2 \omega^2} \quad \epsilon_2 = \frac{\omega_p^2 \gamma \omega}{(\omega_0^2 - \omega^2)^2 + \gamma^2 \omega^2} \quad (3.4)$$

Once dielectric function is known, real and imaginary part of refraction index, n and k , are determined by the following equations:

$$n = \sqrt{\frac{1}{2} \left(\sqrt{\epsilon_1^2 + \epsilon_2^2} + \epsilon_1 \right)} \quad k = \sqrt{\frac{1}{2} \left(\sqrt{\epsilon_1^2 + \epsilon_2^2} - \epsilon_1 \right)} \quad (3.5)$$

Real and imaginary part obtained for MgO substrate are displayed in Fig.3.13.

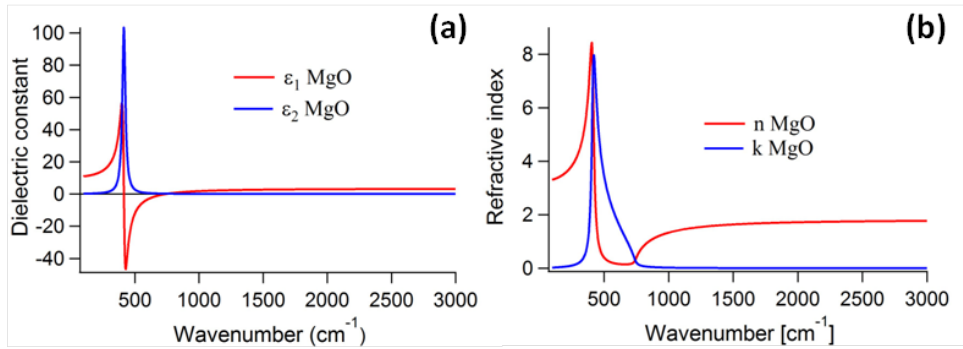


Figure 3.13: Real and imaginary part of (a) dielectric function and (b) refraction index of clean MgO substrate in the $100\text{-}3000\text{ cm}^{-1}$ range.

From MgO data it is possible to obtain a fit for film curves, hypothesizing the oscillators involved in a multilayer model. Layer thickness should be treated as a parameter: here we have set fixed thicknesses of 0.5 mm and 270 nm, for the substrate and film respectively, obtaining satisfying correspondence with experimental data. Fit have been performed with REfFIT software [110], which allows to simultaneously analyze R and T spectra and to have a good conformity with all the available data. An example of data fitting is reported in Fig.3.14. From fitting, oscillators parameters have been determined, which have been used to calculate dielectric function and refraction index of Al-doped ZnO films with eq.3.4 and 3.5.

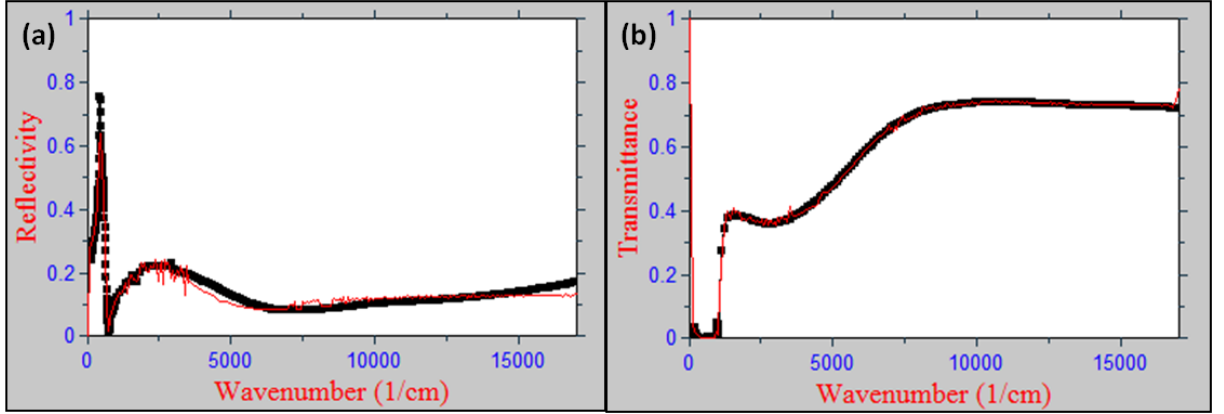


Figure 3.14: Example of curve fitting by RefFIT software for 14 at.% AZO film on MgO: (a) reflectivity and (b) transmittance. Black line: experimental data, red line: result of the fit.

Determination of optoelectronic properties

Besides dielectric function and refractive index, also conductivity, carrier density and mobility can be obtained when a Drude term is present, thus when the material shows a metallic behavior.

The real part of the optical conductivity σ_1 can be calculated from eq.3.2. When the Drude term is present, the real part of optical conductivity at zero frequency corresponds to electrical conductivity and thus this value can be compared to the one resulting from an electrical measurement. Since this technique is a local one, it is thus possible to compare long-range and local conductivity and to determine whether transport properties are dominated by the electronic properties of the bulk or by morphological configuration. The flex in Drude term slope corresponds in turn to screened plasma frequency (bulk plasmon), which is defined as:

$$\omega_p^* = \frac{\omega_p}{\sqrt{\epsilon_\infty}} \quad (3.6)$$

Number of carriers N , in this case electrons, is related to plasma frequency by the relation:

$$\omega_p^2 = \frac{4\pi N e^2}{m_e} \quad (3.7)$$

where m_e is electron mass. In cgs system and with the hypothesis of band mass equal to AZO electronic mass $m = 0.27 m_e$ [127]:

$$N [cm^{-3}] = \frac{\omega_p^2 m_e [cm^{-2}]}{8.962 \times 10^{-14} [cm]} \quad (3.8)$$

Since electrical conductivity can also be expressed in terms of carrier density N , mobility μ and electron charge e by the relation:

$$\sigma = eN\mu \quad (3.9)$$

it is also possible to determine mobility value as:

$$\mu = \frac{\sigma}{eN} \quad (3.10)$$

It has to be remarked that this method is an indirect one and it is possible only under the previously mentioned hypothesis and when materials show marked metallic properties.

3.2.2 Optoelectronic properties

Reflectivity and oscillators parameters

AZO IR measurements of reflectivity are shown in Fig.3.15. 3.6 and 5.3 at.% Al doping films show a high reflectivity at low frequency, which is typical of metallic-like materials. The Drude term, the structure centered on zero frequency, is clearly evident for 3.6 and 5.3 at.% films, while for low doping film it is partially screened by MgO phonon at 413 cm^{-1} . 14.2 at. % AZO does not show any Drude term, but a finite frequency oscillator. Pure ZnO film does not present any structure except for the one assignable to MgO phonon, which highlights the insulating nature of the undoped oxide. The oscillators parameters obtained from the fit of IR measurements on AZO films are reported in Table 3.3, together with screened plasma frequency. The flex in Drude slope in reflectivity spectra corresponds to the screened plasma frequency obtainable from eq.3.6.

Plasma frequency trend as determined by IR technique is in good agreement with first principle calculations from Calzolari et al. [128] for AZO films in an analogous doping range, even if experimental absolute values obtained in the present study are lower [$\omega_P^{exp}(1.6 \text{ at.}\%) = 1.05 \text{ eV}$, $\omega_P^{th}(1.6 \text{ at.}\%) = 1.71 \text{ eV}$; $\omega_P^{exp}(3.6 \text{ at.}\%) = 1.41 \text{ eV}$, $\omega_P^{th}(3.2 \text{ at.}\%) = 2.03 \text{ eV}$ [128]].

Values obtained are also in quite good agreement with other experimental studies, where plasma frequencies of 1.51 eV [125] and 1.74 eV [122] have been measured by ellipsometry at 2 wt.% (about 6 at.%), which are slightly higher than the value of 1.35 eV measured in our study at 5.3 at.%. Since the square of plasma frequency directly scales with both the real and imaginary part of dielectric function, a lower value of ω_P determines both a lower magnitude of ϵ_1 and lower losses, and thus the films prepared and analysed in the present study show high performances in terms of plasmonic properties.

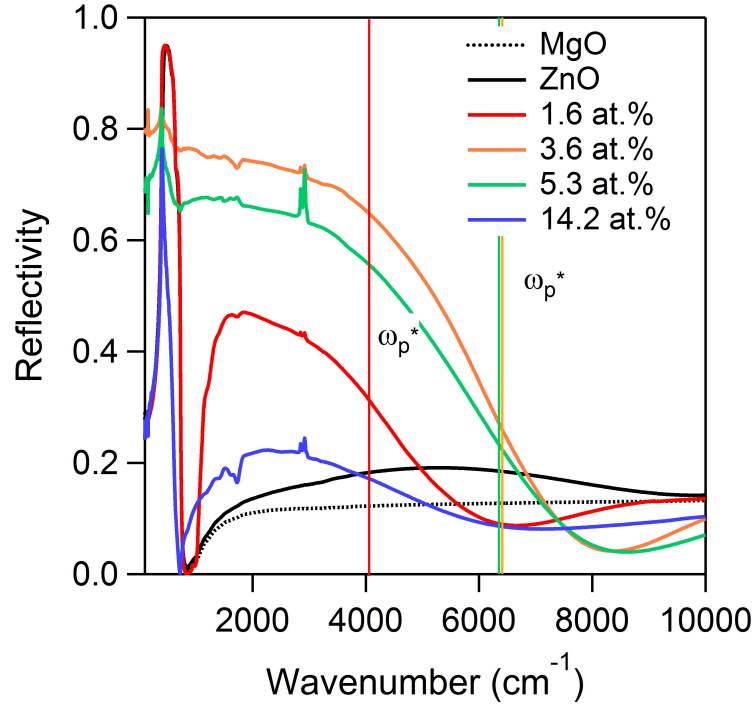


Figure 3.15: Reflectivity spectra for Al-doped ZnO films as a function of doping. Screened plasma frequency is reported for 1.6, 3.6 and 5.3 at.% AZO films as the flex in the slope of Drude term.

| Al content (at.%) | ω_0 (cm^{-1}) | ω_p (cm^{-1}) | γ (cm^{-1}) | ω_p^* (cm^{-1}) |
|----------------------|-----------------------------|-----------------------------|---------------------------|-------------------------------|
| 1.6 | 0 | 8481 | 3330 | 4061 |
| 3.6 | 0 | 11306 | 1251 | 6411 |
| 5.3 | 0 | 10838 | 1906 | 6353 |
| 14.2 | 1158 | 6391 | 6888 | - |

Table 3.3: Values obtained for oscillator parameters of Al-doped ZnO films: central frequency ω_0 , plasma frequency ω_p and collision frequency γ . Screened plasma frequency ω_p^* is also reported. Pure ZnO, which does not present any oscillator is not reported.

Carrier density and mobility

From eq.3.8 and 3.10, number of carriers and mobility for films which show metallic-like properties can be calculated. The results obtained are reported in Table 3.4.

| <i>Al content</i> (at.%) | ρ_{4p} (Ωcm) | ρ_{IR} (Ωcm) | N (cm^{-3}) | μ ($\Omega cm^2 (Vs)^{-1}$) |
|-----------------------------|--------------------------------|--------------------------------|----------------------|--------------------------------------|
| 1.6 | 9.2×10^{-4} | 2.8×10^{-3} | 2.5×10^{20} | 10 |
| 3.6 | 6.1×10^{-4} | 5.9×10^{-4} | 3.9×10^{20} | 27 |
| 5.3 | 1.16×10^{-3} | 9.8×10^{-4} | 3.5×10^{20} | 18 |

Table 3.4: Values obtained for electrical properties of AZO films: resistivity measured by 4-point probes method ρ_{4p} and determined by IR analysis ρ_{IR} , carrier density N and mobility μ .

AZO films properties are compatible with the expected trends for carrier density and mobility. As already reported by other studies [77, 84, 93], the number of carriers increases with increasing doping until solubility limit (3-4 at.%) is reached, then decreases again, while resistivity follows an opposite trend. These trends are in agreement with the previously considered hypothesis (Sec.3.1). Even if N values are not very high if compared with literature ones (see Table 3.1), mobility results can be considered quite satisfying for films obtained with rf magnetron sputtering deposition method.

Dielectric function

Dielectric function is a fundamental parameter to describe the optoelectronic properties of a material. In particular, it is a complex function, whose real and imaginary part (ϵ_1 and ϵ_2) are related, respectively, to the metallicity of the material and the resistive losses. As previously highlighted, a material with negative and small real part and low imaginary part of dielectric function would be an ideal candidate to replace noble metal in plasmonic applications. Real and imaginary part of dielectric function for AZO films, calculated from oscillator parameters as obtained from eq.3.4 are displayed in Fig.3.16.

Real part of dielectric function in metals annihilates at ω_0 and ω_p ; in semiconductors like Al-doped ZnO ϵ_∞ , which includes contribution of high frequency oscillators, is not equal to 1, thus ϵ_1 crosses zero at a different frequency, called crossover frequency ω_c . Since for applications real part of ϵ has to be negative, crossover frequency delimitates the range of utilization of the material: ω_c has to be higher than desired work frequency. Referring to telecommunications window: $\lambda_c < 1.55 \mu m$, $\omega_c > 6450 cm^{-1}$. This condition is verified for 1.6 and 3.6 at.% AZO films, with $\omega_c = 7800 cm^{-1}$ and $\omega_c = 9010 cm^{-1}$, respectively, while 5.3 at.% Al-doped ZnO film presents a too low crossover frequency ($\omega_c = 6060 cm^{-1}$) to be used in these applications.

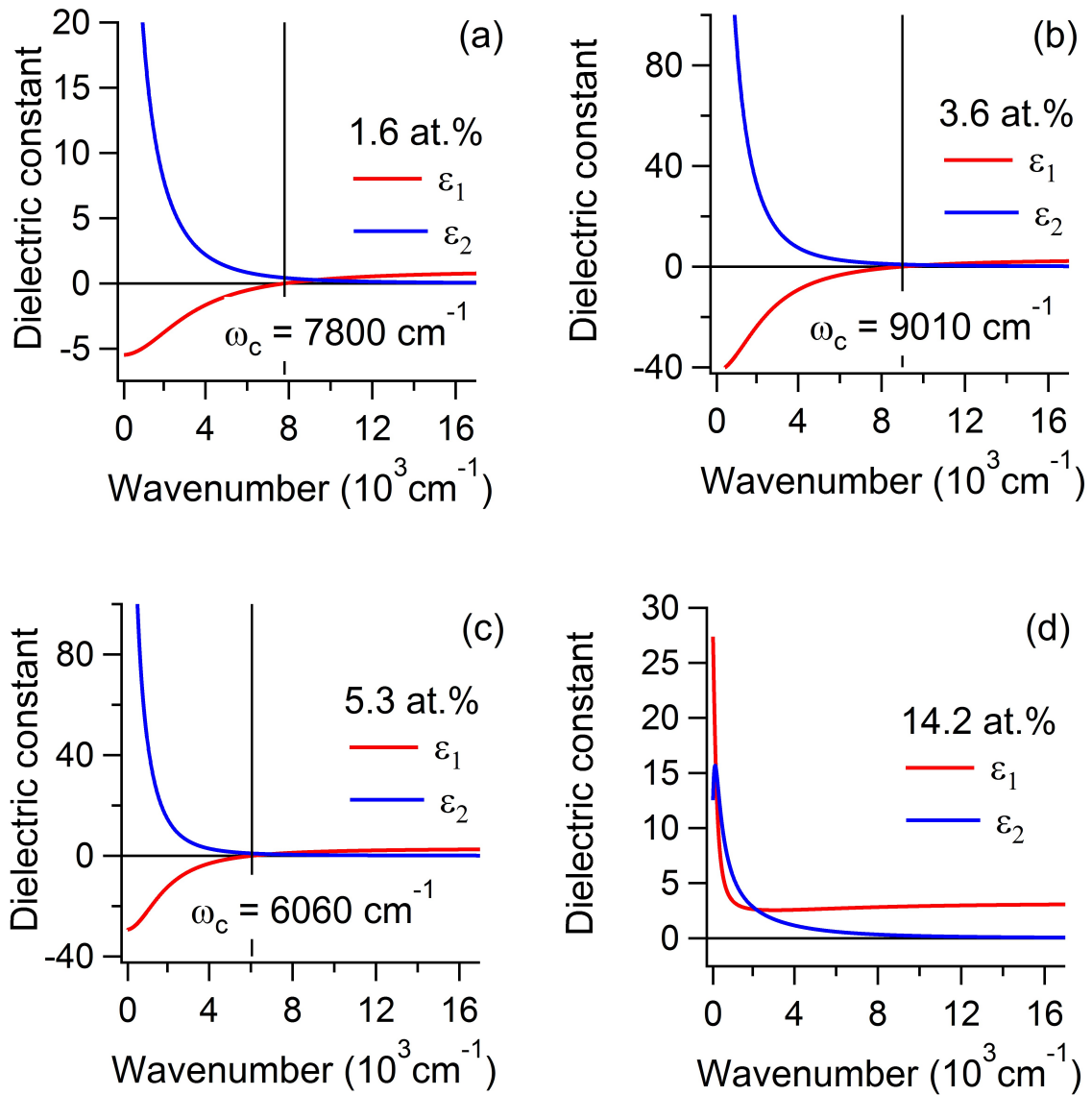


Figure 3.16: Real (ϵ_1) and imaginary (ϵ_2) part of dielectric function of Al-doped ZnO films, as a function of wavenumber. (a) 1.6 at.%, (b) 3.6 at.%, (c) 5.3 at.% and (d) 14.2 at.% Al content. Crossover frequency ω_c is also reported for 1.6, 3.6 and 5.3 at.% AZO films.

ϵ_1 diverges at zero frequency, as expected for the formation of a free electron gas for all films except 14.2 at.%, which, in fact, does not show a metallic-like behavior.

Comparing functions obtained in this work with theoretical ones at 1.6 and 3.2 at.% Al doping [128], real and imaginary part of dielectric function follow the same trend, even if in theoretical case crossover frequencies are higher.

Values obtained can be compared with those measured on Ag. In our case, considering NIR region, which is the most used in applications:

$$|\epsilon_1| > 1.7(1.6at.\%), 9.2(3.6at.\%), 3.1(14.2at.\%)$$
$$\epsilon_2 < 2.2(1.6at.\%), 7.6(3.6at.\%), 2.8(14.2at.\%)$$

While, for Ag [123]:

$$|\epsilon_1| > 100$$
$$\epsilon_2 < 8$$

Thus, 1.6 and 3.6 at.% have proven to possess suitable characteristics to be used as a valid alternative to silver in plasmonic applications in telecommunications and as effective transparent conductive oxides, thanks to the lower ϵ_2 , leading to lower losses, and the small negative real permittivity ($\epsilon_1 < 0$). Additionally, AZO films plasmonic properties can be tuned by changing Al-doping, which allows the access of different optical ranges.

3.3 Conclusions

A complete study of electrical, optical and electronic properties of Al-doped ZnO films in a wide doping range has been presented. AZO films with Al content ranging from 0 to 14 at.% have been deposited by magnetron sputtering on MgO and analyzed by means of various techniques for a better understanding of both the fundamental properties of the material and the improvement of devices performances.

The electrical and optical measurement of the films have shown the typical behavior of AZO as a function of doping: a reduction of resistivity to the optimal value at 3.6 at.% without reducing the transparency of the material in the visible range. Undoped films display exceptionally strong insulating properties demonstrating that previously reported conduction of pure ZnO is related to material defectivity which is not intrinsic and that good insulating ZnO film can be prepared.

The mechanism that governs the properties of the doped AZO film has been investigated by optical measurements and photoemission spectroscopy. HAXPES measurements have clearly demonstrated that induced defects in ZnO matrix can modify the population at

Fermi level thus playing a crucial role in determining the conductivity of the material. On the other side, but not in opposition, the direct relation between photoemission intensity at Fermi level and the photoemission peaks energy positions support the so called CB filling model as the absence of interband transitions in the optical measurements indicates. In this view the shift of the conduction band is responsible for the fancy properties of Al doped ZnO films, rather than the appearance of in-gap defects related new bands.

A high transmittance has been measured ($>85\%$ in the visible range) and reflectance has been analysed in a wide wavenumber range, from Far-Infrared to visible region. Relevant optoelectronic quantities have been determined by a fitting procedure based on Drude-Lorentz Model. Plasma frequencies obtained are in good agreement with both theoretical and experimental studies, and the low values testify the high performances of AZO as a plasmonic material. Plasma frequency trend as a function of doping corresponds to analogous trends in carrier density and mobility, which both show the highest value at 3.6 at.%.

Optical conductivity at zero frequency has been compared to electrical value obtained by 4-point probes method, highlighting a direct correspondance between local and long range electrical properties, which testifies that transport is dominated by electronic structure rather than morphological configuration.

The wide doping range considered has allowed to obtain a complete picture of the evolution of optoelectronic properties as a function of Al content. Besides, the use of a scalable technique creates a connection within the study of fundamental properties of the material and possible industrial applications.

Chapter 4

Ag NP/Oxides

The last part of this study is dedicated to Ag/oxide systems, in particular to the growth of silver nanoparticles on different oxide substrates, exposing different crystal planes: a wide band gap insulator ($E_g=7.8$ eV), MgO(001), a wide band gap semiconductor ($E_g=3.7$ eV), ZnO(10 $\bar{1}$ 0), and an intermediate situation oxide ($E_g=5.6$ eV), ZrO₂(0001).

Ag NPs and nanostructures in general have been largely studied on a variety of substrates. Wide band gap oxides, first of all MgO(001) [23, 24, 129–135] and Al₂O₃ [24, 131, 136] have been chosen preferentially, but also wide band gap semiconductors like TiO₂ [136] and ZnO [136–138] have been studied.

Silver/oxide systems show interesting plasmonic properties, which depend on substrate material and on size, shape and distribution of NPs. The choice of a different oxide affects not only the dielectric response of the system introducing a break of symmetry for the presence of an interface, but also influences cluster growth, in terms of particle shape, density and dimensions. It has been reported that adhesion increases with narrowing of the band gap, thus, NPs with lower aspect ratio are expected to grow on a more insulating material. Additionally, different exposed crystal planes can lead to the growth of different crystal structures: Ag most stable crystal structure is face centered cubic (fcc) phase, with lattice parameter $a = 4.09$ Å, thus a growth on, i.e., square fcc(001) or triangular fcc(111) surfaces can be favoured by different substrate structures and exposed planes.

In our study three different oxide have been chosen, which differs for both bandgap and crystal structure and Ag NPs have been deposited on them by MBE and analyzed *in situ*, to determine the effect of deposition conditions and temperature treatments to morphological and structural properties of the material. Due to the high insulating nature of the oxides, MgO and ZrO₂ have been prepared in the form of thin films on a metal substrate (Mo and Pt₃Zr, respectively) , which allows to perform electrons-based techniques like STM and EELS, while for ZnO the lower band gap does not prevent to use this technique even on a bulk oxide crystal.

The first section is dedicated to the study of Ag/ZrO₂. This system, relevant for the catalytical applications of zirconia, has been prepared and analyzed at Vienna Institute of Technology, where highly consolidated procedures to prepare ZrO₂ film by oxidation of the Pt₃Zr alloy and to analyze STM images have been developed. The STM analysis method developed and tested on this system, described in Sec.4.1, has also been applied to the other Ag/oxides systems to determine morphological properties.

Ag/MgO/Mo has been chosen as a prototypical metal-oxide system, due to the high consolidated experience of the Modena group on the MgO/Mo system, which has allowed to use a reproducible procedure for the preparation of the MgO film and to obtain a simple model system. The analysis on Ag/MgO system prepared and analyzed at SESAMo lab is presented in Sec.4.2, where growth of nanoparticles has been described in terms of morphological parameters determined by STM technique, with the procedure developed at Vienna Institute of technology. Plasmonic properties have been analyzed *in situ* by means of EELS technique, whose results have been compared with the one of a simulation performed with *GranFilm* [131] software to obtain a complete picture of the dependence of optical properties on NPs features.

The analysis skills achieved for the Ag/ZrO₂ and Ag/MgO systems have been exploited to comprehend the more complex Ag/ZnO system, described in Sec.4.3. In this case silver NPs have been deposited on an oxide bulk crystal exposing (10 $\bar{1}$ 0), developing a procedure for surface preparation and determining the best conditions to obtain a high quality oxide crystal structure. Ag/ZnO represent a model system for the applications of plasmonics NPs in photovoltaic cells like DSSC and thus the understanding of the interaction between metal and oxide is fundamental to improve the performances of devices. Ag/ZnO system has been prepared and analyzed by STM and EELS techniques, relating morphological to plasmonic properties.

4.1 Ag/ZrO₂: a case study for morphological analysis

Metal-oxide systems with plasmonic properties are largely used in photocatalysis, associating metal NPs to a catalytic material. Zirconium oxide, ZrO₂, which is a catalyst support and a catalyst on its own, represents a very interesting material to this purpose. When doped with trivalent metals (Y, Sc), or at high temperatures, zirconia becomes an ionic conductor, while remaining an electronic insulator, a property which makes this material suitable for the application in solid state electrochemistry, in solid oxide fuel cells and gas sensors.

ZrO₂ bandgap is between 5.5 and 6.5 eV, depending on the crystal structure, thus the low electric conductivity does not allow to perform electron-based methods: the study of the material in the form of a thin films on a metal substrate can overcome this problem. Since zirconium is quite difficult to evaporate in ultra-high vacuum, Antlanger et

al. developed a preparation method in which a ultrathin ZrO₂ is grown by oxidation of a Pt₃Zr(0001) superalloy [139]. The film obtained is a O-Zr-O trilayer, with an in-plane contracted fluorite structure exposing ZrO₂(111) plane. A reconstruction of the surface is observed, due to the presence of Pt islands on the substrate which induce corrugation of the film (Fig.4.1).

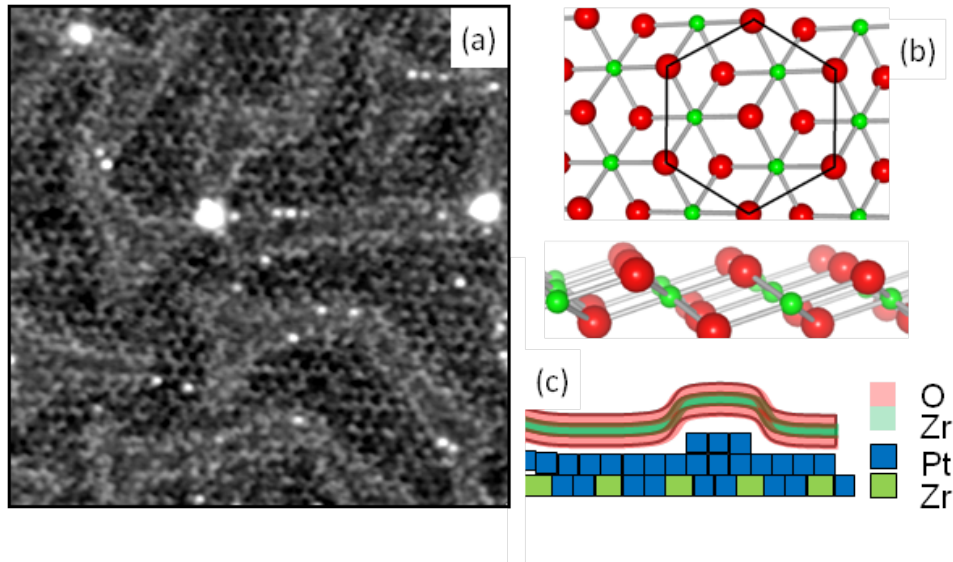


Figure 4.1: (a) $(10 \times 10) \text{ nm}^2$ STM images of the ZrO₂ film obtained by oxidation and annealing of the Pt₃Zr(0001) surface (2 V, 0.1 nA). (b) Schematic representation of the crystal structure of the film, top and side view. (c) Schematic representation of the corrugation of the trilayer induced by the presence of Pt islands on the substrate [139].

Even if some studies concerning the association of Ag to zirconia and the effects on catalytic properties have been performed [67, 140–142], to my knowledge no analysis about the growth of silver in UHV conditions can be found.

In this work Ag/ZrO₂ system has been prepared and analyzed by means of Scanning Tunneling Microscopy. STM is a well known technique, which allows to determine the morphology of the sample and, when atomic resolution is reached, also information about chemical composition. From STM measurements it is also possible to obtain information on the crystal orientation of the material, in an indirect way. The information about NPs size, shape and distribution are of significant relevance in the study of plasmonic properties of the system, thus the morphological analysis represents a fundamental starting point for a better understanding of NPs properties.

The method developed for the Ag/ZrO₂ case study has been applied to Ag/MgO/Mo and Ag/ZnO to relate morphological and plasmonic properties (Sec.4.2 and 4.3).

4.1.1 Experimental apparatus @IAP Tu-Wien

The preparation and characterization of Ag/ZrO₂ system have been conducted at the Institute for Applied Physics (Institut für Angewandte Physik, IAP) at Vienna University of Technology.

All the experiments have been performed in a double UHV chamber (Fig.4.2), where samples have been prepared and analyzed *in situ* at a base pressure of 1×10^{-10} mbar. The analysis chamber features components for standard sample preparation (Ar⁺ ion sputter gun, electron beam heater, leak valves), an RT Omicron STM, a hemispherical analyzer for XPS and LEIS (low-energy ion scattering) and a cylindrical mirror analyzer with coaxial electron source for AES and LEED optics. The preparation chamber is equipped with an ion source for sputtering, three electron-beam evaporators and a gas cracker for atomic oxygen or hydrogen. Sample heaters (electron bombardment of the sample plate, up to 1500 K) are available in both chambers. For oxidation, a directional doser with a microcapillary plate in close proximity to the sample can be used; the pressure at the sample position is estimated as 1×10^{-7} mbar at a chamber pressure of 5×10^{-9} mbar.

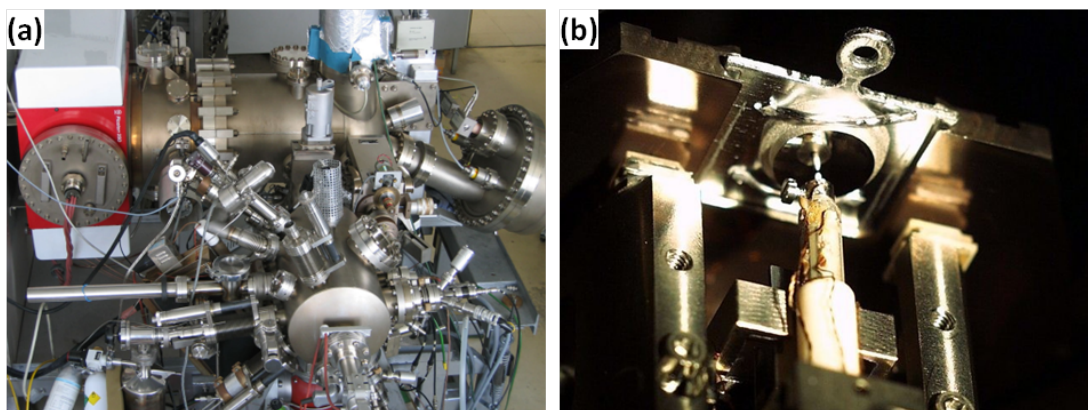


Figure 4.2: (a) View of the UHV apparatus: the preparation chamber is in front, the big chamber contains STM. (b) Photography of the STM stage in UHV chamber. The tip (from bottom) is mirrored by the polished sample surface; the scanner tube is below.

4.1.2 STM analysis procedure

STM images have been measured at RT in constant current mode (0.05-0.1 nA) with electrochemically etched W tips and then analyzed by using three different softwares (ImageJ [143], SPIP [144] and WSxM [54]) determining morphological parameters with the most suitable method, in each case. Procedures applied have been inspired by the work by Napetschnig et al. [145] on Pd and Co clusters on NiAl(110), with some variations related to specificity of the investigated systems. A background has been subtracted to the images prior to any analysis. Reported cluster thickness is the nominal one, as evaluated by quartz-microbalance estimation.

Preferential sites, density and coverage

Cluster density can be generally calculated by counting the number of clusters and dividing by the nominal area of the image. All three softwares used allow to select clusters and count them. Selecting clusters is rather simple when they are few in number and all equivalent, however, in some cases, there are different clusters types, which should be treated separately. This is the case of Ag/ZrO₂: when 0.3 Å (0.1 ML) silver is deposited on zirconia surface at RT three cluster types are clearly distinguishable, which differ for the preferential site for adsorption (Fig.4.3).

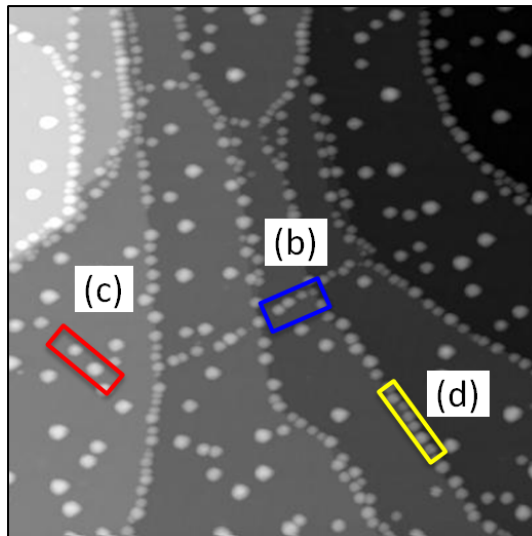


Figure 4.3: $(200 \times 200) \text{ nm}^2$ STM image of 0.3 Å Ag/ZrO₂ (0.5 V). Three different cluster types can be distinguished for the preferential site for adsorption: (c) center of terrace (inside red rectangle), (b) border (blue rectangle) and (d) domain boundary (yellow rectangle).

Clusters labeled *c* (red) are situated in the central part of a terrace and they're mostly bigger than the other ones. Clusters labeled *b* (yellow) choose terraces borders as a preferential site, they look smaller than *c*-type clusters and more close to each other. Clusters labeled *d* look very similar to *b*-type ones and are located on lines which can be identified as domain boundaries. Terraces borders and domain boundaries appear as line on the surface, but can be distinguished from each other by the step height and the orientation of atoms on the substrate. While terraces step height is about 4 Å, domain step height is less than 1 Å [Fig.4.4(b-d)]. Besides, in some of the images, proper contrast settings can highlight the presence of different orientations of substrate atoms, with 120° rotational angle, confirming the presence of domain boundaries which act as preferential sites for clusters [Fig.4.4(a)]. Domain boundaries go across the terraces from one border to the other and have been reported for all the preparation conditions.

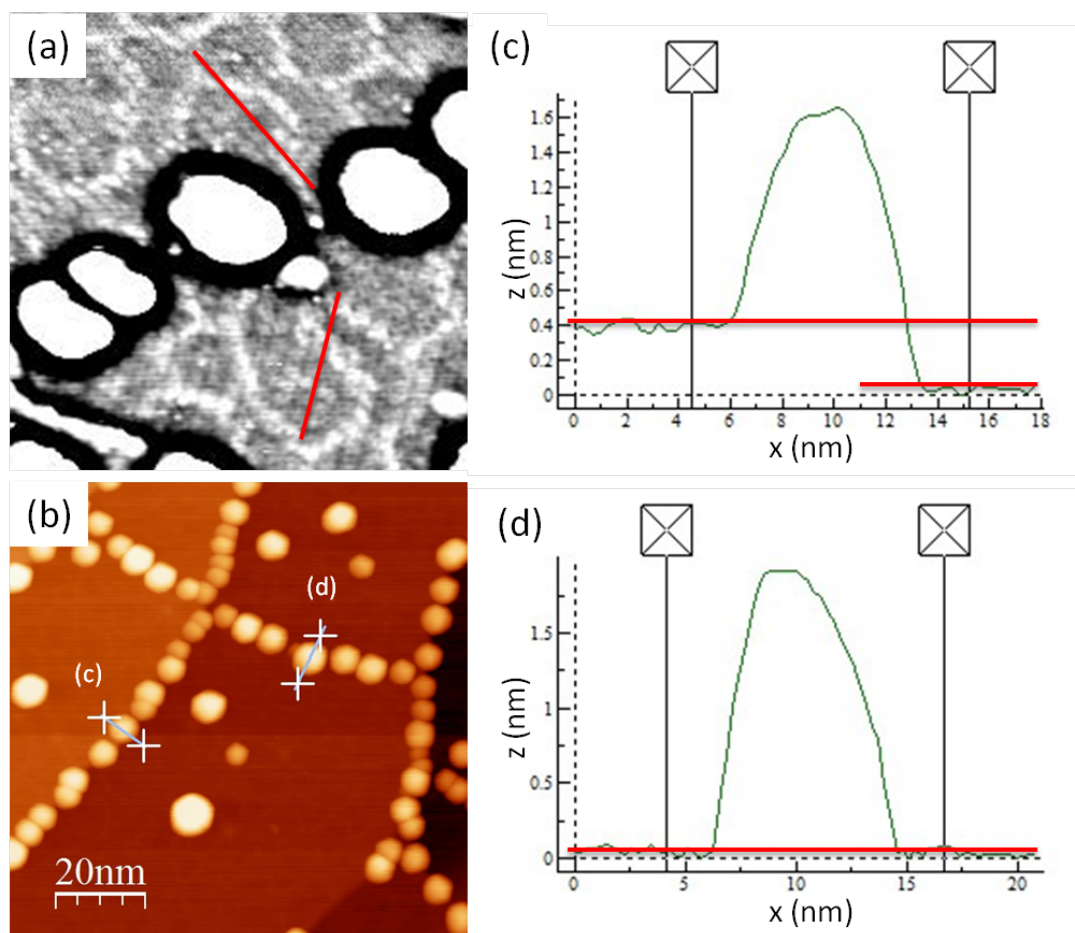


Figure 4.4: 0.3 \AA Ag/ZrO₂. (a) $(25 \times 25) \text{ nm}^2$ STM image with contrast setting highlighting rotational domains (1.5 V). (b) $(100 \times 100) \text{ nm}^2$ STM image where both domain boundaries and terraces steps are present (-1 V). Lines and crosses indicate the corresponding line profiles and cursors, respectively, for (c) terrace step and (d) domain boundary. Height steps of 4 and 1 Å, respectively, allow to distinguish the two cases.

In a case like this, different cluster types should be treated separately, thus it is not possible to use an automatic selection of NPs by software and it is also necessary to redefine density in a proper way. The image was then divided into different parts, each one containing only one type of clusters, so that the calculated cluster density of each cluster type is the density clusters should present if the whole image was occupied only by that cluster type. Since b- and d-type cluster are located on lines, the corresponding area was calculated by measuring the lengths of these lines and multiplying it by the average cluster diameter. The total area occupied by b- and d-type clusters has been subtracted to the total nominal image area, obtaining the area occupied by c-type (Fig.4.5).

Coverage is related to cluster density and size and represents the fraction of surface covered by NPs. Coverage has been determined by *SPIP* software. In this case no distinction between clusters needs to be considered.

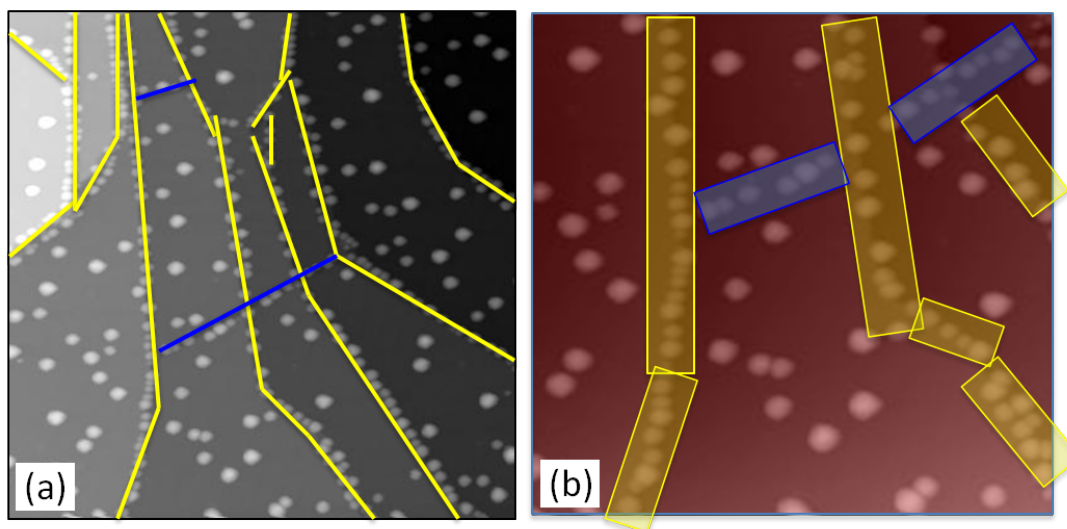


Figure 4.5: *STM images of 0.1 ML Ag/ZrO₂ (a) (200×200) nm² (0.5 V) and (b) zoom on the same image. Coloured lines and areas indicate the selected regions to determine cluster density.*

Apparent dimensions: height and diameter

When performing STM measurements it is fundamental to remind that this technique does not provide a photographic image of the system, but a convolution of morphology and local density of states at the surface. Additionally, imaging strongly depend on tip sharpness. For these reasons, morphological parameters like height and diameter should be treated as apparent values, not real one.

Cluster diameter, and all the in-plane lengths, are strongly affected by the shape of the tip, thus all measured lengths are overestimated. Anyway, it is possible to compare different NPs diameters in the same image, even reminding that this value is only an apparent diameter, not the real one and even compare diameters in different images if images quality is reasonably good and a satisfactory clean tip is obtained. If clusters are not spherical, cluster diameter stands for lateral dimensions, in the case of nanoparticles with simmetrical in-plane section. Diameter can be measured automatically by software analysis with SPIP, which gives an average value considering all the selected clusters. Diameter is calculated as the diameter of a circle having an area equivalent to the island's area A : $d = \sqrt{\frac{4}{\pi}A}$. Also for size determination, if different clusters types are present it is necessary to distinguish among them: in this case cluster diameter can be determined manually as the full width at medium height in a line profile drawn on the image; measurements have to be repeated and an average value has to be calculated to obtain sufficiently reliable data. An example of this procedure is reported in Fig.4.6, where a line profile has been drawn on two c-type clusters and diameter has been determined as the full width at medium height. This method is also preferrable when clusters are partially

superimposed or very close to each other. Additionally, in this case it is also possible to take into account the broadening of the shape due to tip effects, even if it gives a less statistical value.

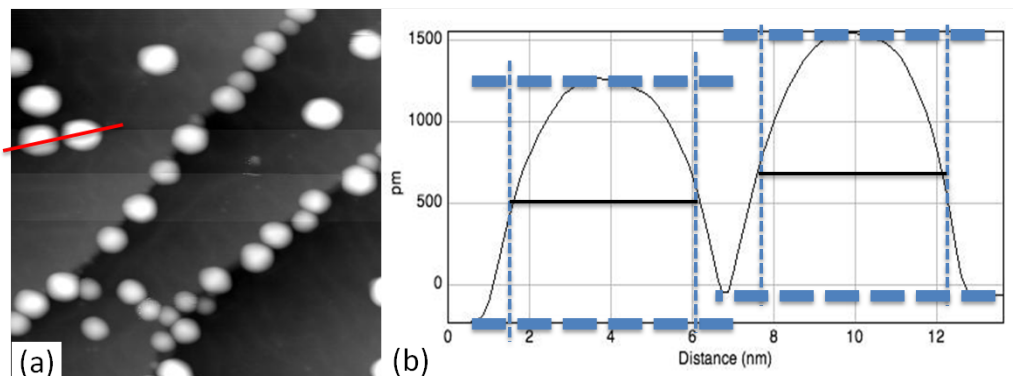


Figure 4.6: 0.1 ML Ag/ZrO_2 : (a) $(50 \times 50) \text{ nm}^2$ STM image (0.5 V) and (b) line profile on the red line drawn on image (a) with lines representing the determination of clusters diameter.

The determination of cluster height is even more intriguing, since it depends not only by tip effects, but also on the tunneling voltage. For measurements taken at voltage values within the oxide band gap, cluster height depends only weakly on voltage, instead, for higher bias voltage the tip probes unoccupied states of the oxide film, than the measured height is no longer representative of the real cluster height [146]. This effect has been reported for Pd clusters on a thin alumina film on NiAl(110) [145, 147, 148] and on Ni₃Al(111) [149]. So, only for measurements performed at a bias voltage inside the band gap, height variation is small and negligible (See Fig.4.7).

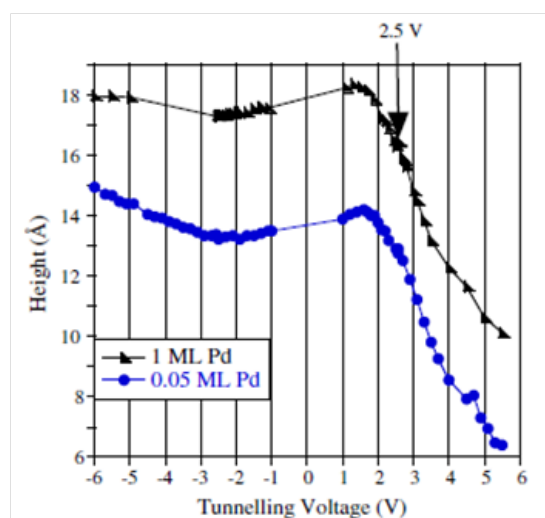


Figure 4.7: Apparent average height of Pd clusters on a thin alumina film on NiAl(110) as a function of the tunneling voltage. Data for 0.5 ML and 1 ML Pd show the same trend [145].

As for diameter, two approaches are available for height determination: an automatic and a manual method. In the first case, the software selects all the clusters and considers height distribution maximum as the average (most frequent) height, in the second case heights are measured as the difference between maximum and background level in line profile. The first method gives the average height as the most frequent value in height distribution only if the distribution is symmetric and centered around maximum, otherwise the distribution should be considered in a more detailed way. The second procedure includes less statistics, since only some clusters are measured, however it could be more reliable to obtain height because the software is not always precise to select cluster area and also it is not able to distinguish different clusters types. So, the second approach was used to determine cluster apparent height, the first mostly to get information about cluster orientation (see next section).

It has to be mentioned that the maximum height variation in the whole range considered by the previously mentioned studies [145, 149] is less than 1 nm and that in the range between -1 and +4 V (used in this work) the variation is about 6 Å. In particular, bias voltage ranges used are, respectively from 3 to 4 V, from 2 to 3 V and from -1 to 2 V for Ag/MgO, Ag/ZnO and Ag/ZrO₂ respectively, so variation should be less than 5 Å, which is very close to the experimental error introduced by the height determination method. Besides, for both MgO and ZrO₂, which are wide band gap oxide, these values are also inside the band gap. Thus, it is possible to hypothesize the absence of relevant variations of height due to bias voltage.

For Ag/ZrO₂ case, height variation with voltage has been checked: average height value was determined by line profile of chosen clusters taken in the same experimental conditions, except for bias voltage, which was changed between -1.5 and +2.5 V. In this voltage range a maximum variation of 4 Å was reported, confirming the hypothesis of negligible height variation.

Shape and crystal structure

From STM images it is possible to have a hint on the crystal orientation by upper terraces shape: for example, a threefold symmetry can be an evidence of growth exposing cubic (111) or hexagonal (0001) planes. Cluster in-plane shape is obviously affected by tip shape, thus the information about terraces shape and consequently orientation has to be compared and integrated with other data, such as height distribution: the difference in height between maxima of the distribution corresponds to the interlayer distance which identifies a series of planes. For Ag fcc crystal structure (Fig.4.8) with lattice parameter $a = 4.09$ Å, interlayer distances can be obtained from: $d_{hkl} = \frac{a}{\sqrt{h^2+k^2+l^2}}$, which leads to: $d_{100} = a = 4.09$ Å, $d_{110} = \frac{a}{\sqrt{2}} = 2.89$ Å and $d_{111} = \frac{a}{\sqrt{3}} = 2.36$ Å.

An example of height distribution obtained with SPIP software is shown in Fig.4.8(d).

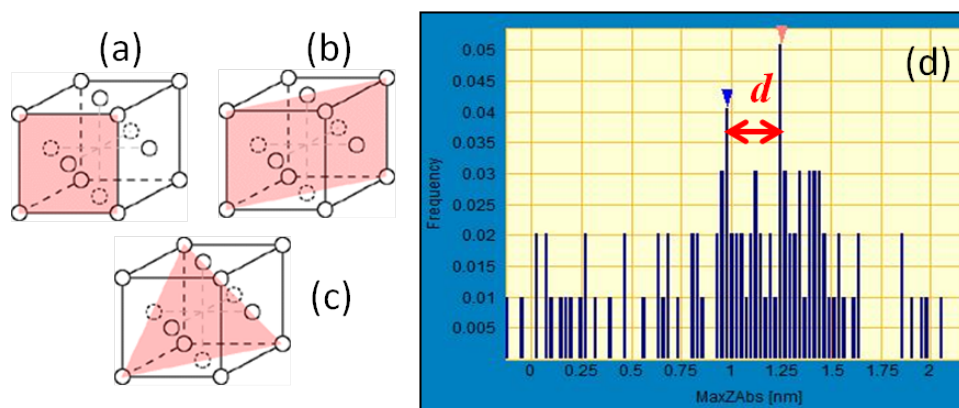


Figure 4.8: *Schematic representation of Ag cubic planes (a) fcc(100), (b) fcc(110) and (c) fcc(111). (d) Example of height distribution: blue and red arrows indicate maximum frequency values, the difference in height between the two values corresponds to an interlayer distance of 2.7 Å.*

Being a statistical measurement, the information about interlayer distance does not distinguish between different cluster types, but can anyway be compared with cluster upper terraces shape to hypothesize the orientation. In the case of Ag/ZrO₂, interlayer distance for all clusters in different preparation and treatment conditions is about 2.7 Å, which is compatible with a growth on fcc(111) or fcc(110) plane. Threefold NPs symmetry shapes, displayed in Fig.4.9, supports the first hypothesis. It has to be noticed that interlayer distances between different crystal planes differs one from another by few Å or fraction of Å, thus, when good resolution is obtained, information about island upper terraces shape can be considered sufficiently reliable.

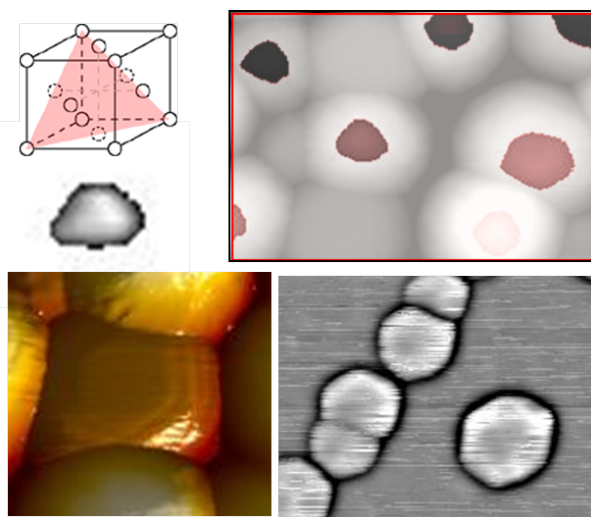


Figure 4.9: *Schematic representation of Ag(111) cubic plane and STM images of Ag/ZrO₂ elaborated to highlight upper terraces shape.*

Contact angle

Cluster contact angles accounts for specific cluster shape, which determines cluster properties, such as plasmonic response. In case that clusters show a nearly uniform shape, they can be approximately considered as truncated spheres, with volume:

$$V = \frac{\pi}{3}h^2(3R - h) \quad (4.1)$$

where R and h are radius and height, respectively.

Thus, from geometric parameters determined by STM images analysis it is possible to calculate contact angle α_c , defined as:

$$\cos\alpha_c = 1 - \frac{h}{R} = 1 - \frac{3\pi h^3}{3V + \pi h^3} \quad (4.2)$$

Height h is directly obtained with the previously described methods. The average volume V is calculated from the amount of metal deposited, in particular from metal coverage θ (in ML), atom density in a metal monolayer n_A (atoms/m²), atom density of the metal bulk N_V (atoms/m³) and cluster density n_C (clusters/m²):

$$V = \frac{\theta n_A}{n_C N_V} \quad (4.3)$$

N_V is specific of the chosen metal and, for Ag case, is obtained by:

$$N_V = \rho \frac{N_{Av}}{m_{mol}} = 5.86 \times 10^{28} \text{ at/m}^3 \quad (4.4)$$

where ρ is density and m_{mol} is molar mass of the material.

Cluster density is determined by STM images; θ and n_A depend on the crystal structure of the clusters, in particular on the exposed plane, so they should be determined after identification of the orientation of the nanoparticles. For Ag: $\theta_{100} = \text{thickness}(\text{\AA})/2.05 \text{ \AA}$, $\theta_{111} = \text{thickness}(\text{\AA})/2.36 \text{ \AA}$, $n_{A(100)} = 1.2 \times 10^{19} \text{ at/m}^2$, $n_{A(111)} = 1.4 \times 10^{19} \text{ at/m}^2$.

An analogous alternative parameter which defines nanoparticle shape is truncation parameter t_r , which is defined as:

$$t_r = \frac{h - R}{R} \quad (4.5)$$

Spheres are distinguished depending on contact angle or truncation parameter: if $t_r > 0$ ($\alpha_c > 90^\circ$) the sphere is truncated, if $t_r < 0$ ($\alpha_c < 90^\circ$) the sphere is called a cap (see Fig.4.10) More generally, when the out-of-plane z axis differs from the others, so if the cluster shows spheroidal shape with $R = a$ major semiaxis and c minor semiaxis volume is defined as:

$$V = \frac{\pi ab}{3c^2} h^2 (3c - h) \quad (4.6)$$

And, thus:

$$c = \frac{3 + \sqrt{9 - \frac{12V}{\pi R^2 h}}}{\frac{6V}{\pi R^2 h^2}} \quad (4.7)$$

The contact angle can be calculated by considering the angular coefficient m of the tangent to the spheroid at the point P , with coordinates (x_0, y_0) , shown in Fig.4.10(c), defined as:

$$m = -\frac{c^2}{R^2} \frac{x_0}{y_0} \quad (4.8)$$

with

$$x_0 = R \sqrt{1 - \frac{(h-c)^2}{c^2}} \quad (4.9)$$

$$y_0 = -(h-c) \quad (4.10)$$

which leads to:

$$m = \frac{c^2}{a(h-c)} \sqrt{1 - \frac{(h-c)^2}{c^2}} = \text{tg}(\pi - \alpha_c) = -\text{tg}\alpha_c \quad (4.11)$$

Truncation parameter is defined, in this cases as:

$$t_r = \frac{h-c}{c} \quad (4.12)$$

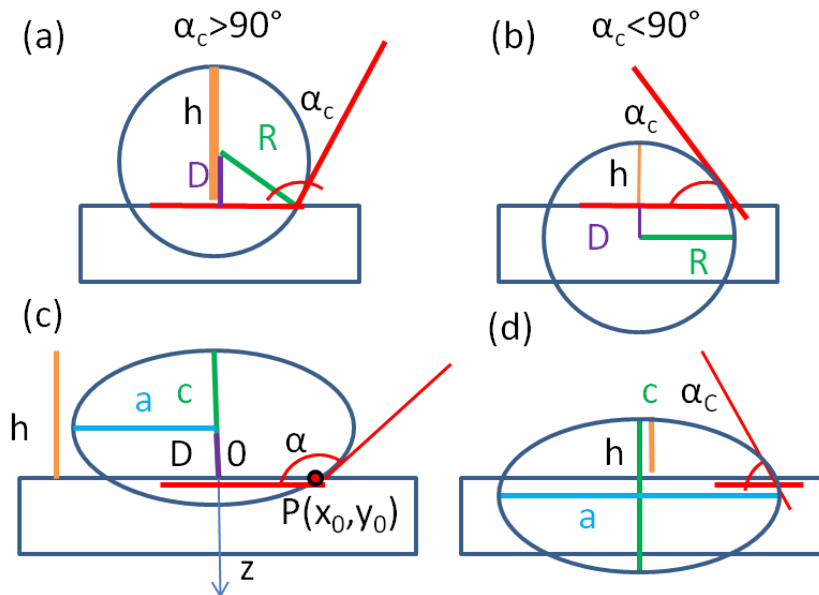


Figure 4.10: Schematic representation of particle shapes: (a) truncated sphere, (b) cap sphere, (c) truncated spheroid and (d) cap spheroid. Significant parameters R , h and α_c are reported.

Work of adhesion

Work of adhesion W_{ad} is the energy per unit area needed to remove clusters from the oxide surface, assuming no plastic or diffusional modifications. In case of a supported spherical metal nanoparticle in thermodynamic equilibrium with an oxide substrate, work of adhesion is obtained by the sum of surface energies of the metal (γ_{met}) and of the oxide (γ_{ox}), subtracting the surface energy of the metal-oxide interface (γ_{ox-met}):

$$W_{ad} = \gamma_{met} + \gamma_{ox} - \gamma_{ox-met} \quad (4.13)$$

Surface energies are related to the contact angle by the relation:

$$\gamma_{ox-met} = \gamma_{ox} - \gamma_{met} \cos \alpha_c \quad (4.14)$$

Thus, combining eq.4.13 and 4.14:

$$W_{ad} = \gamma_{met}(1 + \cos \alpha_c) \quad (4.15)$$

Since real shape and orientation of clusters are not known, an approximation for γ_{met} should be hypothesized. If the shape of the cluster follows Wulff construction [150] and crystal structure is a face centered cubic, which is the most stable for Ag, surface energy can be calculated assuming that surface energy per atoms is proportional to the number of broken bonds. Considering this simple bond-breaking model, cluster has eight equal regular (111) facets and six equal square (100) facets, but no other facets like (110). The total area of the (111) facets is $2\sqrt{3}$ times larger than the one of the (100) facets, whose area thus much smaller and leads only to a 3% increase of the average surface energy. Additionally, a Wulff shaped polyhedron has larger surface area than the sphere with same volume, and thus a larger surface energy. The surface of the Wulff polyhedron is 10% larger, and thus the surface has an overall 13% larger energy than a sphere of equal volume. Since eq.4.13 and 4.14 are obtained at a fixed volume for a spherical particle, a correction of $\gamma_{met} = 1.13 \gamma_{met(111)}$ gives a proper approximation. For silver $\gamma_{met(111)} = 1.2 \text{ J/m}^2$ [151] and $\gamma_{met} = 1.36 \text{ J/m}^2$.

It has to be noticed that this method is applicable only when clusters are indistinguishable, since it involves metal coverage in ML, which is an overall quantity.

4.1.3 Morphology and structure

Growth and self-assembly of Ag nanoparticles on a ZrO_2 trilayer obtained by oxidation of $\text{Pt}_3\text{Zr}(0001)$ have been studied. Ag clusters have been deposited by MBE and the dependence of morphological and structural properties on preparation protocols have been investigated by STM. The evolution of the morphology of Ag nanoparticles with post-deposition treatments has also been studied.

For low amounts of deposited material (0.3 \AA nominal thickness) grown at RT, three types of Ag clusters can be distinguished depending on the preferential sites for adsorption [Fig.4.11(a)]. Clusters which nucleate on terraces steps and domain boundaries are smaller than the ones which grow in the central part of the terraces and their density is higher. Clusters at domain boundaries can be distinguished from clusters at plain terraces by studying the rotational orientation of the oxide film. With a higher amount of material, 6 \AA , surface coverage is higher and clusters appear bigger, without any distinction of preferential sites [Fig.4.11(b)]. Most of the clusters show a growth on (111) fcc plane, as highlighted by upper terraces rounded triangular shape [Fig.4.11(c-d)] and difference between maxima in height distribution [Fig.4.8(d)].

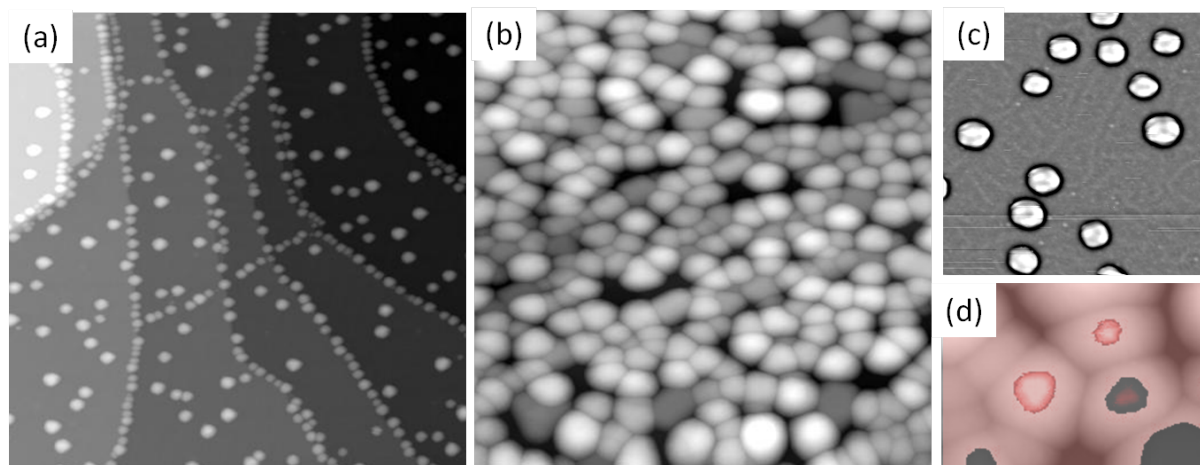


Figure 4.11: *STM images of Ag/ZrO₂: (a) 0.3 Å, (200×200) nm² (0.5 V); (b) 6 Å, (200×200) nm² (-1 V); (c) (50×50) nm² image for 0.3 Å with contrast setting highlighting cluster shape and showing the reconstructed oxide film below (1 V); (d) detail of 6 Å image showing upper terraces shape and the presence of 120° and threefold symmetry.*

The morphology of low coverage RT deposited clusters is not significantly affected by staying in the UHV chamber for two days or by 473 K annealing (not shown here). After 673 K annealing cluster density significantly decreases [Fig.4.12(a)]. Since the apparent height of the clusters in the central part of the terraces increases, this can be partly due to diffusion and aggregation of clusters, as already reported for silver deposited on other catalytic oxides, like CeO_2 [152]. In the present case, however, the increase in cluster dimensions is

too low to account for all the material deposited, suggesting desorption of material from the surface or diffusion through the oxide to subsurface sites. For higher coverage of Ag NPs, a change in morphology is reported after annealing at 473 K [Fig.4.12(b)]: bigger clusters and large areas appear, with average height and diameter (as determined by line profiles) of 4-5 nm and 10-15 nm, respectively. While the presence of some bigger clusters [(25×10) nm²] is clearly shown in the images and can reasonably result from the aggregation of two or more of the clusters previously present on the surface, the nature of the wide areas can be associated either to very big silver aggregations or to ZrO₂ uncovered surface areas. The height of these areas is 2-3 nm, which is much higher than terraces step edges, making the hypothesis of very big clusters aggregations more favorable.

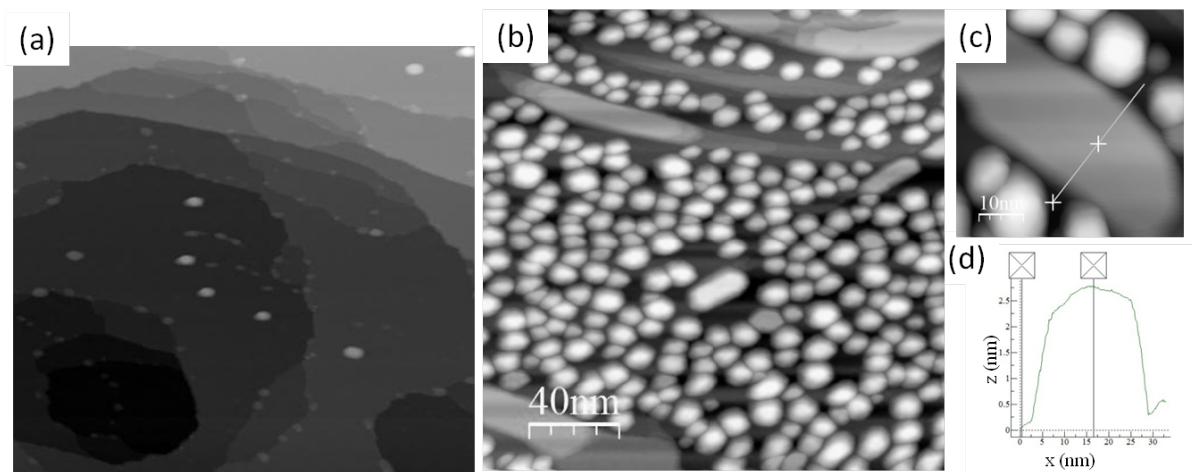


Figure 4.12: *STM images of Ag/ZrO₂: (a) 0.3 Å after annealing at 673 K, (200×200) nm² (-1 V); (b) 6 Å after annealing at 473 K, (200×200) nm² (-1 V); (c) (50×50) nm² image for 6 Å after annealing at 473 K and (d) corresponding line profile showing a 3 nm height (-1 V).*

Quantitative results for all the preparations are reported in Table 4.1. Both density for single cluster type and considering all NPs on the surface are reported. For 0.3 Å after annealing at 673 K the low cluster number does not allow a significant determination of cluster density for single cluster type, while at 6 Å silver NPs were indistinguishable. Errors on cluster diameter and height are estimated to at least 0.5 nm. Average aspect ratios (not reported here) are between 2 and 3, corresponding to flat clusters.

For clusters which show uniform shape without any distinction of cluster type, it is possible to calculate contact angle and work of adhesion, hypothesizing a spherical shape, from eqs.4.2 and 4.15. For Ag/ZrO₂ this is verified for high coverage NPs. Contact angles obtained are, respectively: 143° and 120° for as grown and annealed samples, corresponding to truncated spheres. The calculated works of adhesion are: $W_{ad} = 0.27$ and 0.68 J/m², thus the effect of temperature is to increase adhesion of clusters on the surface creating larger NPs.

| t_{nom} (Å) | | | c (%) | n_{tot} (m^{-2}) | n_b (m^{-2}) | n_c (m^{-2}) | n_d (m^{-2}) |
|------------------|------------|---------------|---------------|---------------------------|-----------------------|-----------------------|-----------------------|
| 0.3 | as grown | | 15 | 1.0×10^{16} | 7.4×10^{16} | 0.3×10^{16} | 5.5×10^{16} |
| 0.3 | 2 days UHV | | 10 | 0.9×10^{16} | 6.5×10^{16} | 0.2×10^{16} | 8.4×10^{16} |
| 0.3 | ann.473 K | | 10 | 0.5×10^{16} | 4.1×10^{16} | 0.3×10^{16} | 2.8×10^{16} |
| 0.3 | ann.673 K | | 2.5 | 0.2×10^{16} | - | - | - |
| 6 | as grown | | 95 | 0.6×10^{16} | - | - | - |
| 6 | ann.473 K | | 95 | 0.4×10^{16} | - | - | - |
| t_{nom} (Å) | | d_b (nm) | d_c (nm) | d_d (nm) | h_b (nm) | h_c (nm) | h_d (nm) |
| 0.3 | as grown | 3 | 4 | 3 | 1.3 | 1.3 | 1.3 |
| 0.3 | 2 days UHV | 3 | 4 | 3 | 1.3 | 2 | 1.3 |
| 0.3 | ann.473 K | 4 | 4 | 4 | 1.3 | 2 | 1.3 |
| 0.3 | ann.673 K | 4 | 5 | 4 | 0.5 | 2 | 0.5 |
| 6 | as grown | 15 | 15 | 15 | 5 | 5 | 5 |
| 6 | ann.473 K | 15 | 15 | 15 | 5 | 5 | 5 |

Table 4.1: Morphological parameters of Ag/ZrO₂ as determined by STM images analysis: coverage (c), total cluster density (n_{tot}). Cluster density (n), diameter (d) and height (h) are reported for each single cluster type (b , c and d).

From contact angle value, geometrical radius of the spherical particle can be calculated by reversing eq.4.2:

$$R = \frac{h}{1 - \cos\alpha_c} \quad (4.16)$$

Values obtained are 2.8 Å and 3.2 Å, respectively for as grown and annealed samples (Fig.4.13), corresponding to aspect ratios d_{calc}/h_{STM} equal to 1.1 and 1.3, thus very close to the one of a perfect sphere ($d/h = 1$). Calculated radius values of 2.8 Å and 3.2 Å are largely smaller than the ones measured by STM (7.5 Å). While it is expectable that STM measured lengths are overestimated, the high discrepancy between measured and calculated radius can be related both on the experimental side to tip effects affecting diameter determination and on calculation side to errors in the determination of cluster density and height, but also to the hypothesized spherical cluster shape. Besides, the estimation of NPs volume includes the tacit hypothesis that all the evaporated material sticks on the surface, by considering the number of deposited ML.

While from STM images NPs show a simmetrical in-plane section, which means equal in-plane axis, whether the third axis is equal or not to the other ones is not trivial to be determined. If clusters are not spherical eqs.4.6-4.12 should be considered. From purely morphological parameters it is not possible to determine whether cluster shape is spherical or spheroidal and results have to be integrated with different measurements.

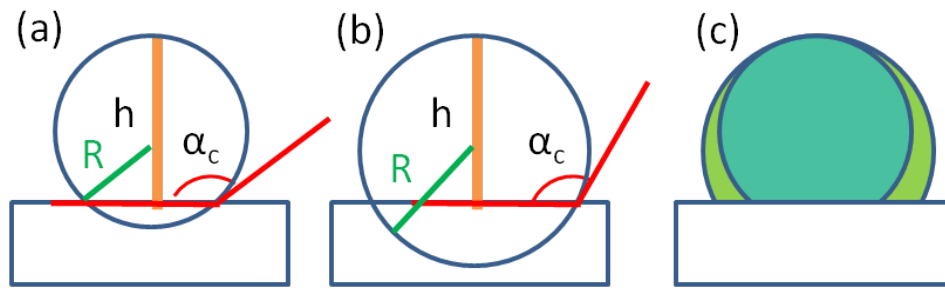


Figure 4.13: *Schematic representation of 6 Å nominal thickness Ag NPs deposited on ZrO₂ (a) as grown and (b) after annealing at 473 K. NPs are represented in a scale drawing, with height as determined by STM and contact angle and radius calculated by a spherical cluster model. Image (c) represents the modification of cluster shape induced by temperature: NPs become slightly bigger without increasing in height.*

Conclusions

Ag NPs have been deposited on ZrO₂ thin film and morphological and structural properties have been investigated by means of STM technique. For low coverage (0.3 Å) NPs morphology strongly depends on the preferential site for adsorption: bigger clusters are formed on terraces central part, while on terraces borders and domain boundaries island are smaller and present a higher density. Increasing the amount of deposited material to 6 Å almost complete coverage is reached and an uniform and homogenous distribution of clusters is observable. All clusters grow exposing fcc(111) surface, as possibly favoured by the presence of an hexagonal substrate. Particle geometry for high coverage NPs film has been hypothesized by morphological parameters: NPs can be modeled as truncated spheres, close to perfect spherical shaped clusters. Morphology is unaffected by staying in UHV chamber up to two days, while annealing induces clusters desorption at low coverage and aggregation with increase in adhesion for higher amount of deposited material.

A powerful method to analyze STM images has been developed by using Ag/ZrO₂ as a case study. Morphological parameters as cluster density, height and diameter have been determined by using the most suitable procedure for each quantity and evaluating the involved errors. Particle crystal structure and geometry have also been extrapolated by combining different experimental data with a model to mimic NP shape. This procedure provides a reliable and quite accurate way to investigate particle morphological and structural properties, fundamental to understand growth mechanism and also optoelectronic properties.

4.2 Ag/MgO

The Ag/MgO(001) interface has been chosen as a prototypical metal-oxide system in different works for many reasons: the noble metal nature of silver unfavours chemical reactions at the interface, while the cube-on-cube epitaxy, the small (3%) lattice mismatch and low contribution of epitaxial strains allow the growth of good quality structures. Ag NPs have been deposited on both MgO bulk crystals [23, 24, 130–135] and MgO thin films [153].

Silver NPs, with thicknesses ranging from 2 Å to 45 Å have been grown on a MgO(001) bulk crystal both at room temperature and 640 K and an *in situ* and in real time characterization by coupled surface differential reflectivity spectroscopy (SDRS) and grazing incidence small angle x-ray scattering has been performed by Lazzari et al. [134]. In this study the evolution of particles growth has been determined by the optical and structural properties. Ag NPs grow as truncated spheres, whose diameter, height and distance increase with increasing silver amount, while aspect ratio (diameter/height) does not show a monotonic trend. SDR results are displayed in Fig.4.14. Parallel mode (2.5–3.0 eV) shows a strong redshift with increasing thickness, as expected for bigger particle size [25]. On the contrary, perpendicular mode (3.8 eV) is quite insensitive to particle size.

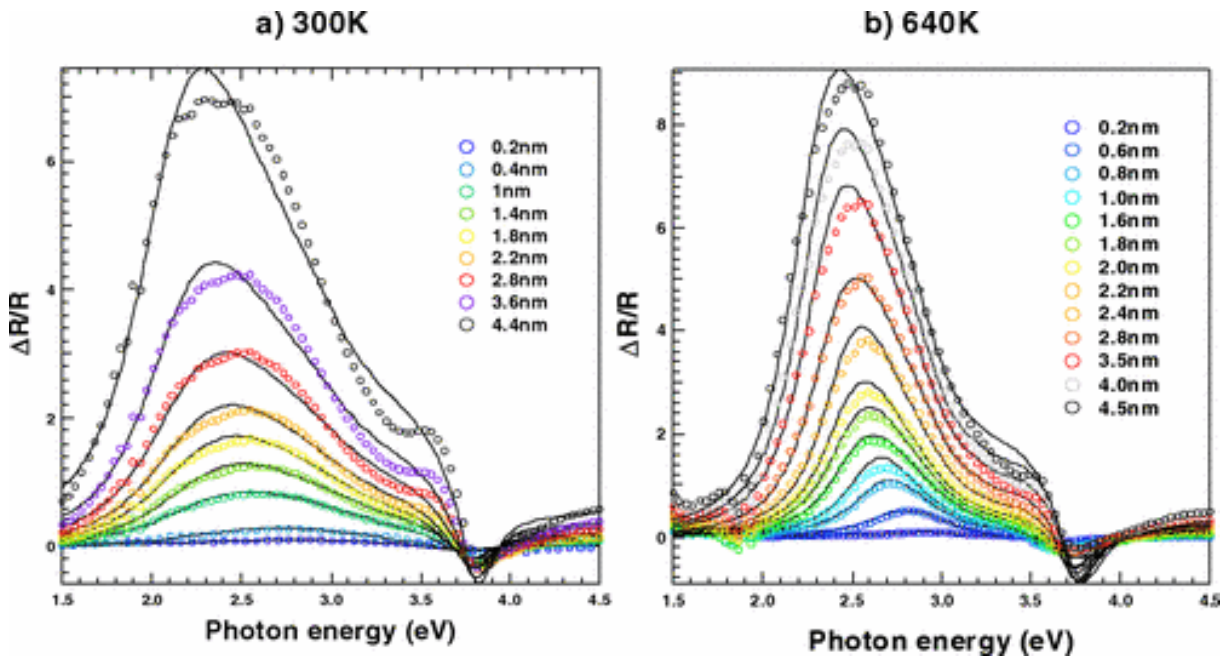


Figure 4.14: SDRS optical spectra recorded *in situ* during the growth of the Ag/MgO(001) film at (a) 300 and (b) 640 K. Deposited thicknesses are given. Open circles: experiment, line: simulation [134].

In another work by Lazzari et al. plasmonic properties of Ag/MgO(001) system have been probed by EELS simulations and compared with the Ag/Si(111) system [24]. The shape-induced plasmon splitting of the absorption modes strongly depends on the dielectric constant of the materials involved. For parallel (perpendicular) mode, depolarization field created by image dipole reduces (increases) the restoring force acting on the electron cloud, which results in a red shift (blue shift) of the mode. Silicon has a higher dielectric constant value ($\epsilon \sim 10$), with respect to MgO ($\epsilon \sim 3$), so this effect is stronger.

EELS cross section simulations displayed in Fig.4.15 show the dependence of EELS peaks on aspect ratio for Ag NPs on MgO: for aspect ratio close to 1 the parallel and perpendicular modes are partially superimposed and result in a broad double peak, when aspect ratio increases the difference in peaks energy increases due to a blueshift of perpendicular mode and a redshift of the parallel one. The shape effect is more relevant for parallel mode than for perpendicular one. The real case for NPs on MgO is close to full spherical shape, while with Si substrate Ag forms flat clusters with high aspect ratio: the separation of peaks is enhanced by shape effects for the low gap silicon substrate, since adhesion energy increases when the gap narrows [26].

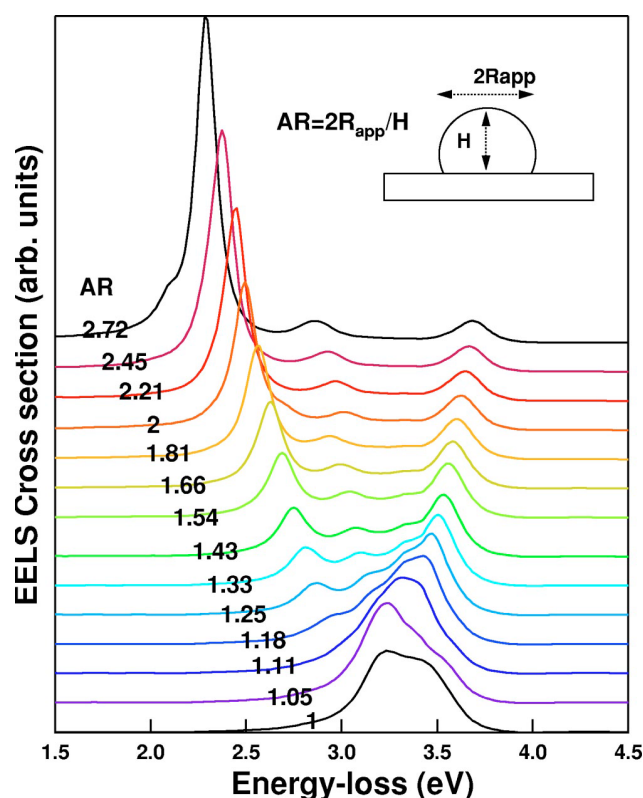


Figure 4.15: Model spectra calculated for truncated spheres of silver supported on MgO to show the influence of the particle aspect ratio on the EELS cross section. Due to the poor wetting of MgO by silver, the real case is close to full sphere. For the sake of clarity, the spectra have been shifted with respect of each other and normalized by the mean film thickness [24].

The study of Ag NPs on a bulk crystal is a simple way to analyze the properties of metal-oxide systems with very good reproducibility, however, the oxide substrate does not allow the use of electronic spectroscopies and imaging techniques. To overcome this limitation, Ag clusters have been deposited on MgO thin films grown on a Mo(001) substrate. The MgO/Mo system has been largely studied [153–157] and a good quality oxide film can be obtained with very high reproducibility. Additionally, Mo shows negligible contribution to the plasmonic properties of the system, thus the Ag/MgO/Mo is an ideal candidate for this study. Films can be employed also to control self assembly and to study additional contributions like interfacial interactions and charge transfer effects.

Morphology of MgO films strongly depends on deposited thickness: up to 7 ML a square pattern due to induced strain by mismatch has been observed [157], which disappears at 15 ML thickness, with the formation of rectangular terraces; for higher thickness the film is strongly flattened and system roughness significantly reduced. 10 ML thickness has been chosen by Benedetti et al. [157] to grow Ag NPs, because the resulting film is quasi-relaxed, with a sufficiently flat surface and a still visible square pattern.

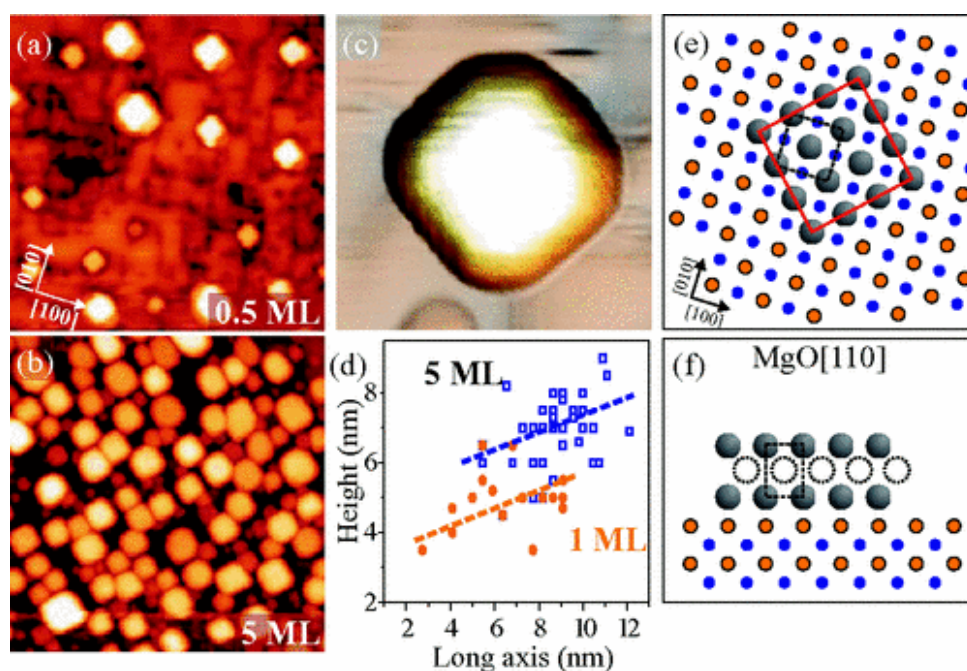


Figure 4.16: (a), (b) $(100 \times 100) \text{ nm}^2$ STM images of 10 ML MgO/Mo(001) for two different exposures of Ag: 0.5 ML (approximately 1 \AA) and 5 ML (4.5 V). For image (a), the sample has been slightly annealed to 550 K after Ag deposition. (c) $(10 \times 10) \text{ nm}^2$ STM image of a characteristic Ag particle. (d) Statistical evaluation of the geometry of Ag particles for two metal exposures. Structure model of the fcc(001) plane of Ag on the MgO surface: (e) top and (f) side view along the indicated crystallographic direction. The fcc Ag unit cell is marked by dashed lines; the particle edges are depicted by a red, solid rectangle. Filled and broken circles in (f) indicate atoms in the plane of view and the next plane, respectively [153].

Morphology and crystal structure of Ag on 10 ML MgO/Mo have been studied: STM images show the nucleation of silver on the MgO dislocation network with a large tendency to 3D growth and a perfect lattice match with the MgO support (see Fig.4.16). When 1 ML (corresponding to about 2 Å) equivalent thickness of Ag is deposited, NPs show the same lattice parameters of the bulk material, while between 1 and 4 ML an intermediate value between Ag and MgO lattice parameters is measured, critical dimension is reached between 4 and 6 ML and a continuous film is formed over 30 ML [158].

Ag/MgO/Mo represents a reference model system, whose study is propedeutic to the comprehension of less understood and more complex systems, thus it has been chosen in this work as a prototypical case study for the analysis of plasmonic properties and how they relate to morphology of nanoparticles.

4.2.1 Electron-Energy Loss Spectroscopy

Electron energy loss spectroscopy is one of the most used technique to investigate plasmonic properties of a system. As mentioned in Sec.1.2, the optical extinction cross section θ_{ext} (see eq.1.2) for metal particles in the quasi-static regime is related to the polarizability and depends on the electron energy losses, thus EELS is a suitable technique to study plasmon resonances. The existence of LSPRs was actually verified for the first time in 1959 with this technique for the metal/vacuum interface of Al and Mg by Powell and Swan [159].

The study of surface electronic excitations is based either on optical methods or on the inelastic scattering of electrons [34]. When applying optical methods, a coupling between the surface plasmon field and the electromagnetic field is necessary, which is generated either by a grating or by the attenuated total reflection method. These methods are, however, limited to quite large wavelengths at which retardation effects are important and give rise to so-called surface plasmon-polaritons. Larger wavevectors can only be achieved by inelastic scattering of electrons.

In inelastic scattering processes from crystalline structures, energy and wavevector parallel to the surface are conserved:

$$E' - E = \hbar\omega \quad (4.17)$$

$$\vec{k}'_p - \vec{k}_p = \vec{q}_p - \vec{G}_p \quad (4.18)$$

where \vec{G}_p is a wavevector of the reciprocal lattice.

Energy $\hbar\omega$ and wavevector \vec{q}_p can be transferred to collective surface excitations, like phonons and plasmons, to single particle like conduction band electrons (intraband scattering) or to electrons which are excited from an occupied electron band to an empty one (interband scattering).

In Fig.4.17 the geometry of a surface scattering experiment is shown. \vec{k} is incident particles wavevector, the scattering in the specular direction with $|\vec{k}_s| = |k|$ represents the elastic process, while the inelastic ones usually involve scattering out of the specular direction and are described by the angles ψ and ϕ . Scattered wavevector \vec{k}' differs from specular wavevector \vec{k}_s by the transferred wavevector \vec{q} .

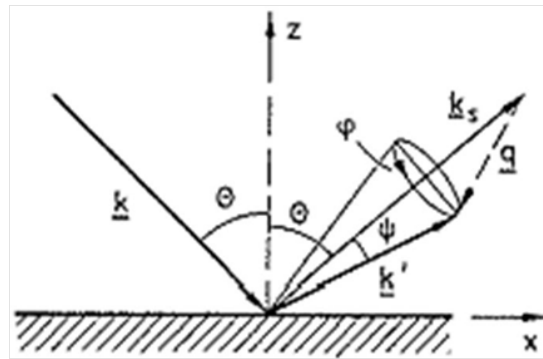


Figure 4.17: *Inelastic scattering representation, with wavevector indication [160].*

Among the particles which can be used for surface inelastic scattering experiments, electrons with low energy are the most relevant, not only because they can be easily produced and analyzed, but also because the penetration into crystal is limited and therefore they are ideally suited for surface investigation. Additionally, from a theoretical point of view, a simple mathematic approach is available to describe inelastic scattering for low energy electrons. Two models are applicable, which differ from the scattering mechanism involved: dipole and impact scattering [Fig.4.18(a)].

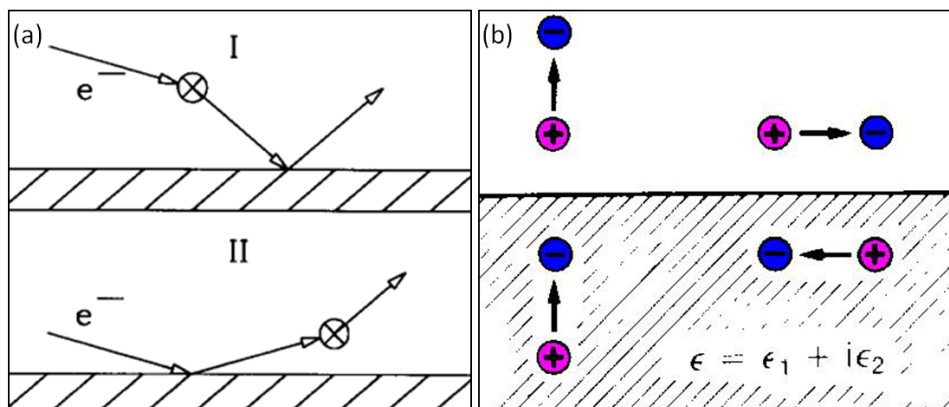


Figure 4.18: (a) *Schematic representation of the possible events in dipole scattering: in case I the electron-surface interaction and the consequent energy loss occurs before the contact with the surface, in case II the process takes place after reflection [34].* (b) *Schematic representation of the normal dipole selection rule.*

Dipole scattering, which dominates at low energy, is caused by the Coulomb interaction of the electrons with a long-range potential, constituted by oscillating dipole fields, which can originate from collective oscillations, such as surface lattice vibrations (phonons) and surface plasmons. The interaction can occur before or after the impact with the surface. Incident electrons are specularly scattered with an energy loss characteristic of the energy given to the vibrational mode. Thus, the resulting information is analogue to the one obtained from an Infrared spectrum. Besides, the selection rule of normal dipole is applicable [Fig.4.18(b)]: the dipole scattering is insensitive to dipole oscillating parallel to the surface and the field interacts only with dipoles normal to the surface when an image dipole is present. Impact scattering is, on the contrary, a short range process, which involves the virtual excitation of an electronic state of a surface atom: the inelastically scattered electron briefly occupies an excited state of this atom and then leaves it with energy which differs from the original one by a vibrational quantum (phonon, plasmon or adsorbed material vibration). Once the electrons loses energy it is deviated from the reflection angle. By measuring deflection angle, it is possible to obtain dispersion relation of the electrons excitation [34].

In EELS experiments [Fig.4.19(a)], which are performed in UHV, the incident electron beam is directed to the surface and the energetic spectrum (and possibly the angular distribution) of the backscattered electrons is measured.

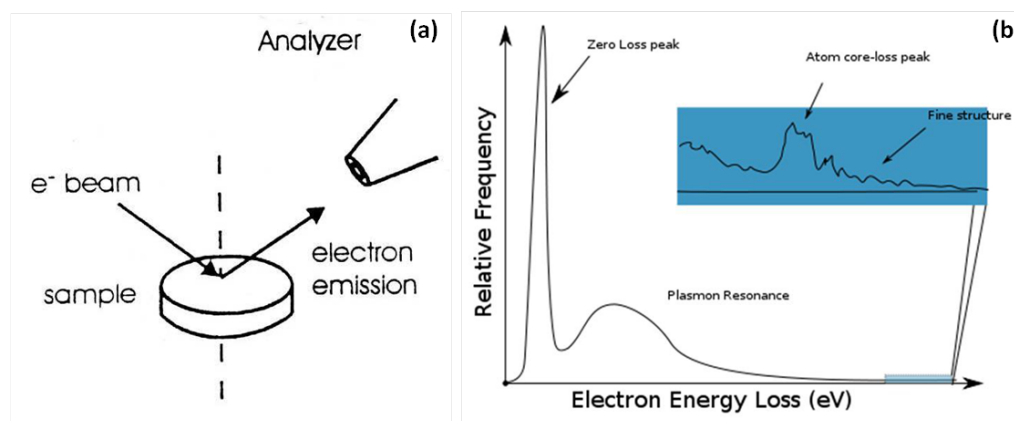


Figure 4.19: (a) Schematic of an experimental apparatus for EELS measurements. (b) Idealized schematic of an EELS spectrum, indicating zero-loss peak, plasmon resonance, and core-loss electron peak.

Electrons are emitted by an electronic gun, constituted by a W filament which is heated to produce electrons by thermoionic effect. Electrons are then accelerated by a potential difference and directed to the sample. Desired electrons kinetic energy is in the range of 1-1000 eV: in this condition, electrons penetrate only the first 3-4 layers of the crystal, so

that backscattered electrons only transfer information from the surface. The backscattered beam is collected by an analyzer which determines the energetic distribution. In the hemispherical analyzer, electrons coming from the sample experience a retarding potential and go through a lenses system to reach analysis system, which is formed by two concentric semispheres, one set to positive potential with respect to pass energy, the other set to negative one: only electrons with energy close to pass energy value reach the exit gap. The exit signal is amplified by electrons multipliers. Gap apertures and pass energy determine the analyzed area, the energy resolution and the angular acceptance of the electrons. An example of the typical EELS spectrum is displayed in Fig.4.19(b). At high energy the transmitted beam is formed by inelastically scattered electrons, whose energy differs from the primary beam by the energy corresponding to the characteristic absorption frequency of the solid in study; in the low energy part of the spectrum structures corresponding to phonons and bulk and surface plasmons are detected.

4.2.2 Growth of Ag NP on MgO

Ag NPs have been deposited on 10 ML MgO grown on a Mo(001) substrate. Mo single crystal has been prepared by sputtering [$E = 0.6 - 1$ KeV, $p(\text{Ar}^+) = 10^{-6}$ mbar] and annealing (1200 K) cycles, verifying the cleanness of the surface by AES spectroscopy, the crystal quality by LEED and the morphology, characterized by large terraces, by STM [Fig.4.20(a)]. A 10 ML (equivalent to about 20 Å) MgO thin film has been grown on Mo substrate by reactive deposition of Mg in oxygen atmosphere [$p(\text{O}_2) = 5 \times 10^{-8}$ mbar] at room temperature and subsequently annealed to 1100 K. MgO/Mo STM image reported in Fig.4.20(b) shows the presence of large terraces (20-50 nm wide) and of the dislocation lines already reported by Benedetti et al. [154]. The modulation arising from the dislocation lattice at the MgO-Mo interface with periodicity 5.5 nm is clearly observable.

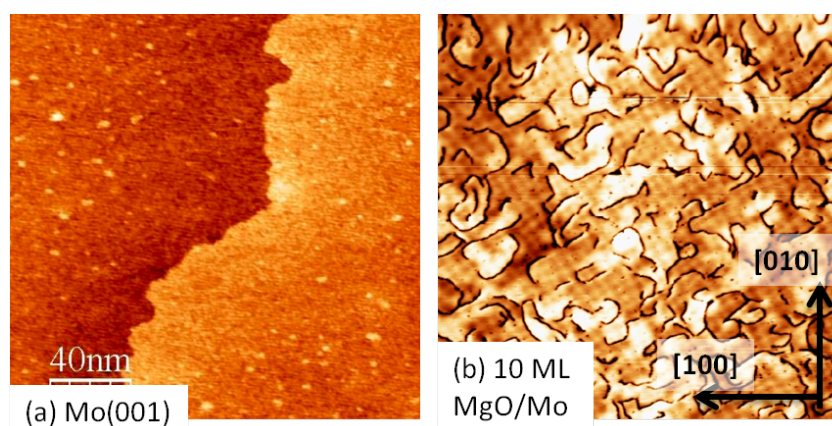


Figure 4.20: (200×200) nm² STM images: (a) clean Mo(001) surface. (3.9 V, 0.05 nA). (b) 10 ML MgO/Mo (0.5 V, 0.3 nA).

Silver has been grown by MBE at room temperature, with deposition rate of 8×10^{-3} Å/s and nominal thicknesses in the 0.1 Å - 2 Å range, to study the initial stages of growth mechanism. The effect of temperature, both during deposition and with subsequent treatments has been studied for 0.5 Å Ag/MgO. Morphological properties have been analyzed by STM technique, with the procedure described in Sec.4.1.2, and related to plasmonic properties determined by EELS. STM images have been acquired by an *in situ* UHV RT Omicron STM, working in constant current mode, with the W tip kept grounded and a positive bias voltage applied to the sample. EELS measurements have been performed in specular geometry ($\theta = 32^\circ$) with primary beam energy of 100 eV. The results of simulations with *GranFilm* software, based on both STM and EELS data, have allowed to obtain a more complete picture of the growth of silver clusters and to relate morphological and optical properties.

Morphology

STM images of Ag NPs deposited at RT with increasing thickness are displayed in Fig.4.21.

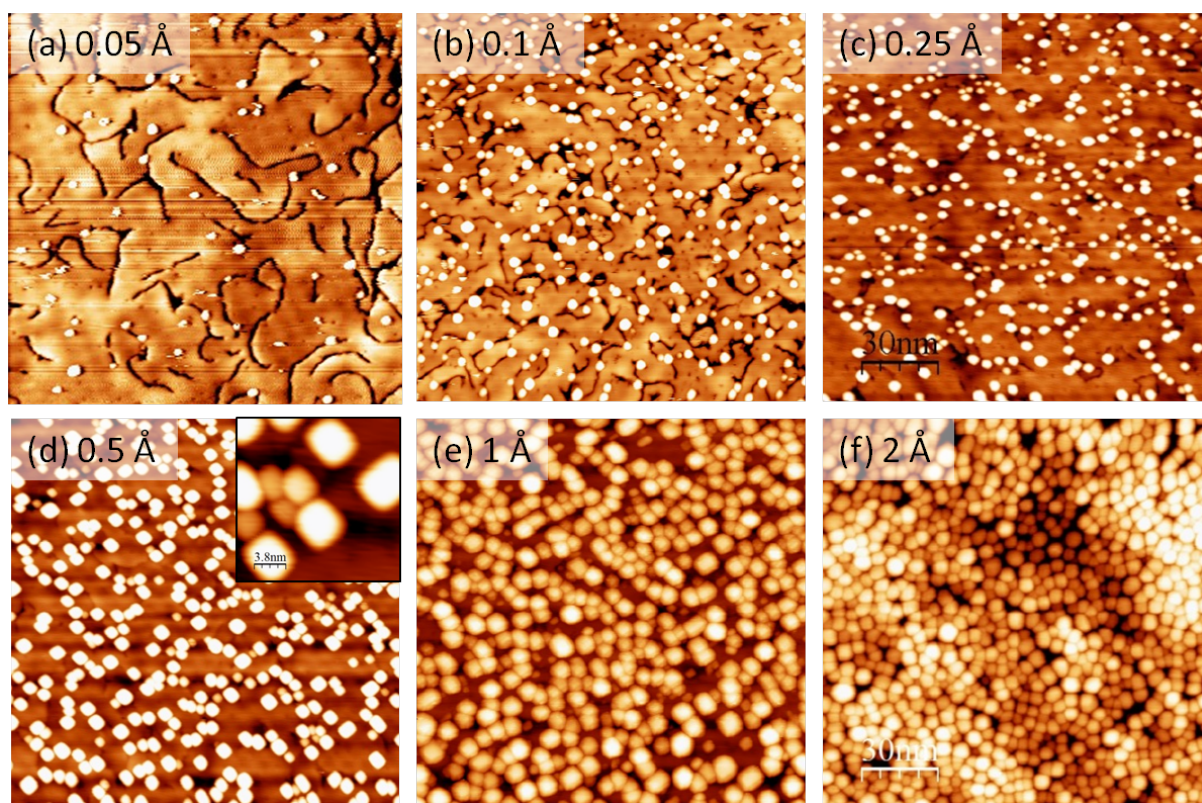


Figure 4.21: (150×150) nm² Ag/MgO/Mo STM images: (a) 0.05 Å (3.7 V, 0.04 nA); (b) 0.1 Å (3.5 V, 0.03 nA); (c) 0.25 Å (3.5 V, 0.05 nA); (d) 0.5 Å (3.6 V, 0.07 nA), (19×19) nm² inset shows square cluster shape; (e) 1 Å (3.7 V, 0.06 nA); (f) 2 Å (2.0 V, 0.1 nA). Cluster size and coverage increase with increasing amount of deposited material.

In the first stages of growth silver NPs nucleates preferentially on the MgO dislocation lines, clearly evident in sub-Å images [Fig.4.21(a-d)], and reach almost total coverage at 2 Å nominal thickness. A square cluster in-plane section can be observed, suggesting a growth exposing (001) surface, favoured by the small lattice mismatch between Ag and MgO lattice of 3%. The reported results are in agreement with previous works. [130, 153, 158]. Cluster density, coverage, average apparent diameter and height, determined by the procedure described in Sec.4.1, are reported in Table 4.2.

| <i>Nom.Thick.</i> (Å) | <i>Density</i> (m^{-2}) | <i>Coverage</i> (%) | <i>Diameter</i> (nm) | <i>Height</i> (nm) |
|--------------------------|--------------------------------|------------------------|-------------------------|-----------------------|
| 0.05 | 0.4×10^{16} | 2.5 | 2.0 ± 0.5 | 0.6 ± 0.3 |
| 0.1 | 1.6×10^{16} | 10 | 2.7 ± 0.6 | 0.8 ± 0.4 |
| 0.25 | 1.9×10^{16} | 13 | 2.9 ± 0.6 | 1.0 ± 0.3 |
| 0.5 | 1.3×10^{16} | 20 | 4.5 ± 0.5 | 1.6 ± 0.3 |
| 1 | 1.7×10^{16} | 50 | 6.0 ± 1.0 | 2.0 ± 0.5 |
| 2 | 3.0×10^{16} | 90 | 6.2 ± 1.0 | 3.2 ± 0.5 |

Table 4.2: *Morphological parameters of Ag/MgO/Mo as determined by STM images analysis.*

For thickness lower than 1 Å automatic cluster selection can be used, while the partial superposition of NPs in high coverage images has made manual determination of diameter and height preferable. In the first case, uncertainty on obtained values was given as standard deviation, in the second, it has been set to 1 nm for diameter and 0.5 nm for height. Sizes and coverage increase with increasing nominal thickness, while between 0.1 Å and 1 Å cluster density, which means number of NPs per unit area, does not experience significant changes. Aspect ratio determined as d/h is around 3, corresponding to flat clusters.

Also in this case, as previously observed on Ag/ZrO₂ cluster, in-plane section is symmetrical, thus NPs can be approximated either with spherical or spheroidal shape. To determine which shape is the most suitable to describe Ag growth on the oxide, plasmonic properties of the material can be studied and related to morphological parameters in a double-check analysis which allows to get a deeper insight on both morphological and optical properties.

Plasmonic properties

Plasmonic properties of silver NPs on MgO have been probed by EELS technique, described in Sec.4.2.1. A survey spectrum, with indication of the main structures for 4 Å Ag/MgO is reported in Fig.4.22(a). EELS peak energy can be determined by a fit including interband transition structure of MgO substrate (5.6 eV), interband transition structure of Ag (about 4 eV, 3.98 in literature [161]) and two gaussian peaks for plasmonic resonances. A gaussian peak has been added to reproduce the low intensity structure at about 1 eV, which is also observable on clean MgO film and thus possibly related to Mo substrate. An example of the fit for 2 Å Ag/MgO is reported in Fig.4.22(b), showing the split of LSPR into two plasmonic modes, referred as the parallel (lower energy) and perpendicular (higher energy) ones.

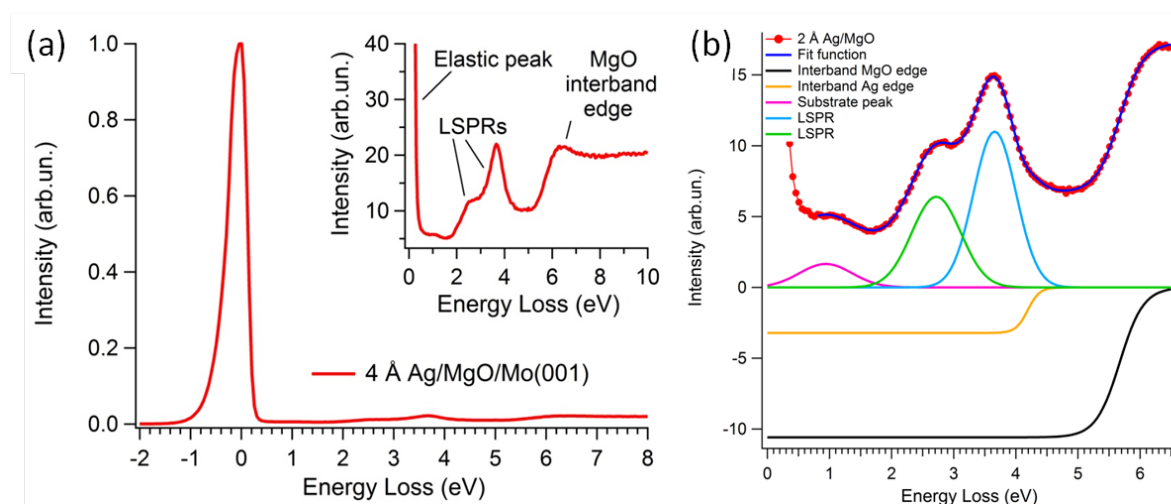


Figure 4.22: Ag/MgO/Mo EELS spectra. (a) Survey spectrum of 4 Å Ag/MgO/Mo and inset with indication of the main observable structures. (b) Spectrum of 2 Å Ag/MgO/Mo: fit function and single components obtained from fitting procedure.

Spectra obtained for increasing deposited silver nominal thicknesses are reported in Fig.4.23: between 0 eV and 5.6 eV a double peak is observable, whose intensity increases with the amount of deposited Ag. The split into two distinct components, identified as the parallel and the perpendicular modes, is related to a break in symmetry which can be introduced by different parameters, as described in Sec.1.2. Plasmon resonances peaks energy determined by fitting procedure is reported in Table 4.3

As reported by Lazzari et al. [134], peak at 2.7-3.1 eV corresponds to parallel mode and is actually more sensitive to cluster properties variations, while peak at 3.6-3.7 eV is attributed to perpendicular mode which has been reported to show smaller shifts with respect to parallel one. At a first glance, EELS plasmonic peaks show a shift to lower energy (redshift) with increasing amount of deposited silver.

To identify which parameters influences the plasmonic properties of the sample a comparison with morphological analysis is needed, which will be presented in the following sections.

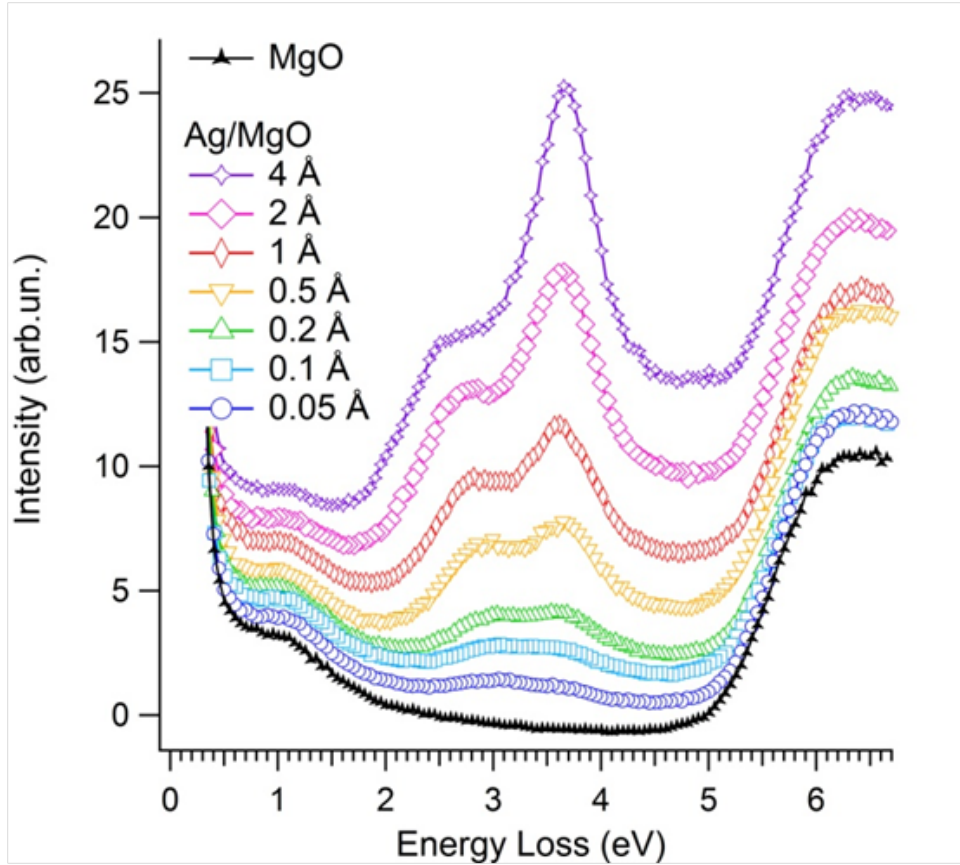


Figure 4.23: *Ag/MgO/Mo EELS spectra for increasing amount of deposited silver. For the sake of clarity, the spectra have been vertically shifted with respect of each other.*

| <i>Nom.Thick.</i> (Å) | E_{par} (eV) | E_{per} (eV) | $E_{per} - E_{par}$ (eV) |
|--------------------------|-------------------|-------------------|-----------------------------|
| 0.05 | 3.02 | 3.73 | 0.71 |
| 0.1 | 3.15 | 3.73 | 0.58 |
| 0.25 | 2.94 | 3.68 | 0.74 |
| 0.5 | 2.80 | 3.63 | 0.83 |
| 1 | 2.80 | 3.64 | 0.84 |
| 2 | 2.76 | 3.69 | 0.93 |
| 4 | 2.75 | 3.71 | 0.96 |

Table 4.3: *Plasmonic peaks energy of Ag/MgO/Mo for parallel and perpendicular mode and their relative difference, as determined by EELS spectra analysis.*

Relating morphology to plasmonic properties

To relate morphology and plasmonic properties, leading to a better understanding of both aspects, a simulation of EELS cross section based on STM parameters has been performed, using *GranFilm* software developed by Lazzari et al. [131], which computes island polarizabilities accounting for the multipolar coupling with the substrate.

From parallel (α_{par}) and perpendicular (α_{per}) polarizabilities, cluster density and substrate dielectric function (ϵ_{MgO} , in this case), total cross section θ_{tot} is calculated as the sum of parallel and perpendicular components:

$$\theta_{par} = \alpha_{par} n_c \left| \frac{1}{1 + \epsilon_{MgO}} \right|^2 \quad \theta_{per} = \alpha_{per} n_c \left| \frac{\epsilon_{MgO}}{1 + \epsilon_{MgO}} \right|^2 \quad (4.19)$$

$$\theta_{tot} = \theta_{par} + \theta_{per} \quad (4.20)$$

Simulations consider either spherical or spheroidal particles; input parameters are, among the others: islands and substrate material, island size (radius for sphere and semiaxis for spheroid), truncation parameter, coverage and cluster density. Thus, parameters obtained by STM images analysis can be used as starting point to perform a simulation of EELS spectra and, from the matching with measured EELS results it is possible to obtain a more accurate estimate of island morphological properties. This procedure leads to a double goal: on one hand it permits to obtain more reliable information concerning particles morphological parameters, on the other it allows to relate them to optical response.

Optical response for both sphere and spheroids has been simulated to determine which one fits better. In simulations with spherical particles relevant parameters are height and coverage from STM and truncation parameter, in turn calculated from height and cluster density obtained by STM; spheroidal particle simulation requires one more parameter and a strong hypothesis: the equality between radius determined by STM and particle semiaxis ($R = a$), thus it relies on the less accurate diameter measurement. Since all STM parameters are affected by non-negligible errors, the determination of most accurate morphological properties is performed by a fitting procedure: starting from STM values, input data are changed comparing the obtained simulation data with measured spectra in terms of peaks energy and relative intensity and looking for the best correspondance. In sphere simulations height has been taken from STM measurements, while R , and as a consequence truncation parameter, has been fitted. The procedure has been iterated for different radius values and the best matching with experimental data has been identified. For spheroid simulations a parameter has been assigned, c has been calculated from eq.4.7 from height and volume and t_r was determined from eq.4.12; the process has been repeated for different a values looking for the best match.

As a general criterium, a good correspondance of both peaks energy and relative intensity, which determines total peak lineshape is required. If both requirements can not be met simultaneously, it has to be noted that in experimental spectra other structure are present, whose convolution with LSPRs modifies width and intensity of the resulting peak. Additionally, modeled peaks are expected to show more narrow structures than experimental ones.

Fig.4.24 reports best matching simulations both for spherical (a) and spheroidal (b) shape and experimental EELS data for 0.05 \AA Ag/MgO.

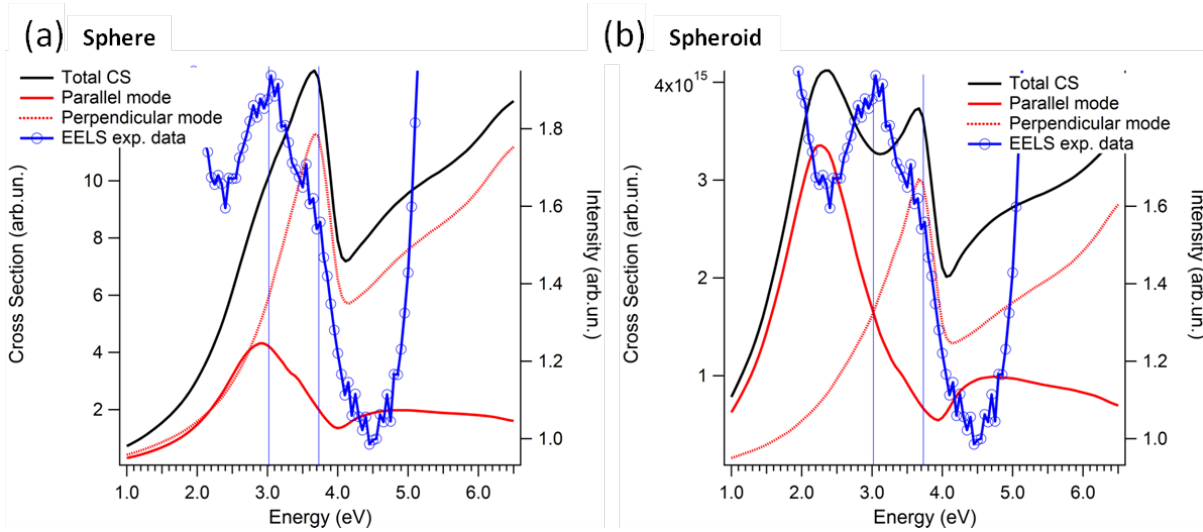


Figure 4.24: 0.05 \AA Ag/MgO/Mo EELS spectrum and (a) spherical and (b) spheroidal best matching simulations. Blue vertical lines indicates peak energy as determined by fitting experimental data.

Parallel and perpendicular mode show a low relative shift in energy. Even if the correspondance is not perfect, spherical shape simulation has been evaluated as the more accurate: peaks energy perfectly matches and the discrepancy in relative peaks intensities can be assigned to the presence of the other structure such as the peak at 1 eV. Besides, it has to be noted that simulated peaks are not single gaussian peaks, but a convolution of different structures. Spheroidal simulation has been excluded also because, as previously mentioned, experimental data are expected to be broadened with respect to model ones: in this case the difference difference of about 0.7 eV between calculated and measured parallel peak can not be ascribed to experimental error. The best matching radius for spherical particle shape is 0.6 nm, which is, as expected, lower than STM measured value (1 nm). It has to be mentioned that the low quantity of material and the consequent difficulties in fitting procedure strongly influence the obtained peak energy, thus the results for low silver nominal thicknesses are less reliable and should be treated cautiously.

As for lowest coverage sample, all the analyzed spectra show a better match with spherical shaped particle simulations rather than with spheroidal ones. Best matching spectra and simulation are reported in Fig.4.25.

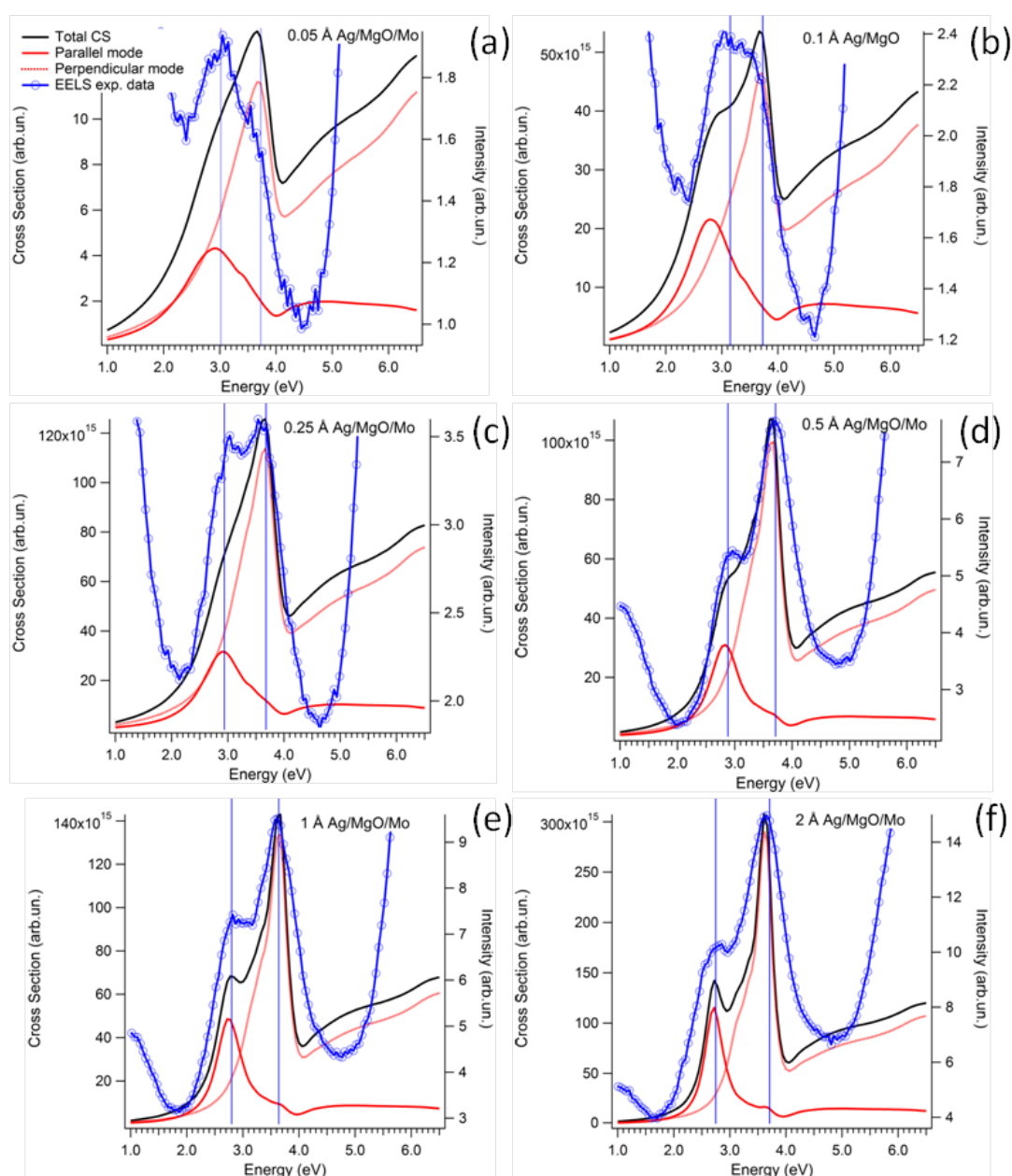


Figure 4.25: Ag/MgO/Mo EELS spectra and simulations for spherical particle shape with Ag nominal thickness ranging from 0.05 Å and 2 Å. Blue vertical lines indicate peak energy as determined by fitting experimental data.

Numerical values obtained by matching simulations and EELS measurements are reported in Table 4.4. Diameter from simulations is assigned to be most reliable value which describes particle size; consequently aspect ratio d/h is calculated from diameter obtained with simulations and height from STM analysis. Work of adhesion has also been calculated from contact angle value.

| <i>Nom.Thick.</i> (Å) | <i>Cov.</i> (%) | h_{STM} (nm) | d_{sim} (nm) | α (°) | d_{sim}/h_{STM} | W_{ad} (J/m ²) | E_{par} (eV) | E_{per} (eV) |
|--------------------------|--------------------|-------------------|-------------------|-----------------|-------------------|---------------------------------|-------------------|-------------------|
| 0.05 | 2.5 | 0.6 | 1.2 | 95 | 2.0 | 1.24 | 3.02 | 3.73 |
| 0.1 | 10 | 0.8 | 1.6 | 95 | 2.0 | 1.24 | 3.15 | 3.73 |
| 0.25 | 13 | 1.0 | 1.6 | 104 | 1.6 | 1.03 | 2.94 | 3.68 |
| 0.5 | 20 | 1.6 | 2.7 | 101 | 1.7 | 1.10 | 2.80 | 3.63 |
| 1 | 50 | 2.0 | 3.4 | 100 | 1.7 | 1.12 | 2.80 | 3.64 |
| 2 | 90 | 3.2 | 5.4 | 101 | 1.7 | 1.10 | 2.76 | 3.69 |

Table 4.4: *Morphological and optical parameters of Ag/MgO/Mo as determined by STM, EELS and GranFilm simulations analysis.*

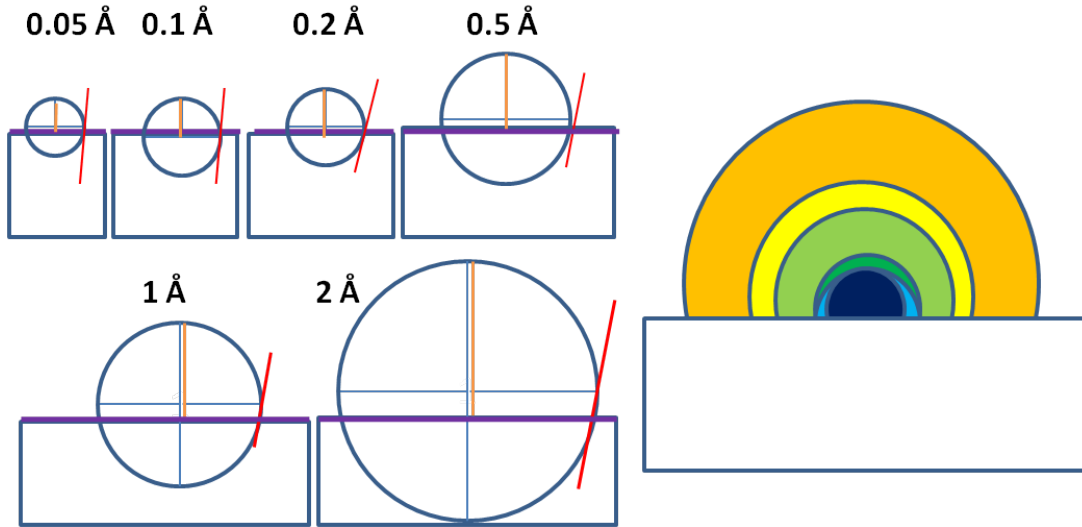


Figure 4.26: *Scale schematic representation of Ag NPs growth on MgO, from 0.05 Å to 2 Å nominal thickness. Purple lines indicate corresponding diameter as measured by STM.*

It is now possible to describe first stage of growth of Ag NPs on MgO (Fig.4.26). Silver deposited on MgO forms island which expose (100) surface and grow in Volmer-Weber mode due to the weak interfacial metal-oxide interaction [153]. For sub-Å nominal thickness cluster number increases, then between 0.1 Å and 1 Å the deposited material creates larger cluster without any significant change in NP density. From 1 to 2 Å NPs grow both larger and higher in number leading to an almost complete coverage at 2 Å.

Islands can be approximated with truncated spheres with aspect ratio close to 2 (semi-spheres), in accordance with the study by Benedetti et al. [153], where a aspect ratio between 2 and 1 was reported for cluster with nominal thickness between 1 and 10 Å and with the study by Lazzari et al., who measured an aspect ratio of 1.7 for 2 Å Ag deposited at RT [134]. Adhesion to the substrate decreases with increasing particle size, getting close to spherical shape, as already reported for Co and Pd NPs on alumina [145].

Morphological parameters (height, diameter and coverage) as a function of nominal Ag thickness are reported in Fig.4.27: trends are analogous and quite superimposed.

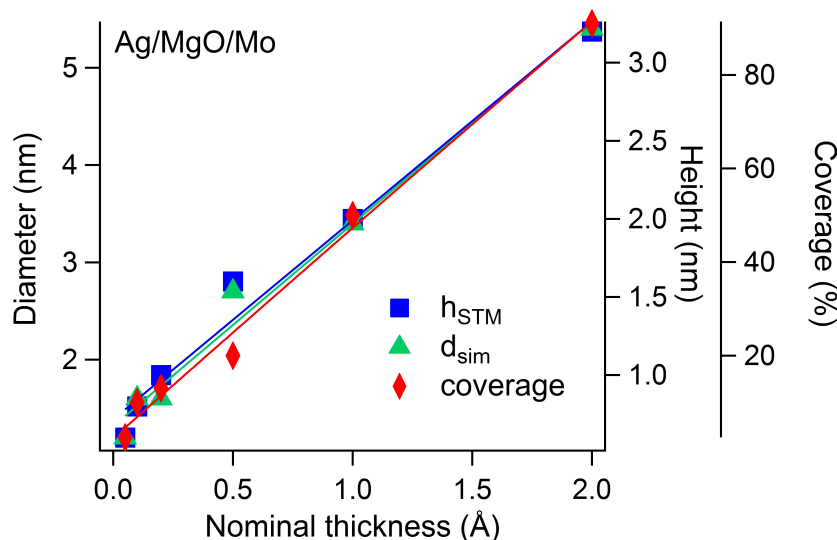


Figure 4.27: *Ag/MgO/Mo* morphological parameters as a function of nominal deposited Ag thickness. h and coverage have been determined by STM, d from matching with simulations of EELS spectra. Linear fit are reported as a guide to the eye.

Given morphological and plasmonic properties, some conclusions concerning their relation can be driven. As described in Sec.1.2, LSPRs energy depends on different parameters, which affect the optical response of the material. NPs size, shape and distribution play a fundamental role in determining plasmonic properties.

The best way to account for NPs size is by considering NPs volume, however, if all clusters show a similar shape, like in this case, diameter can be a sufficiently representative value. EELS peaks energy for parallel and perpendicular mode as a function of diameter are reported in Fig.4.28. Both peaks show an overall redshift with increasing size as expected for nanosized particle [25]; while parallel mode redshift covers a 0.4 eV range, perpendicular mode shift is less than 0.1 eV, which is close to the experimental error in peak energy determination.

Energy difference between peaks, which reflects relative shift, has also been reported: peak relative energy difference increases with increasing size. Since size affects both mode in the same direction (redshift with increasing dimensions), the quite insensitivity of perpendicular mode can be attributed to other competitive effects, such as interaction and shape variations.

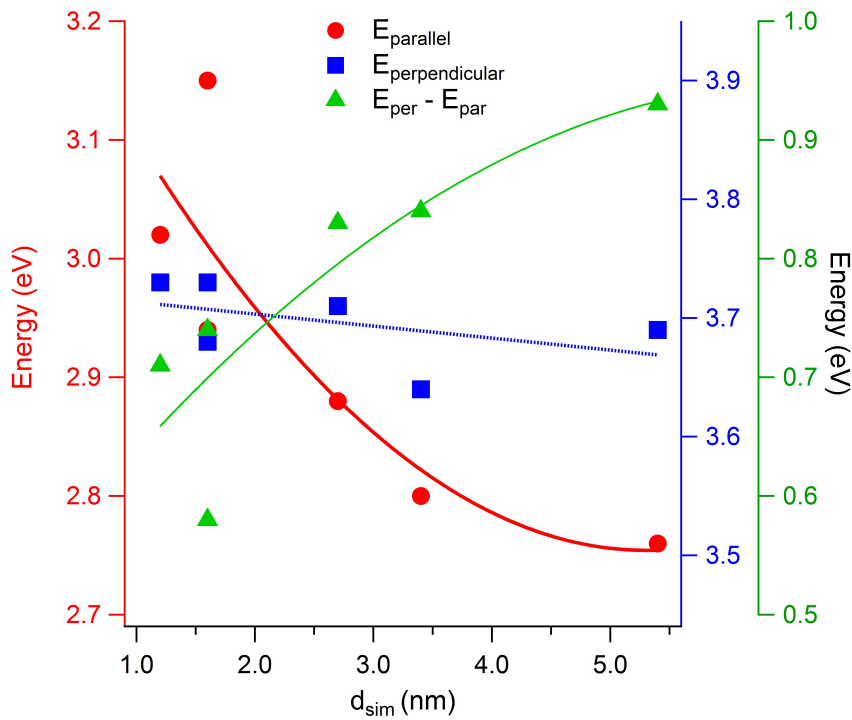


Figure 4.28: Ag/MgO/Mo EELS peaks energy for parallel and perpendicular plasmonic modes and their relative difference ($E_{per} - E_{par}$) as a function of NPs diameter determined by GranFilm simulations. Left axis is referred to parallel mode, first right axis to perpendicular mode, second right axis to relative energy difference. All axis cover the same energy range of 0.5 eV, thus relative variations can be directly compared. Parabolic (solid line) and linear (dotted line) fit for parallel and perpendicular modes and their energy difference act as a guide for the eye.

Particle shape is poorly affected by the increase in dimensions as testified by aspect ratio values ranging from 1.6 to 2. When particle gets close to spherical shape, which means when aspect ratio approaches value 1 ($d = h$), peaks energy difference is expected to decrease (due to blueshift of the parallel mode and redshift of the perpendicular one), which is the opposite of the observed overall trend. In Fig.4.29 single peaks energy and energy difference are reported, which highlights the absence of a clear trend. Thus, for Ag NPs deposited on MgO in this nominal thickness range, the effect of aspect ratio is negligible.

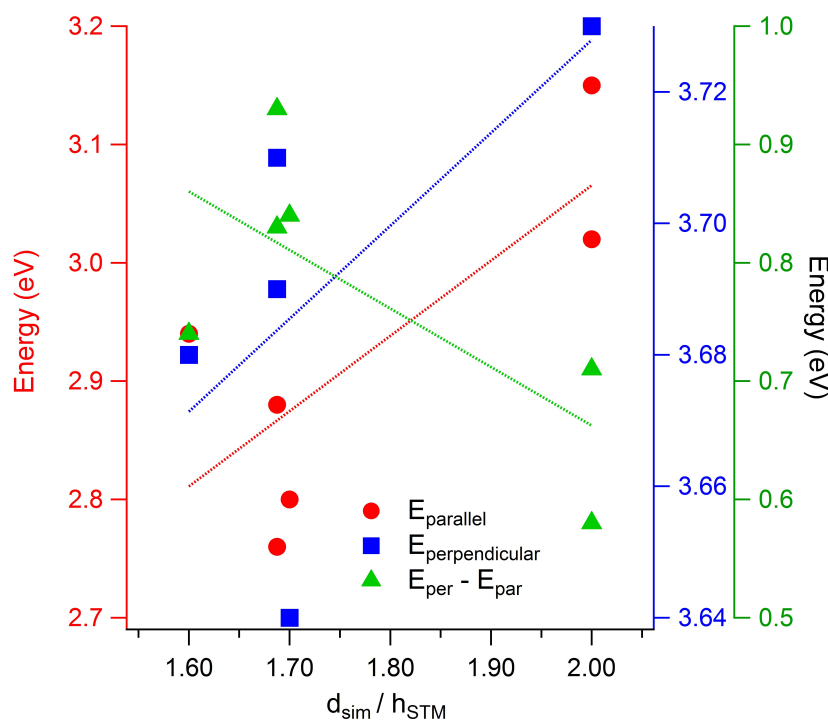


Figure 4.29: *Ag/MgO/Mo EELS peaks energy for parallel and perpendicular plasmonic modes and their relative difference as a function of NP aspect ratio d/h . Left axis is referred to parallel mode, first right axis to perpendicular mode, second right axis to relative energy difference. All axis cover the same energy range of 0.5 eV, thus relative variation can be directly compared. Trends are not well defined.*

The effect of particle interaction, which depends on the proximity of islands, has to be analyzed by considering both cluster density and diameter. Coverage can be a representative value which includes both cluster number and size, but it is strongly affected by tip shape. An alternative way to evaluate particle distribution is by calculating border-to-border distance. If an homogenous distribution can be hypothesized and if clusters can be approximated with truncated spheres located in the center of a square area, the area occupied by a single cluster is the inverse ratio of cluster density. Thus, center-to-center distance corresponds to the square area side, while border-to-border distance is obtained by subtracting sphere diameter from center-to-center distance. Summarizing, border-to-border distance L_{BB} is calculated from cluster density n_C and cluster diameter d_{sim} by the relation:

$$L_{BB} = \sqrt{\frac{1}{n_c}} - d_{sim} \quad (4.21)$$

Obviously also this quantity is affected by errors introduced by the approximation considered, by the error on simulated diameter and on cluster density.

Generally speaking, the dipole-dipole interparticle interaction affects polarizability and determines a redshift for parallel mode and a blueshift for perpendicular one, thus when particles are closer and the interaction is stronger, the energy difference between parallel and perpendicular mode is expected to increase. Thus, while size effect generates a redshift for both modes with increasing nominal thickness (due to the increase in dimensions), the effect of interaction is concordant for parallel mode and competitive for perpendicular one. Trends for plasmon peak energy as a function of coverage or border-to-border distance (not reported here) is analogous to the one considering diameter, since the trend of the two parameters are quite superimposable as shown in Fig.4.27. It is obviously impossible to disentangle the two effects when dealing with real particles whose size and distribution change simultaneously, thus both trends as a function of diameter and coverage show the two effects at the same time.

It has to be mentioned that in previous studies on Ag/MgO, both concerning measured [134] and calculated [24] peaks energy, perpendicular mode has been reported to suffer minor energy shift with respect to the more sensitive parallel mode. Thus, the lower redshift of perpendicular peak is not definitely assignable to interaction effect. A measurement where only one of the two parameters, distance or size, is changing, while the other remains fixed should help clarifying this point.

Summarizing, the non-spherical shape of NPs induce the split of LSPR into two plasmonic modes: a redshifted parallel mode and a blueshifted perpendicular mode. When particle size increase both modes are redshifted, but the perpendicular mode results quite unaffected by this effect. A possible explanation for this minor shift is the counteracting interaction effect, which generates an opposite blueshift for perpendicular mode; vice versa, a redshift of parallel mode is induced by increasing interaction, concordant to size shift and thus enhancing this effect.

4.2.3 The role of temperature

The role of temperature, both during deposition and after a subsequent annealing, has been analyzed. 0.5 Å nominal thickness has been chosen since it represents an intermediate value in the analyzed range and because the correspondance between measured and simulated EELS spectra has proved to be the best one. 0.5 Å Ag have been deposited on MgO substrate by keeping the oxide both at RT and at 523 K. The RT grown sample has also been subsequently annealed at 673 K.

All preparations result in similar morphologies [Fig.4.30(a-b)]: negligible or very low variations in morphology have been observed for annealed sample, while NPs deposited at 523 K appear slightly bigger. EELS peaks [Fig.4.30(c)] show a redshift of less than 0.1 eV with respect to RT as grown sample for both Ag NPs deposited at higher temperature or subsequently annealed, for both modes. Numerical values are reported in Table 4.5.

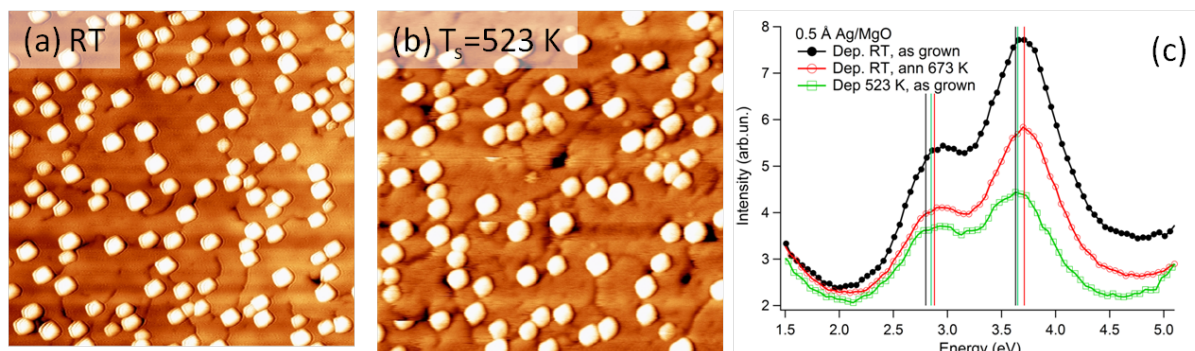


Figure 4.30: 0.5 \AA Ag/MgO/Mo. (a-b) $(100 \times 100) \text{ nm}^2$ STM images for Ag deposited at (a) RT and (b) with substrate temperature of 523 K (3.2 V, 0.05 nA). (c) EELS spectra for the different preparations. Vertical lines indicates peaks energy as determined by fitting procedure.

| Preparation | n_C (m^{-2}) | Cov (%) | d_{STM} (nm) | h_{STM} (nm) | E_{par} (eV) | E_{per} (eV) | $E_{par} - E_{per}$ (eV) |
|---------------------|-----------------------|------------|-------------------|-------------------|-------------------|-------------------|-----------------------------|
| Dep. RT, as grown | 1.3×10^{16} | 20 | 4.5 ± 0.5 | 1.6 ± 0.3 | 2.80 | 3.63 | 0.83 |
| Dep. RT, ann. 673 K | 1.0×10^{16} | 20 | 4.3 ± 0.6 | 1.6 ± 0.3 | 2.88 | 3.71 | 0.83 |
| Dep. 523 K | 0.9×10^{16} | 20 | 5.4 ± 0.6 | 1.6 ± 0.3 | 2.85 | 3.65 | 0.80 |

Table 4.5: Morphological parameters and plasmonic peak energy of 0.5 \AA Ag/MgO/Mo as determined by STM and EELS analysis.

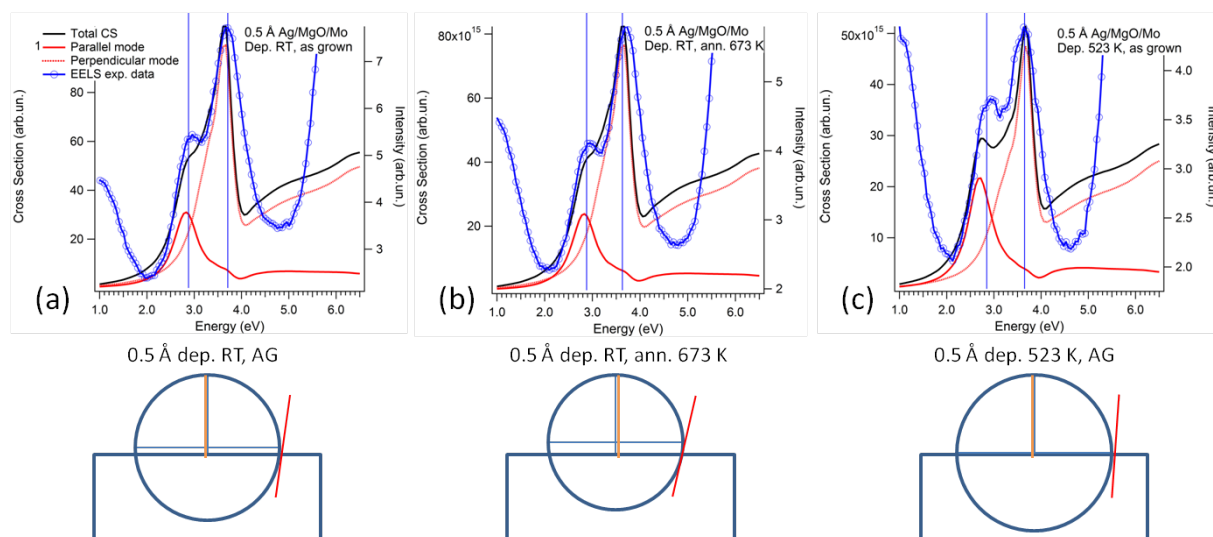


Figure 4.31: 0.5 \AA Ag/MgO/Mo. EELS spectra and simulations for spherical particle shape. Blue vertical lines indicate peak energy as determined by fitting experimental data and corresponding scale schematical representation. (a) silver deposited at RT, as grown and (b) after annealing at 673 K, (c) silver deposited with substrate temperature of 523 K.

Matching of simulations with EELS spectra show a very good correspondance (Fig.4.31). Particles can be modeled as truncated spheres with aspect ratio between 1.6 and 1.9. Simulated diameter are smaller than the one measured by STM and follow the same trend. Annealing at 673 K induces very little change in NP morphology, slightly decreasing particle diameter from 2.8 to 2.6 nm. On the contrary, clusters deposited at higher temperature appear bigger (3 nm diameter). Since no change in height occur, aspect ratio decrease in the first case and increase in the second. However, since differences in diameter and energy shifts are below experimental errors it seems reasonable to conclude that the effect of temperature in the considered range does not significantly affect morphological and optical properties.

4.2.4 Fe/MgO as a template to grow Ag NPs

Ag NPs grow epitaxially on MgO substrate, but the distribution is not ordered. The growth of silver NPs can be modified by introducing a template of clusters which spontaneously form a regular array the oxide substrate, like the case of Fe, leading silver deposition to an ordered distribution [153, 157].

0.5 Å Ag have been grown on 0.4 Å Fe previously deposited on clean MgO substrate, successfully resulting in a well ordered distribution, testified by the Fourier transform of the image which shows defined intensity peaks (Fig.4.32). Additionally, Fe islands act as preferential sites for adsorption, favouring the growth of a higher number of silver NPs, as reported by density increasing by a factor 4.5. EELS spectra in Fig.4.33 show a significant blueshift of both peaks with respect to the sample where Fe is absent, more relevant for parallel mode. Peaks difference is significantly reduced resulting in a broad unique peak. Numerical values are reported in Table 4.6.

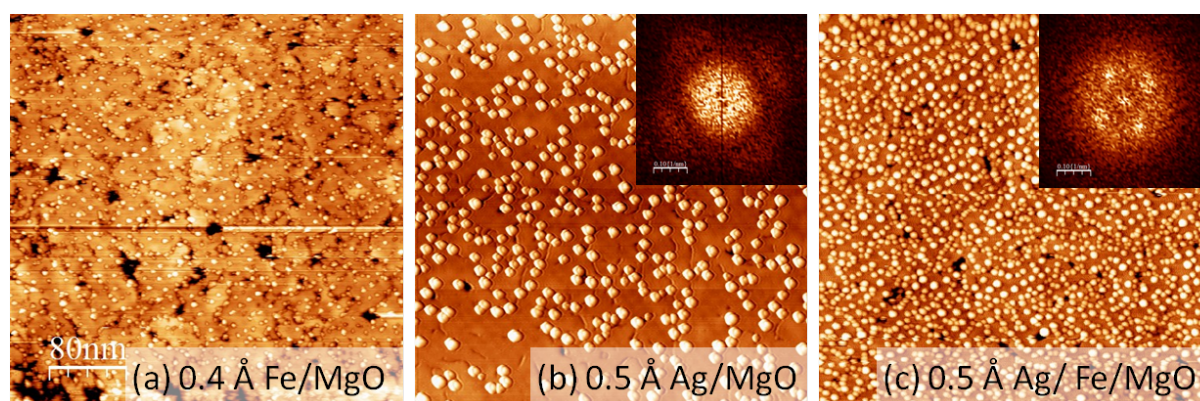


Figure 4.32: $(200 \times 200) \text{ nm}^2$ STM images for (a) 0.4 Å Fe/MgO/Mo (3.2 V, 0.04 nA), (b) 0.5 Å Ag/MgO/Mo (3.2 V, 0.06 nA) and (c) 0.5 Å Ag/0.4 Å Fe/MgO/Mo (3.8 V, 0.04 nA). Inset in images (b) and (c) show Fourier transform of corresponding STM image.

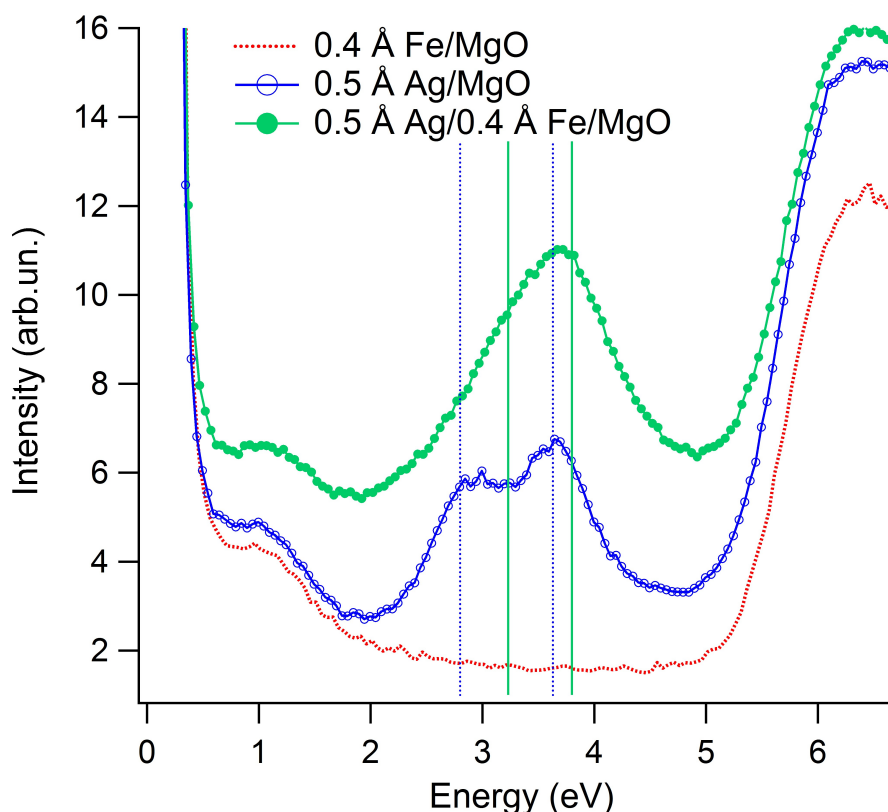


Figure 4.33: *EELS spectra for 0.4 Å Fe/MgO/Mo, 0.5 Å Ag/MgO/Mo and 0.5 Å Ag/0.4 Å Fe/MgO/Mo. Vertical lines indicate peak energy as determined by fitting procedure.*

| | n_C (m^{-2}) | Cov (%) | d_{STM} (nm) | h_{STM} (nm) | E_{par} (eV) | E_{per} (eV) | $E_{par} - E_{per}$ (eV) |
|-----------|-----------------------|--------------|-------------------|-------------------|-------------------|-------------------|-----------------------------|
| Ag/MgO | 1.3×10^{16} | 20 | 4.5 ± 0.5 | 1.6 ± 0.3 | 2.80 | 3.63 | 0.83 |
| Ag/Fe/MgO | 5.8×10^{16} | 33 | 3.0 ± 0.5 | 0.8 ± 0.3 | 3.23 | 3.80 | 0.57 |

Table 4.6: *Morphological parameters and plasmonic peaks energy of 0.5 Å Ag NPs deposited on clean MgO or on Fe/MgO as determined by STM and EELS analysis.*

In this case, the effect on LSPRs are related not only to the modification in morphology induced by the ordered template, but also to the coupling between dielectric functions the involved materials. Not only coupling between Fe, MgO and Ag has to be considered, but also image charge transfer generated between Fe and Mo substrate, thus the electronic interaction which affects plasmonic resonances is not simple to describe. For this reason, simulation of this system can result quite complicated and thus, determination of diameter and shape is not trivial. However, some qualitative consideration can be drawn. When considering the relative relation between diameter measured by STM and by simulations, a good correspondance can be found in these terms: an equal diameter measured by STM corresponds to an equal simulated diameter. The morphology of Ag/Fe system

is quite analogous to the one of 0.1 and 0.2 Å Ag/MgO in terms of apparent diameter and height, thus an analogous geometry can be hypothesized, describing Ag/Fe NPs as a semisphere with diameter equal to about 1.6 nm. Considering both apparent dimensions and hypothesized ones, NP diameter and height are lower for Ag NP/Fe/MgO with respect to Ag NPs on MgO and thus blueshift can be reasonably assigned to size effect. No simple explanation can be found for shape and distribution contributes: both increasing aspect ratio and coverage should lead to a higher energy difference (redshift of parallel mode and blueshift of perpendicular one), on the contrary a broad almost unique peak formed by the superposition of the two modes, here very close in energy, is observed. The effect of less evident modes splitting can be ascribed to the coupling between different dielectric constant introduced by adding Fe on the substrate.

4.3 Ag/ZnO

The association of Ag NP with a semiconductor oxide like ZnO can possibly open the way to the use of this system to improve performances in photovoltaic devices. Despite the high interest of this topic, the studies about this metal-oxide system are not many and all deal with the polar ZnO surfaces [136–138].

ZnO is a narrow bandgap oxide, so wetting is expected to be favoured: in fact flat clusters with high aspect ratio are formed on hexagonal ZnO (000 $\bar{1}$) surface, which grow along the Ag(111) plane [137]. SDR spectra show a double peak with components located at about 3.2 and 3.5 eV respectively (see Fig.4.34). Ag NPs, with nominal thickness ranging from 5 Å to 40 Å, have been mimicked by truncated oblate hemispheroids with aspect ratio equal to 8, obtaining morphological informations by optical SDR analysis [136].

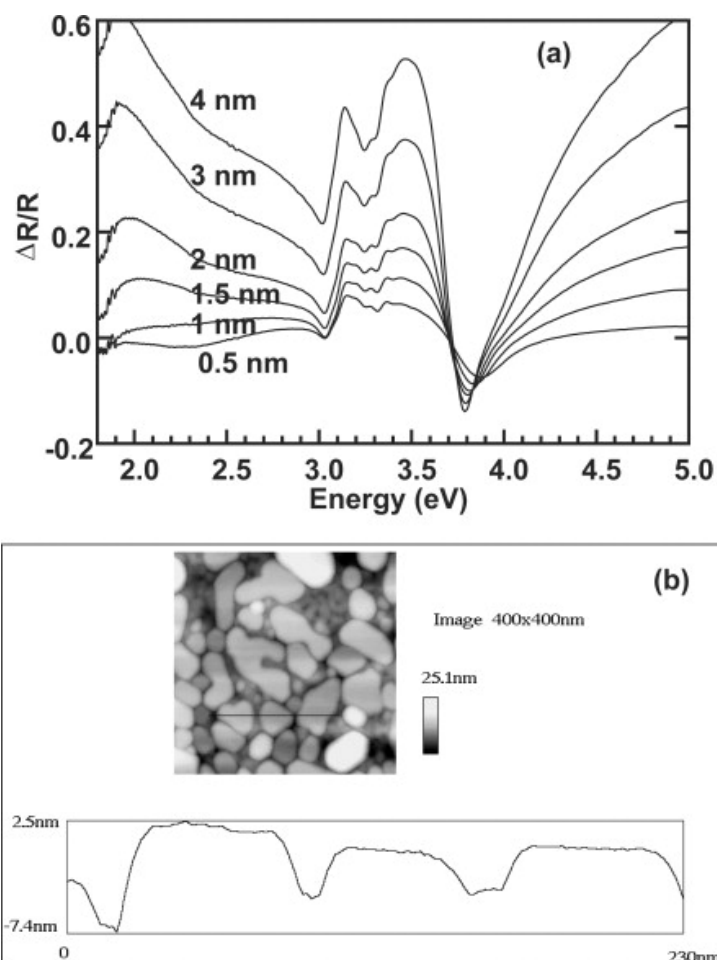


Figure 4.34: Silver deposited on the oxygen-rich polar ZnO (000 $\bar{1}$) plane at room temperature: (a) SDR spectra; (b) AFM image of the final deposit recorded in air. The height profile is shown along the line drawn in figure. Both SDR and AFM characterize a Volmer–Weber growth mode with cluster having high aspect ratios [137, 138].

In the work of Jedrecy et al. [138] lower Ag thicknesses, ranging from 2 Å to 16 Å, on both Zn- and O- terminated ZnO(0001) surface have been investigated by means of GISAXS (grazing incidence small-angle x-ray scattering). The measured aspect ratios, between 1.6 and 3.5, depend on the termination of the oxide surface: a lower adhesion (aspect ratio closer to 1) has been observed on the O-terminated plane. Aspect ratio does not show a monotonic trend with respect to nominal thickness, while both cluster size and inter-island distance are reported to increase.

To my knowledge, any studies concerning the growth of Ag nanoparticles on ZnO non-polar ($10\bar{1}0$) surface have not been performed so far, and a correlation between morphology and plasmonic properties is still missing. The Ag/ZnO($10\bar{1}0$) represents a suitable model case to study the interaction in this metal-oxide system and has been analysed in the next section.

4.3.1 Growth of Ag NP on ZnO

Silver NPs have been deposited on a ZnO($10\bar{1}0$), with nominal thickness ranging from 0.1 Å to 1 Å, to analyze first stages of growth and relate morphology to plasmonic properties. Since ZnO is a wide band gap semiconductor, a bulk crystal can be used as a substrate, which has been prepared by sputtering [$E = 0.6 - 1$ keV, $p(\text{Ar}) = 1 \times 10^{-6}$ mbar] and annealing in UHV (1073 K) cycles. The cleanliness of the surface has been checked by AES, while the good crystalline structure has been verified by LEED. STM and EELS measurements have been performed in the same experimental conditions as for Ag/MgO/Mo system. STM image of clean ZnO($10\bar{1}0$) surface is reported in Fig.4.35: the flat rectangular terraces separated by one monolayer step height (about 2.6 Å) already measured by Dulub et al. [7] are observable on the surface.

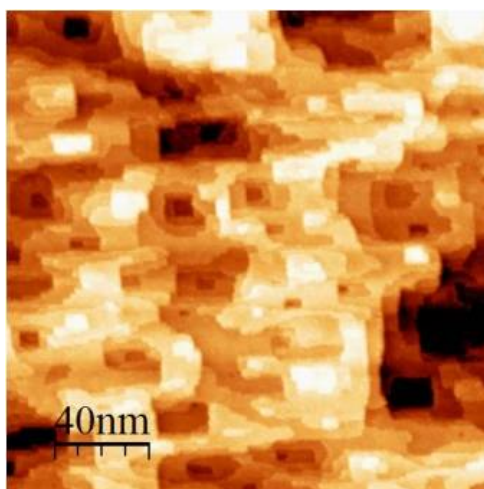


Figure 4.35: (200×200) nm^2 STM images for clean ZnO($10\bar{1}0$) (2 V, 0.05 nA).

Morphology

STM images of Ag grown on ZnO for both preparations (RT and with substrate kept at 673 K) are shown in Fig.4.36.

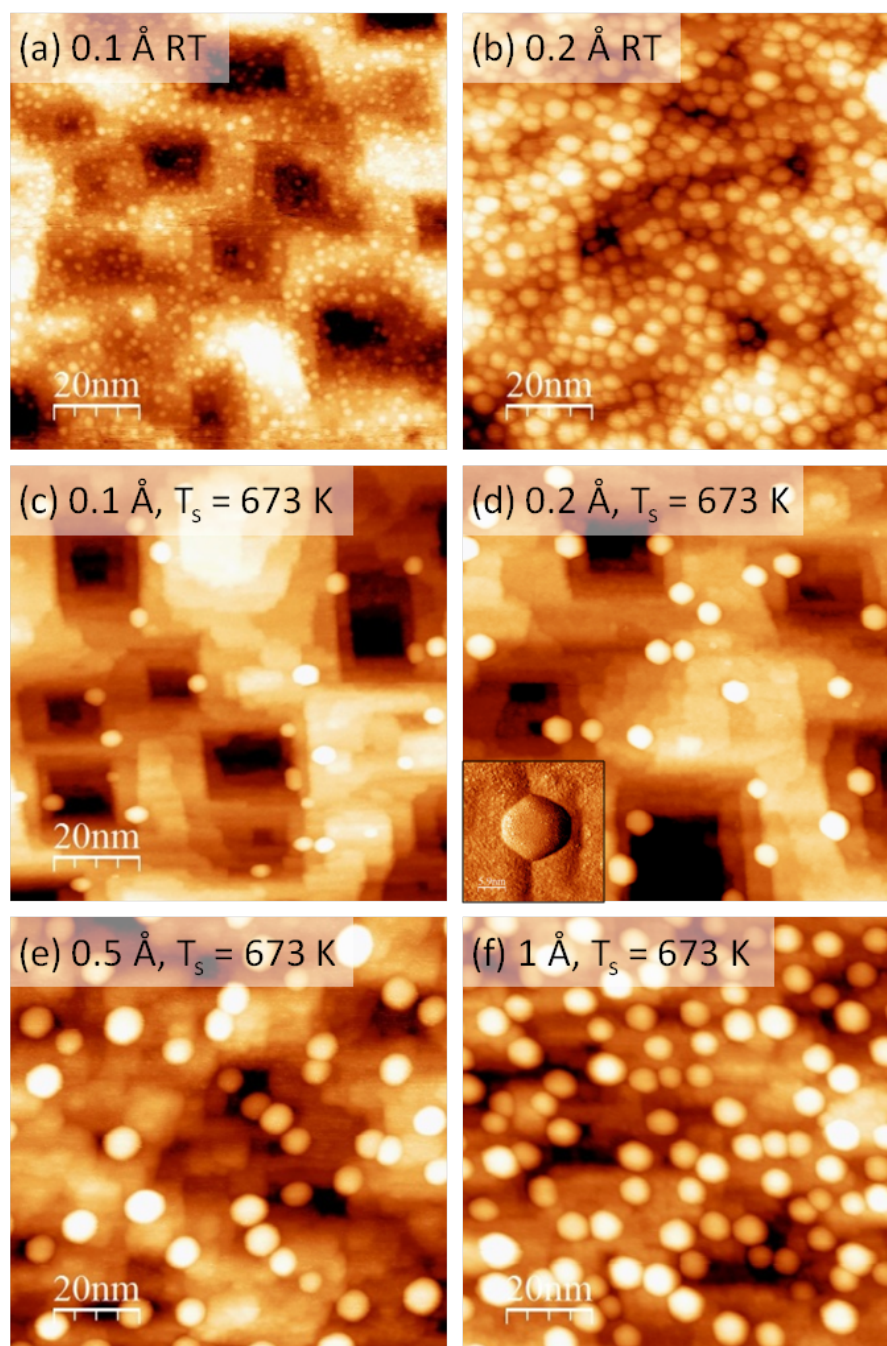


Figure 4.36: (100×100) nm^2 STM images for Ag/ZnO($10\bar{1}0$). (a) 0.1 Å grown at RT (2.3 V, 0.1 nA), (b) 0.2 Å grown at RT (3 V, 0.04 nA), (c) 0.1 Å grown at $T_s = 673$ K (2 V, 0.05 nA), (d) 0.2 Å grown at $T_s = 673$ K (2.3 V, 0.05 nA), (e) 0.5 Å grown at $T_s = 673$ K (2.7 V, 0.04 nA) and (f) 1 Å grown at $T_s = 673$ K (2.6 V, 0.04 nA). Inset in image (d) shows the derivative of STM image highlighting hexagonal island shape.

When silver is deposited at RT clusters do not show any preference for the site of adsorption and form an uniform distribution on the oxide surface. Small clusters with high density have been observed for low amount of material deposited (0.1 Å nominal thickness), and almost complete coverage is reached at 0.2 Å nominal thickness while cluster dimensions increase without significant density variation [Fig.4.36(a-b)]. The morphology of cluster deposited at 673 K is quite different: islands grow preferentially on terraces borders and appear bigger than the one formed at RT; clusters density and size increase with increasing thickness; at 1 Å nominal thickness coverage is about 50% [Fig.4.36(c-f)]. Ag islands show hexagonal shape, compatible with growth on Ag fcc(111) surface, as reported for silver clusters growth on ZnO(0001) plane [137]. In this case substrate unit cell is rectangular, with parameters $a = 3.25$ Å and $c = 5.21$ Å; silver lattice parameter of hexagonal (111) surface is $l = 5.78$ Å, thus the expected lattice mismatches of Ag growing along $[1\bar{2}1]$ direction exposing fcc(111) plane are: $\frac{(2a-l)}{2a} = 11\%$ and $\frac{(c-h)}{c} = 4\%$ (Fig.4.37). These low mismatch values allow an epitaxial growth of Ag hexagonal lattice on ZnO rectangular lattice, as testified from islands shapes. Morphological parameters, as determined by STM are reported in Table 4.7.

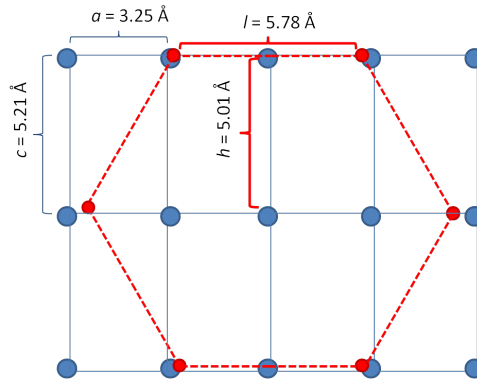


Figure 4.37: Schematic representation of epitaxial growth of Ag on ZnO($10\bar{1}0$). Blue solid lines represents ZnO lattice, red dotted line Ag lattice. The small mismatch favours the growth along $[1\bar{2}1]$ direction exposing fcc(111) plane.

| Nom.Thick. (Å) | T_s (K) | Density (m^{-2}) | Coverage (%) | Diameter (nm) | Height (nm) |
|-------------------|--------------|-------------------------|-----------------|------------------|----------------|
| 0.1 | RT | 5.4×10^{16} | 30 | 1.6 ± 0.3 | 0.8 ± 1.0 |
| 0.2 | RT | 5.6×10^{16} | 90 | 4.0 ± 0.6 | 1.5 ± 0.8 |
| 0.1 | 673 | 2.5×10^{15} | 3 | 4.4 ± 0.8 | 1.6 ± 1.0 |
| 0.2 | 673 | 3.0×10^{15} | 10 | 4.6 ± 0.5 | 1.8 ± 1.0 |
| 0.5 | 673 | 5.0×10^{15} | 30 | 7.4 ± 0.4 | 1.5 ± 1.0 |
| 1 | 673 | 1.2×10^{16} | 50 | 7.2 ± 0.5 | 1.6 ± 0.8 |

Table 4.7: Morphological parameters of Ag/ZnO as determined by STM images analysis.

Plasmonic properties

EELS spectra for Ag/ZnO are reported in Fig.4.38. Since ZnO bandgap is between 3 and 4 eV, oxide interband transition structure is partially superimposed to LSPRs peaks, in particular to perpendicular mode (about 3.8 eV), while parallel mode is located inside the gap, between 2.4 and 2.8 eV.

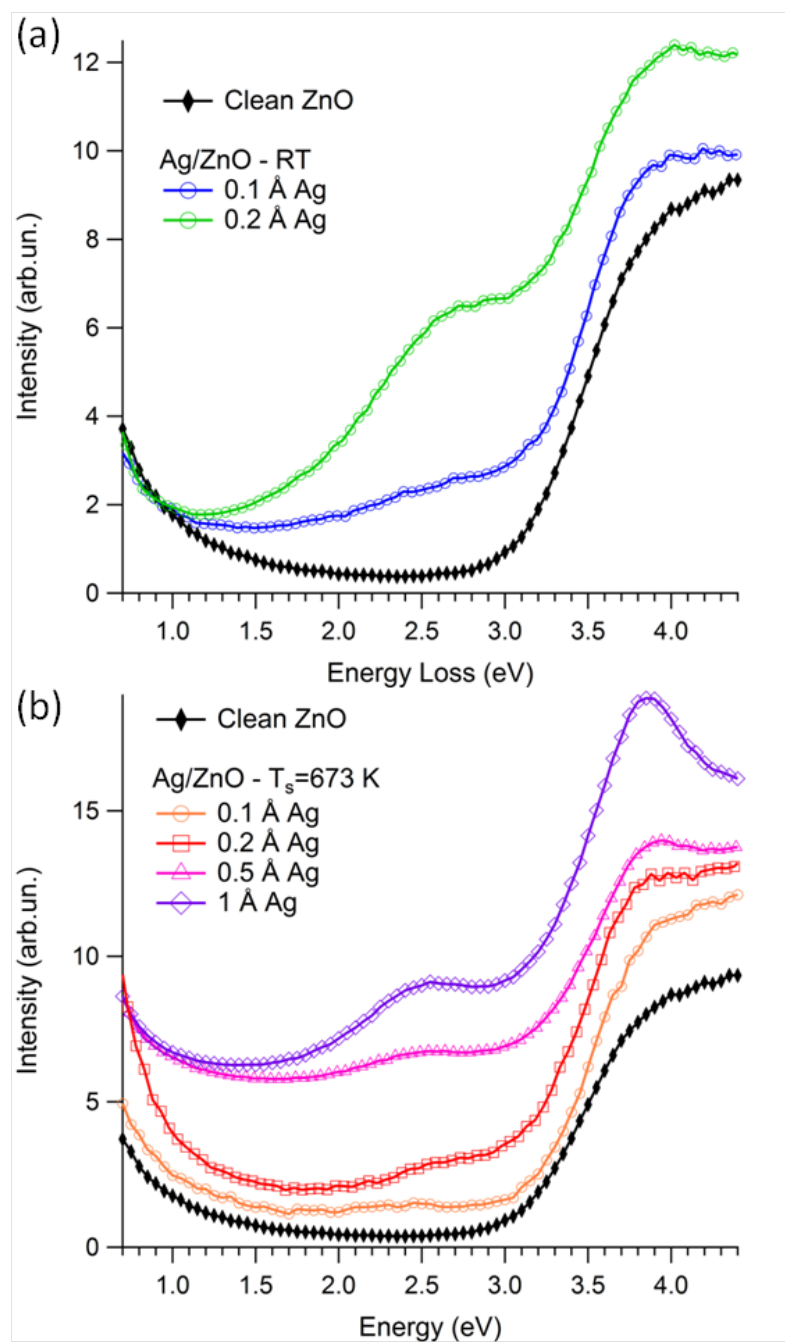


Figure 4.38: Ag/ZnO EELS spectra for increasing amount of silver deposited at (a) RT and (b) 673 K. For the sake of clarity, the spectra have been vertically shifted with respect of each other.

Fitting procedure, which is in this case more complex than for Ag/MgO due to the superposition of different structures, has been performed considering two gaussian peaks to model LSPRs, ZnO interband transition structure and a gaussian peak at zero energy to mimic the background. Ag interband transition structure was not included since it has been verified that the contribution was negligible or lead to non-physical results. EELS numerical results are reported in Table 4.8. It is immediately noticeable that plasmonic resonances are clearly distinguishable and that their energy difference is around or more than 1 eV, so higher than in Ag/MgO case for both preparations; energy separation between modes is higher for Ag deposited at 673 K.

| <i>Nom.Thick.</i> (Å) | T_s (K) | E_{par} (eV) | E_{per} (eV) | $E_{per} - E_{par}$ (eV) |
|--------------------------|--------------|-------------------|-------------------|-----------------------------|
| 0.1 | RT | 2.88 | 3.72 | 0.85 |
| 0.2 | RT | 2.73 | 3.73 | 1.00 |
| 0.1 | 673 | 2.45 | 3.80 | 1.35 |
| 0.2 | 673 | 2.59 | 3.81 | 1.22 |
| 0.5 | 673 | 2.49 | 3.80 | 1.31 |
| 1 | 673 | 2.51 | 3.83 | 1.32 |

Table 4.8: *Plasmonic peaks energy of Ag/ZnO for parallel and perpendicular mode and their relative difference, as determined by EELS spectra analysis.*

Relating morphological to plasmonic properties

Simulations with *GranFilm* software have been performed to determine particle geometry, both considering spherical and spheroidal shape. Also in this case, as for Ag/MgO, particles are better modeled by truncated spheres with aspect ratio close to 2. Simulations results compared with EELS peaks are reported in Fig.4.39. In ZnO case peak relative intensity is not trivial to evaluate, since peaks are superimposed to ZnO interband transition structure, thus peaks positions rather than shape have been mainly considered. Morphological and plasmonic properties of Ag NPs deposited on ZnO are summarized in Table 4.9. Growth of Ag NPs on ZnO is strongly affected by substrate temperature during deposition resulting in a different distribution of clusters with different evolution with increasing coverage. NPs can be modeled as truncated spheres with aspect ratio close to 2, which means by approximate semispheres, as on MgO substrate. A schematic representation of Ag NPs growth on ZnO for the different preparations is reported in Fig.4.40. The almost constant diameter obtained by simulations for clusters deposited at 673 K is in contrast with STM results, where size was reported to almost double from 0.2 to 0.5 Å nominal thickness, which evidences the strong dependence of STM parameters on tip shape and cleanliness and the high potential of simulations in clarifying actual particle properties.

| <i>Nom.Thick.</i> (Å) | T_s (K) | <i>Cov.</i> (%) | h_{STM} (nm) | d_{sim} (nm) | α (°) | d_{sim}/h_{STM} | W_{ad} (J/m ²) | E_{par} (eV) | E_{per} (eV) |
|--------------------------|--------------|--------------------|-------------------|-------------------|-----------------|-------------------|---------------------------------|-------------------|-------------------|
| 0.1 | RT | 30 | 0.8 | 1.4 | 95 | 1.8 | 1.24 | 2.88 | 3.72 |
| 0.2 | RT | 90 | 1.5 | 2.4 | 104 | 1.6 | 0.94 | 2.73 | 3.73 |
| 0.1 | 673 | 3 | 1.6 | 3.0 | 94 | 1.9 | 1.27 | 2.45 | 3.80 |
| 0.2 | 673 | 10 | 1.8 | 3.0 | 101 | 1.7 | 1.10 | 2.59 | 3.81 |
| 0.5 | 673 | 30 | 1.5 | 3.2 | 86 | 2.1 | 1.45 | 2.49 | 3.80 |
| 1 | 673 | 50 | 1.6 | 3.2 | 90 | 2.0 | 1.36 | 2.51 | 3.83 |

Table 4.9: *Morphological and optical parameters of Ag/ZnO as determined by STM, EELS and GranFilm simulations analysis.*

It is now possible to relate plasmonic to morphological properties. For RT deposited NPs, parallel mode shifts to lower energy (redshift) increasing the amount of material, as expected for increasing NP size. On the contrary, the almost unchanged size of 673 K deposited NP is reflected in almost constant peaks positions with increasing thickness for both modes. The increase in coverage for higher nominal thickness should lead to a monotonic increase in energy difference between peaks, which is not the case, thus interaction does not play a relevant role. For RT deposited NPs, where size effect is more relevant due to the high increase in particle dimensions, also aspect ratio effect is almost negligible. On the contrary, for Ag grown at 673 K, where size does not change significantly, even small aspect ratio variation influences LSRPs energy: when increasing thickness from 0.1 to 0.2 Å, aspect ratio gets close to 1 leading to the expected decrease in energy difference, while at 0.5 Å the increase in aspect ratio, which is again close to 2 induces a bigger energy separation, which remains constant reaching 1 Å nominal thickness as aspect ratio does not change much. Since perpendicular peak shift are almost negligible (less than 0.05 eV), it is possible to conclude that this mode is quite insensitive to aspect ratio effect, as already reported by Lazzari et al. [24]. In this case the effect of interaction is in clear opposition with the expected behavior, thus the lower shift of perpendicular mode can not be assigned to distribution effect. This conclusion can possibly suggest that the reason for lower shift of perpendicular mode are ascribed, also in MgO case, to the nature of the mode rather than to the previously hypothesized effect of interaction.

The higher energy difference between peaks reported for 673 K grown NPs with respect to RT deposited clusters is assignable mainly to size increase, redshifting parallel mode as a main effects. In fact RT deposited NPs are smaller even when the same amount of material is considered and aspect ratio trend, considering all preparations, is not well defined.

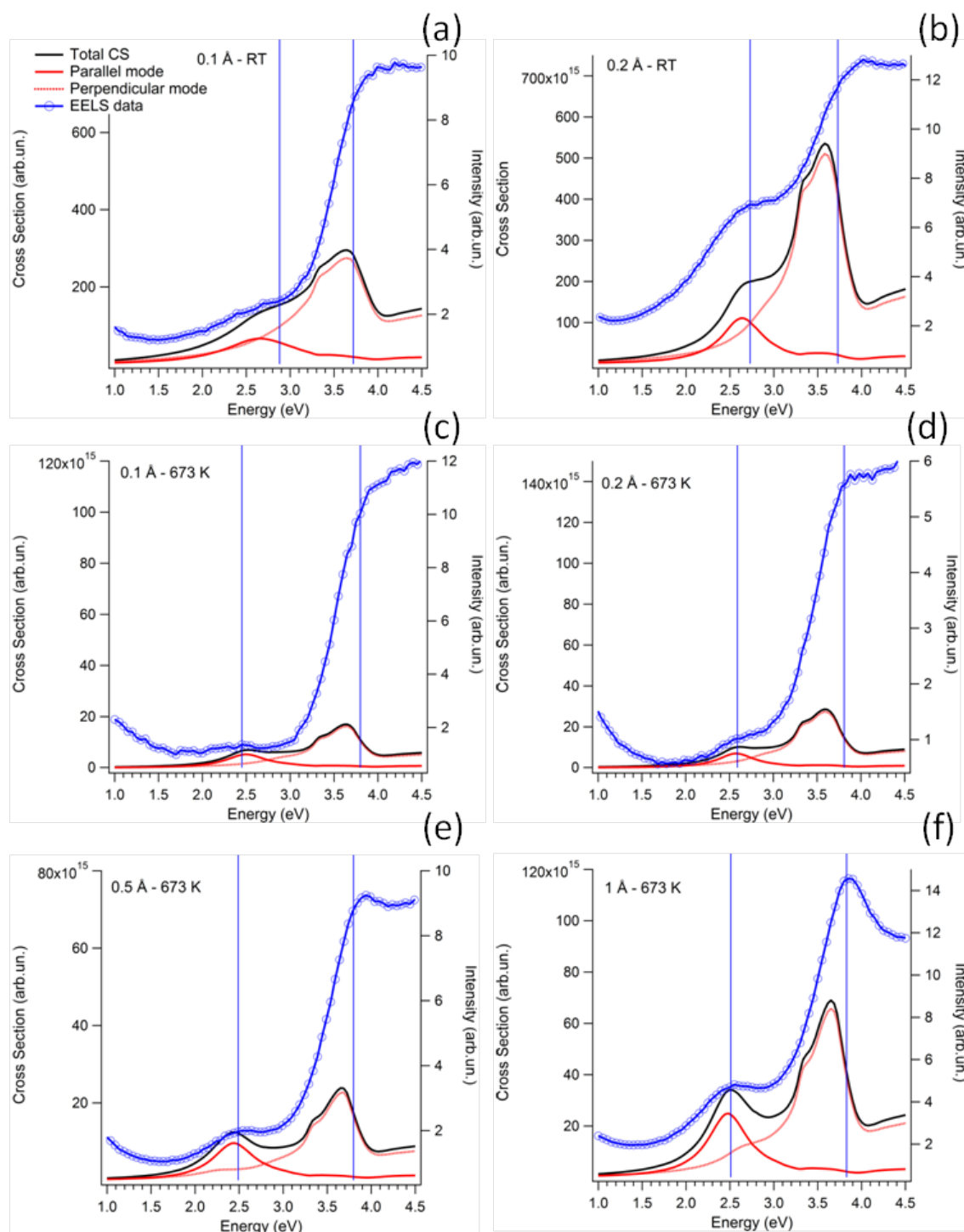


Figure 4.39: *Ag/ZnO EELS spectra and simulations for spherical particle shape for different preparations: (a) 0.1 Å grown at RT, (b) 0.2 Å grown at RT, (c)-(f) 0.1, 0.2, 0.5 and 1 Å grown with substrate temperature kept at 673 K. Blue vertical lines indicate peaks energy as determined by fitting experimental data.*

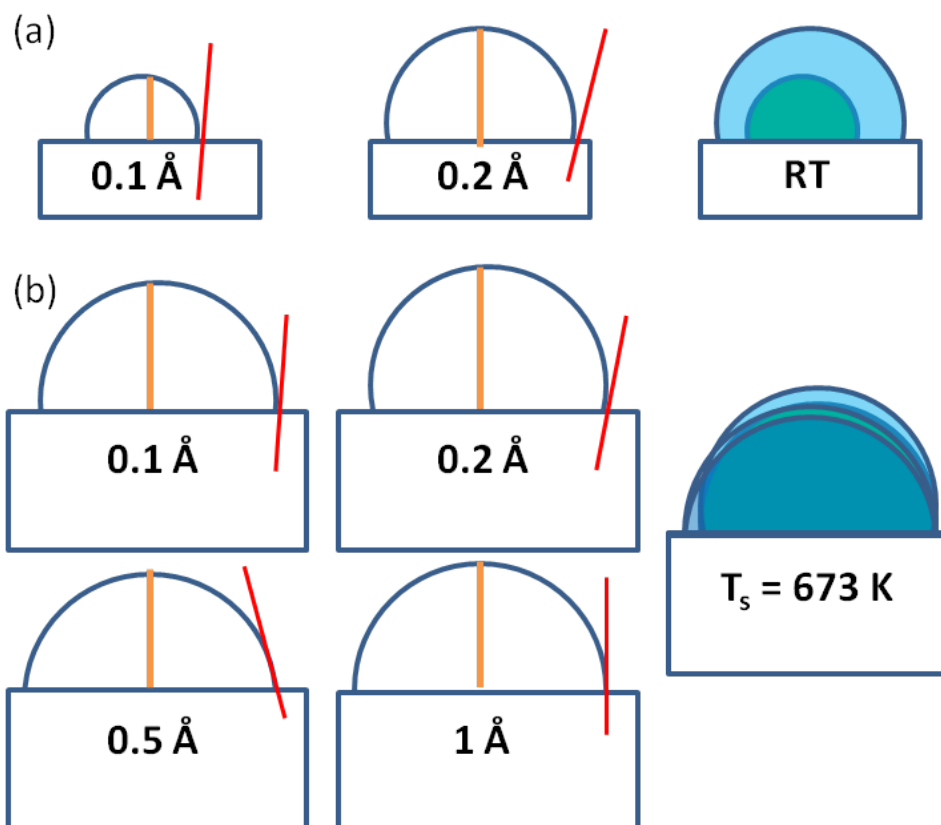


Figure 4.40: Scale schematic representation of Ag NPs growth on ZnO. (a) 0.1 and 0.2 Å Ag deposited at RT, (b) 0.1 - 1 Å Ag deposited with substrate temperature kept at 673 K.

XPS analysis

For a deeper understanding of the investigated NP properties XPS measurements have been performed. A good parameter to evaluate the amount of material deposited is equivalent thickness, which is total thickness of deposited material if it formed a continuous film on the substrate. Equivalent thickness was calculated by exponential attenuation model, considering intensity ratio between Ag3d and Zn2p peaks. For equal nominal thickness, the amount of detected silver is higher for RT deposited clusters, which show a higher sticking coefficient with respect to the ones deposited at higher temperature.

0.2 Å deposited at RT shows a strong shift to lower binding energies (~ 0.4 eV) of Ag3d with respect to 0.1 Å sample, which can be ascribed to surface effects: due to the bigger particle size the hole in core level is more efficiently screened, leading to a shift of lower BE of core Ag peak. A similar, but weaker effect is also observable for NP grown at 673 K: a maximum shift of 0.19 eV from 0.1 Å to 1 Å is reported, confirming that particle size experience only very small or negligible increase.

4.3.2 The role of temperature

The role of temperature and its effect on NP properties has been checked not only by using different deposition temperatures, but also by performing temperature treatments. In this case 0.2 Å nominal thickness has been chosen and RT deposited NPs have been subsequently annealed at different temperatures (673 K, 873 K and 1273 K) to determine how this affects morphology and, consequently, plasmonic properties.

STM images for the different preparations are shown in Fig.4.41, where also 673 K deposited NPs are shown. The main effect of annealing on cluster morphology is to decrease density due to desorption of material, which was also confirmed by quantitative analysis by XPS. After annealing at 1273 K (STM image not shown here) very few clusters remain on the surface, as testified by the almost complete disappearance of plasmonic peak (Fig.4.42). LSPRs parallel and perpendicular modes are respectively red- and blueshifted with increasing annealing temperature (Fig.4.42).

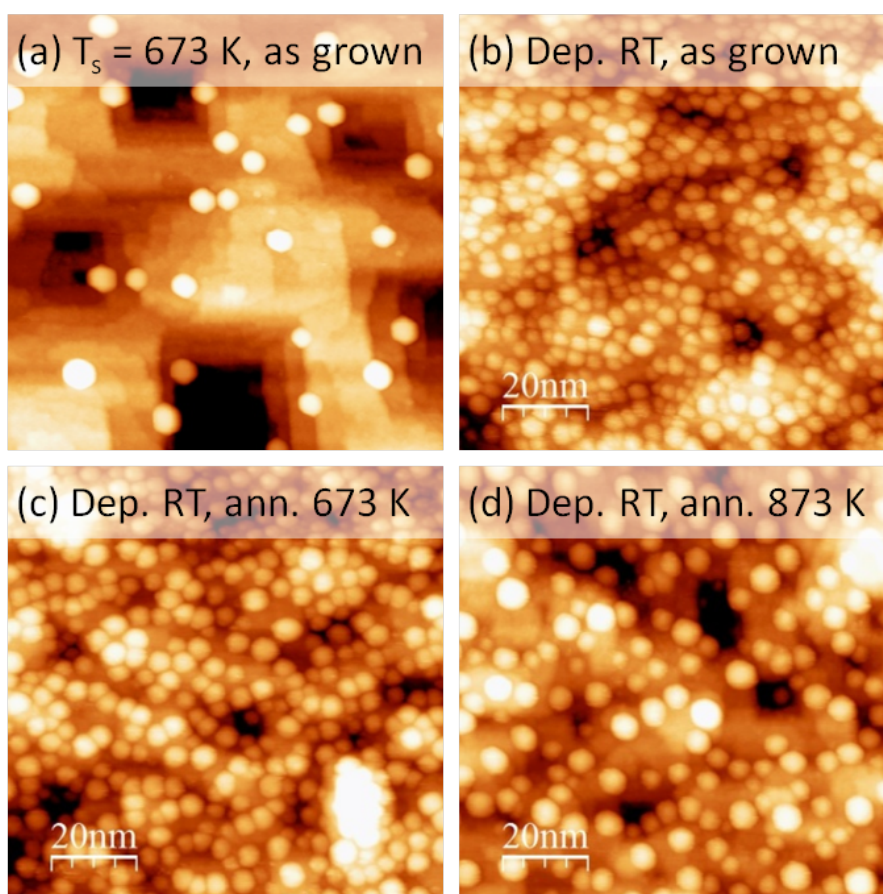


Figure 4.41: (100×100) nm² STM images for 0.2 Å Ag/ZnO. (a) Silver deposited at 673 K, as grown (2 V, 0.05 nA); (b) silver deposited at RT, as grown (3 V, 0.04 nA), (c) after annealing at 673 K (3.2 V, 0.04 nA) and (d) after annealing at 873 K (3 V, 0.04 nA).

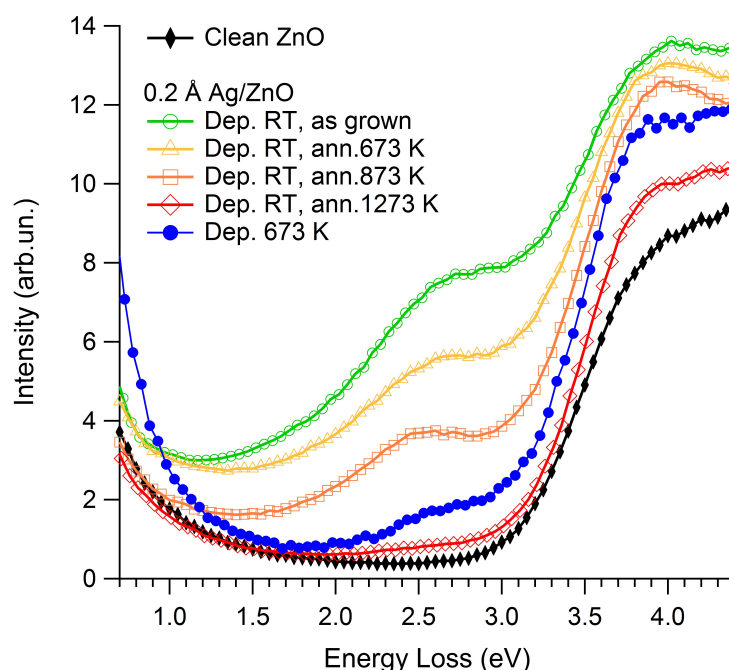


Figure 4.42: EELS spectra for 0.2 Å Ag/ZnO with silver deposited at 673 K, as grown, silver deposited at RT, as grown, after annealing at 673 K, 873 K and 1273 K. For the sake of clarity, the spectra have been vertically shifted with respect of each other.

Fig.4.43 reports simulation results, where NPs are best modeled as truncated spherical particles. Annealing induces in this case a slight increase in particle diameter without affecting height, thus clusters are both bigger and with higher aspect ratio, getting close to 2 (semisphere). The increasing size induces redshift of parallel mode, while blueshift of perpendicular one can be explained both in terms of interaction and particle shape. Both the increasing coverage and consequent higher interaction and the aspect ratio approaching 2 value should lead to a higher energy difference between peaks with redshift of parallel mode and blueshift of perpendicular one. Since the effect of interaction has been reported as negligible in the previous analysis, it seems more reasonable to attribute the increasing modes splitting to shape effect, even if it is not possible to disentangle the two contributions in this case.

| <i>Prep.</i> | n_C (m^{-2}) | <i>Cov</i> (%) | d_{STM} (nm) | h_{STM} (nm) | d_{sim} (nm) | E_{par} (eV) | E_{per} (eV) | $E_{per} - E_{par}$ (eV) |
|--------------|-----------------------|-------------------|-------------------|-------------------|-------------------|-------------------|-------------------|-----------------------------|
| As grown | 5.6×10^{16} | 90 | 4.0 ± 0.6 | 1.5 ± 0.8 | 1.3 | 2.73 | 3.73 | 1.00 |
| Ann. 673 K | 3.6×10^{16} | 80 | 4.3 ± 0.9 | 1.5 ± 0.9 | 1.4 | 2.61 | 3.76 | 1.15 |
| Ann. 873 K | 2.6×10^{16} | 30 | 4.7 ± 0.7 | 1.5 ± 0.8 | 1.5 | 2.51 | 3.80 | 1.29 |

Table 4.10: Morphological parameters and plasmonic peak energy of 0.2 Å Ag/ZnO as determined by STM and EELS analysis for the different preparations.

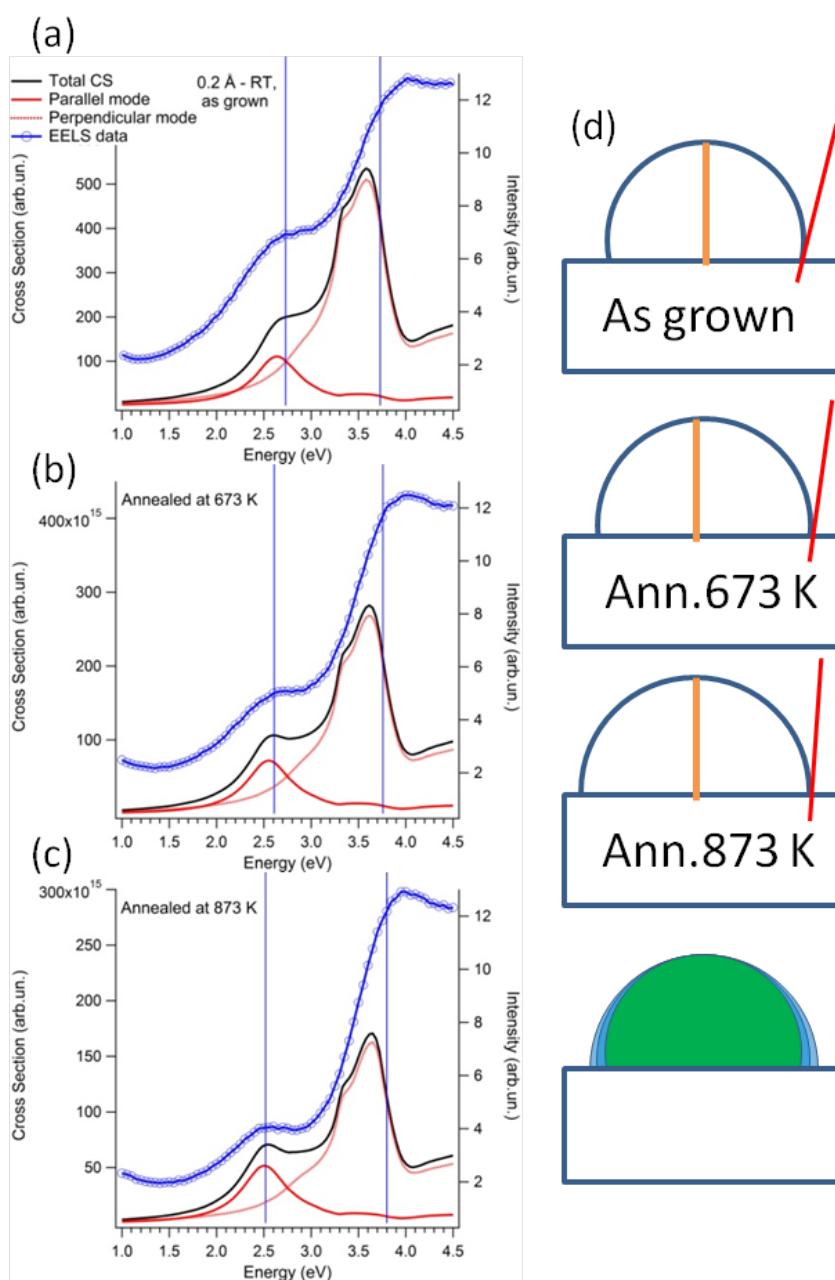


Figure 4.43: 0.2 Å Ag/ZnO. (a-c) EELS spectra and simulations for spherical particle shape. Blue vertical lines indicate peak energy as determined by fitting experimental data. (d) Corresponding scale schematical representation.

Ag3d XPS peak confirms the hypothesis of increasing NP size with annealing: a shift to lower binding energy related to surface effects is observed with increasing annealing temperature, equal to 0.1 eV between each subsequent preparation and the previous state, reaching a total shift of about 0.3 eV from as grown to 1273 K annealed sample.

4.4 Conclusions

Ag NP have been deposited by MBE on three different oxides, with different exposed crystal planes and different bandgaps, analysing clusters growth and how it affects material properties.

Ag/ZrO₂ system was chosen as a case study to determine morphology and crystal structure by STM and the developed method has been applied to analyze Ag/MgO and Ag/ZnO, where information on NPs properties in terms of size, shape and distribution have been refined by means of the simulation of the optical response of the system and have been related to plasmonic response.

Silver grows epitaxially on the oxide surface, exposing the most suitable surface depending on the lattice mismatch: while the growth on the square (001) is favoured on the cubic MgO(001) substrate, on hexagonal ZrO₂(0001) triangular (111) plane is preferred, as on the rectangular ZnO(10 $\bar{1}$ 0). Independently from the underlying lattice, when dislocations or generally irregularity like terraces borders are present on the substrate surface, silver deposited on MgO and ZrO₂ at RT chooses these lines as preferential sites for adsorption at low coverage, while in ZnO case this happens only for clusters deposited at higher temperature (673 K). When the amount of material increases approaching full coverage, the distribution is homogenous even if not ordered in all cases. Clusters grow in Volmer-Webber mode, increasing more in size than in number. An exception is represented by 673 K deposited Ag on ZnO: in this case dimensions remain almost constant while only cluster density increases with increasing amount of deposited material. Very small or negligible effect of temperature treatment up to 673 K has been reported on the three oxide for nominal thickness lower than 2 Å, which testifies the high stability of silver NPs in this temperature range. On the contrary, substantial differences in morphology have been observed for clusters deposited at 673 K with respect to the one grown at RT on ZnO.

It has been reported that adhesion increases with narrowing of the band gap, thus, NPs with lower contact angle are expected to grow on a more insulating material, due to the lower adhesion [26]. Comparing the three different oxides in study this adhesion trend as a function of bandgap does not seem to be verified. Comparing STM data, aspect ratio in all three cases is between 2 and 3.5 without any well defined trend. Calculated contact angle for Ag on MgO and ZnO, whose band gap differs by more than 4 eV, ranges in both cases between 95° and 105°, corresponding to NPs with truncated spherical shape, close to perfect semispheres. Thus, for Ag on these oxides, a similar adhesion can be related to a similar concentration of surface defects, which has also been reported as a relevant factor in NPs wetting the substrate surface [26].

The possibility to compare different oxides has shown the effects on plasmonic properties: first through morphology, but also by dielectric coupling. Thanks to the choice of different substrate and preparation conditions, which leads to different morphologies, the effect of some of the parameters has been partially disentangled from the others. In the case of Ag deposited on ZnO at 673 K, where particle size remained rather constant even increasing nominal thickness, it has been possible to directly measure the effect of shape and conclude that, at fixed dimensions, even a small aspect ratio increase lead to a significant peak shift. This shift is however small if compared with size-related one, thus when aspect ratio variations are less than 0.5, their effect is negligible when compared to the dimensions increase. Comparing Ag/MgO and Ag/ZnO it has been possible to exclude a significant contribution of interaction, concluding that the low shift observed for perpendicular mode is more likely related to the nature of the optical response than to NPs distribution.

A significant role has been reported to be played by the dielectric coupling between metal and oxide: the higher dielectric function of ZnO (~ 3.6 - 3.7 eV [5]) with respect to MgO one (~ 3 eV) leads to a redshift of the parallel mode. Considering 0.1 \AA Ag deposited at RT, plasmonic parallel mode suffers a 0.4 eV redshift in Ag/ZnO case with respect to Ag/MgO system, while perpendicular mode energy results unchanged.

Last but not least, beside the significant results on phenomena and mechanism involved, this study has proved the development of a reliable method to determine morphological parameters of NPs, starting from STM images and fitting morphological parameters in a model simulation looking for best match with experimental EELS data. The comparison between different techniques through the presented procedure has allowed to obtain a complete and accurate picture of NPs growth on the oxide, which takes into account and integrates all the available data concerning different properties.

Conclusions

In this work different systems with ZnO coupled to various metals in different forms have been prepared and analyzed. The effect of metal-oxide coupling has been investigated with various techniques, studying the fundamental mechanisms involved and the relevant properties in each case.

ZnO thin films have been grown on a Mo(001) substrate and composition, defectivity and crystalline structure have been investigated. Film growth has been modeled from first stages, determining the role of deposition parameters. Oxidation, which is not complete for thickness higher than 10 Å can be improved by temperature treatments or increasing the oxygen-to-zinc ratio during deposition. Mo substrate plays an active role in Zn oxidation, acting as an oxygen reservoir. A high presence of defects has been observed, related to structural deformations. Morphology is strongly influenced by deposition conditions, resulting completely different when different parameters are set, ranging from an irregular continuous film to the formation of peculiar nanostructured islands. These results improve the knowledge on the material, which is fundamental for a better comprehension of the nanostructures which find application in many field, especially in solar energy conversion.

In the second part of the study, metal has been coupled to ZnO as a dopant. Al-doped ZnO thin films prepared by magnetron sputtering have been fully characterized in a wide doping range to obtain a complete picture of the system. Best performances as TCO, in terms of electrical and optical properties, have been determined for 3.6 at.% Al content, realizing high quality films with low resistivity ($6 \times 10^{-4} \Omega \text{ cm}$) and high transmittance (>85%). High performances of AZO as an alternative plasmonic material have been probed by IR technique: low losses ($\epsilon_2 < 8$) and a lower absolute value for real part of dielectric function with respect to Ag have been measured. The origin of material conductivity has been deeply investigated. The analysis of electronic properties by XPS and HAXPES measurements has allowed to determine which one of the two proposed models is the more suitable to describe AZO behavior, clearly assigning the best description of material conductivity to conduction band filling by donor dopant electrons. The fundamental role of defects in determining the electronic properties of the material has also been highlighted.

Finally, Ag NPs have been deposited on a ZnO bulk crystal in different conditions, to analyze morphological and plasmonic properties and their inter-relation. A method to analyze STM images and to determine morphology in a reliable way has been developed by using Ag/ZrO₂ as a case study. The acquired skills has been applied to the analysis of Ag/ZnO and Ag/MgO systems, the latter chosen as a prototypical model system to be compared to ZnO one and to gain a deeper insight on the substrate role. The analysis has been performed both with STM and EELS techniques, whose results have been integrated with a simulation of the optical response, which has allowed a more accurate determination of particle geometry and distribution. Ag NPs growth has been modeled from the first stages and the dependence of plasmonic properties on the single parameters has been discussed. The role of the substrate, acting on one hand by conditioning Ag clusters size, shape and distribution, and on the other hand by introducing a different dielectric coupling with the metal, has been deeply investigated.

This study is relevant not only for the significant results on fundamental physical processes and properties, but also for the development of reliable methods and procedures which integrate different techniques and allows to obtain a complete picture of the involved system in terms of different properties.

Bibliography

- [1] *National Renewable Energy Laboratory (NREL)* - [http : //www.nrel.gov](http://www.nrel.gov).
- [2] M. Grätzel. *Inorg. Chem.*, 44:6841–6851, 2005.
- [3] M. A. Green, K. Emery, D. L. King, Y. Hishikawa, and W. Warta. *Prog. Photo-vol.:Res.Appl.*, 14:455–461, 2006.
- [4] J. Burschka, N. Pellet, S.-J. Moon, R. Humphry-Baker, P. Gao, M. K. Nazeeruddin, and M. Grätzel. *Nature*, 499:316–320, 2013.
- [5] Ü. Özgür, Ya. I. Alivov, C. Liu, A. Teke, M. A. Reshchikov, S. Doğan, V. Avrutin, S.-J. Cho, and H. Morkoç. *J.Appl.Phys.*, 98(041301):1–103, 2005.
- [6] T. Minami, H. Sato, H. Nanto, and S. Takata. *Jpn. J. Appl. Phys.*, 24(10):L781–L784, 1985.
- [7] O. Dulub, L. A. Boatner, and U. Diebold. *Surf. Sci.*, 519:201–217, 2002.
- [8] A. A. Ashrafi, A. Ueta, H. Kumano, and I. Suemune. *J. Cryst. Growth*, 221:435–439, 2000.
- [9] U. Diebold, L. V. Koplitz, and O. Dulub. *Appl. Surf. Sci.*, 237:336–342, 2004.
- [10] G. Kresse, O. Dulub, and U. Diebold. *Phys. Rev. B*, 68(245409):1–15, 2003.
- [11] C. Noguera. *J. Phys.: Condens. Matter*, 12(R367), 2000.
- [12] T. Becker, S. Hovel, M. Kunat, C. Boas, U. Burghaus, and C.Wöll. *Surf. Sci.*, 486:L502.
- [13] N. Jedrecy, M. Sauvage-Simkin, and R. Pinchaux. *Appl. Surf. Sci.*, 69:162–163, 2000.
- [14] O. Dulub, U. Diebold, and G. Kresse. *Phys. Rev. Lett.*, 90(1):016102–1–4, 2003.
- [15] M. Kunat, S. G. Girol, T. Becker, U. Burghaus, and C.Wöll. *Phys. Rev. B*, 66(081402), 2002.

- [16] J.-M. Chauveau, D. A. Buella, M. Laugt, P. Vennegues, M. Teisseire-Doninelli, S. Berard-Bergery, C. Deparis, B. Lo, B. Vinter, and C. Morhain. *J. Cryst. Growth*, 366:301–302, 2007.
- [17] C. Chen, V. Adivarahan, J. Yang, M. Shatalov, E. Kuokstis, and M. A. Khan. *Jpn. J. Appl. Phys.*, 1039:42, 2003.
- [18] J. B. Baxter, A. M. Walker, K. van Ommerring, and E. S. Aydil. *Nanotechnology*, 17:S304, 2006.
- [19] T. M. Parker, N. G. Condon, R. Lindsay, F. M. Liebsle, and G. Thornton. *Surf. Sci.*, 415:L1046, 1998.
- [20] U. Kreibig and W. Vollmer. *Optical Properties of Metal Clusters*, volume 25. Springer Series Material Science, 1995.
- [21] S.A. Maier and H.A. Atwater. *J. Appl. Phys.*, 98(1):011101 1–10, 2005.
- [22] G. Mie. *Annalen der Physik*, 330(3):377–445, 1908.
- [23] I. Simonsen, R. Lazzari, J. Jupille, and S. Roux. *Phys. Rev. B*, 61(1):7722–7733, 2000.
- [24] R. Lazzari, J. Jupille, and J.-M. Layet. *Phys. Rev. B*, 68(4):045428 1–11, 2003.
- [25] A. Liebsch. *Phys. Rev. B*, 48(15):11317–11328, 1993.
- [26] F. Didier and J. Jupille. *J. Adhes.*, 58(3-4):253–261, 1996.
- [27] K. Watanabe, D. Menzel, N. Nilius, and H.-J. Freund. *Chem. Rev.*, 106(10):4301–4320, 2006.
- [28] H. A. Atwater and A. Polman. *Nat. Mater.*, 9(3):205–213, 2010.
- [29] M. D. Brown, T. Suteewong, R. S. S. Kumar, V. D’Innocenzo, A. Petrozza, M. M. Lee, U. Wiesner, and H. J. Snaith. *Nano Lett.*, 11(2):446–454, 2010.
- [30] C. Hägglund, M. Zäch, and B. Kasemo. *Appl. Phys. Lett.*, 92(1):013113 1–3, 2008.
- [31] D. H. Lee, J. Y. Kwon, S. Maldonado, A. Tuteja, and A. Boukai. *Nano Lett.*, 14(4):1961–1967, 2014.
- [32] S. Pillai, K. R. Catchpole, T. Trupke, and M. A. Green. *J. Appl. Phys.*, 101(9):093105 1–8, 2007.
- [33] Q. Zhang, Y. N. Tan, J. Xie, and J. Y. Lee. *Plasmonics*, 4(1):9–22, 2009.

-
- [34] M. Rocca. *Surf. Sci. Rep.*, 22:1–71, 1995.
- [35] C. Tusche, H. L. Meyerheim, and J. Kirschner. *Phys. Rev. Lett.*, 99(026102), 2007.
- [36] G. Weirum, G. Barcaro, A. Fortunelli, F. Weber, R. Schennach, S. Surnev, and F. P. Netzer. *J. Phys. Chem. C*, 114(15432), 2010.
- [37] H. Gabasch, A. Knop-Gericke, R. Schlögl, S. Penner, B. Jenewein, K. Hayek, and B. Klötzer. *J. Phys. Chem. B*, 110:11391–11398, 2006.
- [38] F. Stavale, L. Pascua, N. Nilius, and H.-J. Freund. *J. Phys. Chem. C*, 117(10552), 2013.
- [39] Y. Chen, H. Ko, S. Hong, and T. Yao. *Appl. Phys. Lett.*, 76:559, 2000.
- [40] M. Xue, Q. Guo, K. Wu, and J. Guo. *Langmuir*, 24:8760, 2008.
- [41] F. Stavale, N. Nilius, and H.-J. Freund. *J. Phys. Chem. Lett.*, 4:3972–3976, 2013.
- [42] E. Cagin, J. Yang, W. Wang, J. D. Phillips, S. K. Hong, and J. Y. Lee J. W. Lee. *Appl. Phys. Lett.*, 92(233505), 2008.
- [43] M. Nistor, N. B. Mandache, J. Perrière, C. Hebert, F. Gherendi, and W. Seiler. *Thin Solid Films*, 519(3959), 2011.
- [44] H. Zhou, H.-Q. Wang, X.-X. Liao, Y. Zhang, J.-C. Zheng, J.-O. Wang, E. Muhammed, H.-J. Qian, K. Ibrahim, X. Chen, H. Zhan, and J. Kang. *Nanoscale Res. Lett.*, 7(184), 2012.
- [45] D. Kato, T. Matsui, and J. Yuhara. *Surf. Sci.*, 604(1283), 2010.
- [46] H. N. Kourouklis and R. M. Nix. *Surf. Sci.*, 318(104), 1994.
- [47] K. Zheng, Q. Guo, M. Xue, D. Guo, S. Liu, and E. G. Wang. *Thin Solid Films*, 515(7167), 2007.
- [48] D. Guo, M. Xue, Q. Guo, K. Wu, J. Guo, and E.G. Wang. *Appl. Surf. Sci.*, 255(9015), 2009.
- [49] P. Vennéguès, J. M. Chauveau, M. Korytov, C. Deparis, J. Zuniga-Perez, and C. Morhain. *J. Appl. Phys.*, 103(083525), 2008.
- [50] B. H. Lin, W.-R. Liu, C. Y. Lin, S. T. Hsu, S. Yang, C. C. Kuo, C.-H. Hsu, W. F. Hsieh, F. S.-S. Chien, and C. S. Chang. *ACS Appl. Mater. Interfaces*, 4(5333), 2012.
- [51] S. Benedetti, P. Luches, M. Liberati, and S. Valeri. *Surf. Sci.*, 572(2-3):L348–L354, 2004.

- [52] F. Oba, M. Choi, A. Togo, and I. Tanaka. *Sci. Technol. Adv. Mater.*, 12(3):034302 1–14, 2011.
- [53] M. Kuhn and J. A. Rodriguez. *Surf. Sci.*, 336(1), 1995.
- [54] I. Horcas, R. Fernandez, J.M. Gomez-Rodriguez, J. Colchero, J. Gomez-Herrero, and A. M. Baro. *Rev. Sci. Instrum.*, 78(1):013705 1–8, 2007.
- [55] S. Tanuma, C. J. Powell, and D. R. Penn. *Surf. Interface Anal.*, 21(3):165–176, 1994.
- [56] L. Z. Mezey and J. Giber. *Jpn. J. Appl. Phys.*, 21(11):1569–1571, 1982.
- [57] S.-H. Na and C.-H. Park. *J. Korean Phys. Soc.*, 56(1):498–502, 2010.
- [58] J.-C. Dupin, D. Gonbeau, P. Vinatier, and A. Levasseur. *Phys. Chem. Chem. Phys.*, 2(6):1319–1324, 2000.
- [59] T. Szörényi, L.D. Laude, I. Bertóti, Z. Kántor, and Zs. Geretovszky. *J. Appl. Phys.*, 78(10):6211–6219, 1995.
- [60] A. Janotti and C. G. Van de Walle. *Appl. Phys. Lett.*, 87(12):122102 1–3, 2005.
- [61] A. Janotti and C. G. Van de Walle. *Phys. Rev. B*, 76(16):165202 1–22, 2007.
- [62] PDF Card 00-036-1451 (ICDD).
- [63] L. N. Demianets, D. V. Kostomarov, I. P. Kuzmina, and S. V. Pushko. *Crystallogr. Rep.*, 47(1):S86–S98, 2002.
- [64] R. C. Wang, C. P. Liu, J. L. Huang, S.-J. Chen, Y.-K. Tseng, and S.-C. Kung. *Appl. Phys. Lett.*, 87(1):013110–013113, 2005.
- [65] H. Saarenpää, T. Niem, A. Tukiainen, H. Lemmetyinen, and N. Tkachenko. *Sol. Energy Mater. Sol. Cells*, 94(8):1379–1383, 2010.
- [66] J.-H. Park, K.-J. Ahn, K.-I. Park, S.-I. Na, and H.-K. Kim. *J. Phys. D: Appl. Phys.*, 43(115101):1–6, 2010.
- [67] D. Xu, Z. Deng, Y. Xu, J. Xiao, C. Liang, Z. Pei, and C. Sun. *Phys. Lett. A*, 346:148–152, 2005.
- [68] X. Jiang, F. L. Wong, M. K. Fung, and S. T. Lee. *Appl. Phys. Lett.*, 83:1875–1877, 2003.
- [69] Y. R. Park, E. Nam, J.-H. Boo, D. Jung, S. J. Suh, and Y. S. Kim. *Bull. Korean Chem. Soc.*, 28(12):2396–2400, 2007.

-
- [70] P. R. West, S. Ishii, G. V. Naik, N. K. Emani, V. M. Shalaev, and A. Boltasseva. *Laser Photonics Rev.*, 4(6):795–808, 2010.
- [71] A. Boltasseva and H. A. Atwater. *Science*, 331(6015):290–291, 2011.
- [72] D.-J. Yun and S.-W. Rhee. *Thin Solid Films*, 517(16):4644–4649, 2009.
- [73] T. Minami. *Semicond. Sci. Technol.*, 20(4):S35–S44, 2005.
- [74] Y. Sawada, C. Kobayashi, S. Seki, and H. Funakubo. *Thin Solid Films*, 409(1):46–50, 2002.
- [75] A. Suzuki, T. Matsushita, T. Aoki, A. Mori, and M. Okuda. *Thin Solid Films*, 411(1):23–27, 2002.
- [76] S. C. Gong, Y.-J. Choi, H. Kim, C.-S. Park, H.-H. Park, J. G. Jang, H. J. Chang, and G. Y. Yeom. *J. Vac. Sci. Technol. A*, 31(1):01A101 1–6, 2013.
- [77] J. G. Lu, Z. Z. Ye, Y. J. Zeng, L. P. Zhu, L. Wang, J. Yuan, B. H. Zhao, and Q. L. Liang. *J. Appl. Phys.*, 100(073714):1–11, 2006.
- [78] C. E. Kim, P. Moon, I. Yun, S. Kim, J.-M. Myoung, H. W. Jang, and J. Bang. *Expert Sys. Applic.*, 38(3):2823–2827, 2011.
- [79] R. E. I. Schropp and A. Madan. *J. Appl. Phys.*, 66(5):2027–2031, 1989.
- [80] Z.C. Jin, I. Hamberg, , and C. G. Granqvist. *J. Appl. Phys.*, 64(10):5117–5131, 1988.
- [81] A. Le Donne L. Ciontea S. Binetti R. A. Mereu, S. Marchionna and M. Acciarri. *Phys. Status Solidi C*, 11(9-10):1464–1467, 2014.
- [82] J. C. Lee, K. H. Kang, S. K. Kim, K. H. Yoon, I J. Park, and J. Song. *Sol. Energy Mater. Sol. Cells*, 64:185–195, 2000.
- [83] B. E. Sernelius, K.-F. Berggren, Z.-C. Jin, I. Hamberg, and C. G. Granqvist. *Phys. Rev. B*, 37(17):10244–10248, 1988.
- [84] K. C. Park, D. Y. Ma, and K. H. Kim. *Thin Solid Films*, 305(1):201–209, 1997.
- [85] S. H. Jeong, B. N. Park, D.-G. Yoo, and J.-H. Boo. *Journal of the Korean Physical Society*, 50(3):622–625, 2007.
- [86] Y. Ma, G. T. Du, S. R. Yang, Z. T. Li, B. J. Zhao, X. T. Yang, T. P. Yang, Y. T. Zhang, and D. L. Liu. *J. Appl. Phys.*, 95(11):6268–6272, 2004.

BIBLIOGRAPHY

- [87] H. Mondragón-Suárez, A. Maldonado, M. de la L. Olvera, A. Reyes, R. Castanedo-Pérez, G. Torres-Delgado, and R. Asomoza. *Appl. Surf. Sci.*, 193(1):52–59, 2002.
- [88] M. Gabás, S. Gota, J. R. Ramon-Barrado, M. Sánchez, N. T. Barrett, J. Avila, and M. Sacchi. *Appl. Phys. Lett.*, 86, 042104(4):042104–1, 2005.
- [89] M. Gabás, N. T. Barrett, J. R. Ramon-Barrado, S. Gota, T. C. Rojas, and M. C. López-Escalante. *Sol. Energy Mater. Sol. Cells*, 93(8):1356–1365, 2009.
- [90] H. H.-C. Lai, T. Basheer, V. L. Kuznetsov, R. G. Egdell, R. M. J. Jacobs, M. Pepper, and P. P. Edwards. *J. Appl. Phys.*, 112(8):083708 1–5, 2012.
- [91] B. Li, Y. Adachi, J. Li, H. Okushi, I. Sakaguchi, S. Ueda, H. Yoshikawa, Y. Yamashita, S. Senju, K. Kobayashi, M. Sumiya, H. Haneda, and N. Ohashi. *Appl. Phys. Lett.*, 98, 082101 (2011)(8):082101 1–3, 2011.
- [92] L. Gong, Z. Ye, J. Lu, L. Zhu, J. Huang, X. Gu, and B. Zhao. *Vacuum*, 84(7):947–952, 2010.
- [93] H. Kim, A. Piqué, J. S. Horwitz, H. Murata, Z. H. Kafafi, C.M. Gilmore, and D. B. Chrisey. *Thin Solid Films*, 377-378:798–802, 2000.
- [94] P. Gondoni, M. Ghidelli, F. Di Fonzo, V. Russo, P. Bruno, J. Martí-Rujas, C. E. Bottani, A. Li Bassi, and C. S. Casari. *Thin Solid Films*, 520(14):4707–4711, 2012.
- [95] P. Gondoni, M. Ghidelli, F. Di Fonzo, M. Carminati, V. Russo, C. E. Bottani, A. Li Bassi, and C. S. Casari. *Nanotechnology*, 23:365706 1–8, 2012.
- [96] P. Palacios, K. Sánchez, and P. Wahnón. *Thin Solid Films*, 517(7):2448–2451, 2009.
- [97] M. Bazzani, A. Neroni, A. Calzolari, and A. Catellani. *Appl. Phys. Lett.*, 98:121907 1–3, 2011.
- [98] M. Gabás, P. Torelli, N. T. Barrett, M. Sacchi, F. Bruneval, Y. Cui, L. Simonelli, P. Díaz-Carrasco, and J. R. Ramos Barrado. *Phys. Rev. B*, 84:153303 1–4, 2011.
- [99] S. Lany and A. Zunger. *Phys. Rev. Lett.*, 98:045501 1–4, 2007.
- [100] E. Burstein. *Phys. Rev.*, 93:632–633, 1954.
- [101] T. S. Moss. *Proc. Phys. Soc.*, 67(10):775, 1954.
- [102] M. Sacchi, F. Offi, P. Torelli, A. Fondacaro, C. Spezzani, M. Cautero, G. Cautero, S. Huotari, M. Grioni, R. Delaunay, M. Fabrizioli, G. Vankó, G. Monaco, G. Paollicelli, G. Stefani, and G. Panaccione. *Phys. Rev. B*, 71:155117 1–8, 2005.

-
- [103] C. G. van de Walle. *Phys. Rev. Lett.*, 85(5):1012–1015, 2000.
- [104] L. E. Halliburton, N. C. Giles, N. Y. Garces, M. Luo, C. Xu, L. Bai, and L. A. Boatner. *Appl. Phys. Lett.*, 87(17):172108 1–3, 2005.
- [105] D. C. Look, G. C. Farlow, P. Reunchan, S. Limpijumnong, S. B. Zhang, and K. Nordlund. *Phys. Rev. Lett.*, 95(22):225502 1–4, 2005.
- [106] M. Sakamaki, N. Kawai, T. Miki, T. Kaneko, T. Konishi, T. Fujikawa, K. Amemiya, Y. Kitajima, Y. Kato, T. Muro, H. Yamauchi, and M. Sakai. *Phys. Rev. B*, 83(15):155210 1–7, 2011.
- [107] T. Minami, H. Nanto, and S. Takata. *Japan J. Appl. Phys.*, 23(5):L280–L282, 1984.
- [108] H. Agura, A. Suzuki, T. Matsushita, T. Aoki, and M. Okuda. *Thin Solid Films*, 445(2):263–267, 2003.
- [109] S. H. Park, S. E. Park, J. C. Lee, P. K. Song, and J. H. Lee. *Journal of the Korean Physical Society*, 54(3):1344–1347, 2009.
- [110] A. B. Kuzmenko. *Rev. Sci. Instrum.*, 76:083108 1–9, 2005.
- [111] D. Céolin, J.M. Ablett, D. Prieur, T. Moreno, J.-P. Rueff, T. Marchenko, L. Journal, R. Guillemin, B. Pilette, T. Marin, and M. Simon. *J. Electron Spectrosc. Relat. Phenom.*, 190(PART B):188–192, 2013.
- [112] J.-P. Rueff, J. Ablett, D. Céolin, D. Prieur, T. Moreno, V. Balédent, B. Lassalle-Kaiser, J. Rault, M. Simon, and A. Shukla. *Journal of Synchrotron Radiation*, 2014. to be published.
- [113] N. W. Ritchie. *Microsc. Microanal.*, 15(05):454–468, 2009.
- [114] F. Wooten. *Optical Properties of Solids*. Academic Press, New York, 1972.
- [115] M. Dressel and G. Grüner. *Electrodynamics of Solids*. Cambridge University Press, 2002.
- [116] S. H. Jeong, J. W. Lee, S. B. Lee, and J. H. Boo. *Thin Solid Films*, 435(1-2):78–82, 2003.
- [117] G. Haacke. *J. Appl. Phys.*, 47(9):4086–4089, 1976.
- [118] V. K. Jain and A. P. Kulshreshtha. *Sol. Energy Mater.*, 4:151–158, 1981.
- [119] A. C. Thompson and D. Vaughan. *X-ray data booklet*. Lawrence Berkeley Laboratory, 2001.

- [120] A. Walsh, J. L. F. Da Silva, S.-H. Wei, C. Körber, A. Klein, L. F. J. Piper, A. De Masi, K. E. Smith, G. Panaccione, P. Torelli, D. J. Payne, A. Bourlange, and R. G. Egdell. *Phys. Rev. Lett.*, 100(16):167402 1–4, 2008.
- [121] C. Körber, V. Krishnakumar, A. Klein, G. Panaccione, P. Torelli, A. Walsh, J. L. F. Da Silva, S.-H. Wei, R. G. Egdell, and D. J. Payne. *Phys. Rev. B*, 81(16):165207 1–9, 2010.
- [122] G. V. Naik, V. M. Shalaev, and A. Boltasseva. *Adv. Mat.*, 25(24):3264–3294, 2013.
- [123] G. V. Naik, J. Kim, and A. Boltasseva. *Optical Materials Express*, 1(6):1090–1099, 2011.
- [124] G. V. Naik, J. Liu, A. V. Kildishev, V. M. Shalaev, and A. Boltasseva. *Proc. Natl. Acad. Sci. U. S. A.*, 109(23):8834–8838, 2011.
- [125] J. Kim, G. V. Naik, N. K. Emani, U. Guler, and A. Boltasseva. *IEEE Journal of Selected Topics in Quantum Electronics*, 19(3):4601907 1–7, 2013.
- [126] A. M. Hofmeister, E. Keppel, and A. K. Speck. *Mon. Not. R. Astron. Soc.*, 345:16–38, 2003.
- [127] D. L. Young, T. J. Coutts, V. I. Kaydanov, A. S. Gilmore, and W. P. Mulligan. *J. Vac. Sci. Technol. A*, 18:2978–2985, 2000.
- [128] A. Calzolari, A. Ruini, and A. Catellani. *ACS Photonics*, 1(8):703–709, 2014.
- [129] R. Lazzari, J. Jupille, and Y. Borensztein. *Appl. Surf. Sci.*, 142(1-4):451–454, 1999.
- [130] O. Robach, G. Renaud, and A. Barbier. *Phys. Rev. B*, 60(8):5858–5871, 1999.
- [131] R. Lazzari and I. Simonsen. *Thin Solid Films*, 419(1):124–136, 2002.
- [132] A. Barbier, G. Renaud, and J. Jupille. *Surf. Sci.*, 454-456:979–983, 2000.
- [133] R. Lazzari, I. Simonsen, D. Bedeaux, J. Vlieger, and J. Jupille. *Eur. Phys. J. B*, 24(2):267–284, 2001.
- [134] R. Lazzari, G. Renaud, C. Revenant, J. Jupille, and Y. Borensztein. *Phys. Rev. B*, 79(12):125428 1–8, 2009.
- [135] C. Revenant, G. Renaud, R. Lazzari, and J. Jupille. *Phys. Rev. B*, 79(23):235424 1–10, 2009.
- [136] R. Lazzari, J. Jupille, R. Cavallotti, and I. Simonsen. *J. Phys. Chem. C*, 118(13):7032–7048, 2014.

- [137] R. Lazzari and J. Jupille. *Surf. Sci.*, 482-485(part 2):823–828, 2001.
- [138] N. Jedrecy, G. Renaud, R. Lazzari, and J. Jupille. *Phys. Rev. B*, 72(4):045430 1–14, 2005.
- [139] M. Antlanger, W. Mayr-Schmölzer, J. Pavelec, F. Mittendorfer, J. Redinger, P. Varga, U. Diebold, and M. Schmid. *Phys. Rev. B*, 86(3):035451 1–9, 2012.
- [140] R. T. Tom, A. Sreekumaran Nair, N. Singh, M. Aslam, C. L. Nagendra, R. Philip, K. Vijayamohanan, and T. Pradeep. *Langmuir*, 19(8):3439–3445, 2003.
- [141] R. Grau-Crespo, N. Cruz Hernández, J. F. Sanz, and N. H. de Leeuw. *J. Phys. Chem. C*, 111(28):10448–10454, 2007.
- [142] M. Kumar, C. S. S. Sandeep, G. Kumar, Y. K. Mishra, R. Philip, and G. B. Reddy. *Plasmonics*, 9:129–136, 2014.
- [143] C. A. Schneider, W. F. S. Rasband, and K. W. Eliceiri. *Nat. Methods*, 9(7):671–675, 2012.
- [144] *Image Metrology A/S - Software: SPIP 4.4.11.0 (2007)*.
- [145] E. Napetschnig, M. Schmid, and P. Varga. *Surf. Sci.*, 601(6):3233–3245, 2007.
- [146] D. Alloyeau, C. Mottet, and C. Ricolleau. *Nanocoalloys: Synthesis, Structure and Properties*. Springer Science & Business Media, 2012.
- [147] K. Højrup Hansen, T. Worren, E. Lægsgaard, F. Besenbacher, and I. Stensgaard. *Surf. Sci.*, 475(1-3):96–102, 2001.
- [148] W. Hebenstreit, J. Redinger, Z. Horozova, M. Schmid, R. Podloucky, and P. Varga. *Surf. Sci.*, 424(2-3):L321–L328, 1999.
- [149] S. Degen, C. Becker, and K. Wandelt. *Faraday Discuss.*, 125:343, 2003.
- [150] G. Wulff. *Z. Kristallogr.*, 34:449–530, 1901.
- [151] L. Vitos, A. V. Ruban, H. L. Skriver, and J. Kollar. *Surf. Sci.*, 411:186–202, 1998.
- [152] P. Luches, F. Pagliuca, S. Valeri, F. Illas, G. Preda, and G. Pacchioni. *J. Phys. Chem. C*, 116(1):1122–1132, 2012.
- [153] S. Benedetti, P. Myrach, A. di Bona, S. Valeri, N. Nilius, and H.-J. Freund. *Phys. Rev. B*, 83(12):125423 1–10, 2011.
- [154] S. Benedetti, P. Torelli, S. Valeri, H. M. Benia, N. Nilius, and G. Renaud. *Phys. Rev. B*, 78(19):195411 1–8, 2008.

BIBLIOGRAPHY

- [155] H.M. Benia, P. Myrach, N. Nilius, and H.-J. Freund. *Surf. Sci.*, 604(3-4):435–441, 2010.
- [156] H.-M. Benia, P. Myrach, A. Gonchar, T. Risse, N. Nilius, and H.-J. Freund. *Phys. Rev. B*, 81(24):241415 1–4, 2010.
- [157] S. Benedetti, F. Stavale, S. Valeri, C. Noguera, H.-J. Freund, J. Goniakowski, and N. Nilius. *Adv. Funct. Mater.*, 23(1):75–80, 2013.
- [158] G. Renaud. *Surf. Sci. Rep.*, 32:1–90, 1998.
- [159] C. J. Powell and J. B. Swan. *Phys. Rev.*, 115(869), 1959.
- [160] H. Lüth. *Solid Surfaces, Interfaces and Thin Films - Fourth Edition*. Springer, 2001.
- [161] N. E. Christensen. *Phys. Stat. Sol. B*, 54:551–563, 1972.

Acknowledgements

I would like to thank, first of all, Prof. Sergio Valeri for giving me the opportunity to work in this interesting and challenging project and to directly participate to all the activities of the SESAMo research group.

A special thank goes to my direct supervisor, Dr. Stefania Benedetti, whose guide has been a fundamental contribution to all my scientific activities. She has been a constant presence and a reference point even in this particular moment of her life and for the third time I would like to thank her for her support, patience and precious advices.

I would like to acknowledge Dr. Paola Luches, for the help and support in every situation and for sharing her valuable experience.

I would also like to thank all the SESAMo and Superman research groups, with whom it was a pleasure to work.

I acknowledge Dr. Alessandro di Bona, whose high expertise in some of the technique used has been indispensable in the study of the ZnO films and Al-doped ZnO in particular.

I would like to thank Dr. Piero Torelli for the valuable involvement in Al-doped ZnO study, from the starting ideas to the practical realization of some of the experiments and the fundamental contribution to all the work.

I acknowledge SOLEIL and ELETTRA Synchrotron for provision of synchrotron radiation facilities. I would like to thank Dr. Denis Céolin for assistance in using Galaxies beamline (SOLEIL Synchrotron). I would also like to address a special thank to Dr. Andrea Perucchi and Dr. Paola Di Pietro for the assistance in using SISSI beamline (ELETTRA Synchrotron) and in analyzing IR data.

I acknowledge Prof. Michael Schmid and Dr. Joong-Il Jake Choi for the fundamental contribution in Ag/ZrO₂ experiments and data analysis, and Prof. Ulrike Diebold for the possibility to perform the three-months scientific visit at IAP laboratory at Vienna University of Technology, which as been a very formative experience not only from the scientific point of view. I would also like to thank all the staff at Vienna University of Technology.

I would like to thank Dr. Rémi Lazzari for the fundamental help and suggestions in using GranFilm software.

I acknowledge the FIRB project RBAP115AYN “Oxides at the nanoscale: multifunctionality and applications” and the COST ACTION CM1104 “Reducible oxide chemistry, structure and functions” for the financial support.

This work has been accomplished in the framework of the Global Grant Spinner 2013 and funded by the European Social Fund and the Emilia Romagna Region. I acknowledge Consorzio SPINNER, Regione Emilia Romagna and European Social Fund for the postgraduate fellowship.

Curriculum and list of publications

Personal Information

Ilaria Valenti

Place and date of birth: Scandiano (Reggio Emilia) - Italy, 27/02/1987

Current address: Via E. Montale, 21 - 41049 Sassuolo (Modena) - Italy

E-mail address: ilariavalenti@gmail.com

Education

January 2012 - December 2014: PhD in “Physics and Nano sciences” at the University of Modena and Reggio Emilia, Modena - Italy, in affiliation with CNR, Istituto Nanoscienze, S3, Modena – Italy

Selected for a postgraduate fellowship funded by Consorzio SPINNER, Regione Emilia Romagna and European Social Fund, within the project “Nanoscienze: Materiali e strategie emergenti per tecnologie sostenibili”, coordinator: Prof. Molinari Elisa.

July 2012: *International School of Solid State Physics, Materials for Renewable Energy*, Erice (Trapani) - Italy

November 2009 - October 2011: University of Modena and Reggio Emilia, Modena - Italy. Master’s Degree in Physics. Final Grade: 110/110 cum laude. Thesis discussed: “Analisi chimica e strutturale di cluster di Mg su MgO” (Chemical and structural analysis of Mg clusters on MgO), Supervisors: Prof. Sergio Valeri, Dr. Stefania Benedetti.

September 2006 - December 2009: University of Modena and Reggio Emilia, Modena - Italy. Bachelor Degree in Physics. Final Grade: 110/110 cum laude. Thesis discussed: “Ossidi nanostrutturati per il fotovoltaico: sistemi modello e sistemi reali” (Nanostructured oxides for photovoltaic technology: model and real systems), Supervisors: Prof. Sergio Valeri, Dr. Stefania Benedetti.

September 2001 - June 2006: Liceo “A. F. Formiggini”, Sassuolo (MO) - Italy. Scientific-linguistic High-school Diploma. Final mark: 100/100

Scientific activities

December 2013 and March 2014: One week visit to Elettra Synchrotron in Trieste to perform measurements and analysis on IR absorption at SISSI beamline.

January 2013 - April 2013: Three-months scientific stage activity with Surface Physics Group at the Institut für Angewandte Physik der Technische Universität Wien (Institute for Applied Physics of Vienna University of Technology), within the framework of COST CM1104 Action “Reducible oxide chemistry, structure and functions”, to study metal-oxide systems with applications in catalysis.

September 2011: Short period of stay in Grenoble at European Synchrotron Radiation Facility (ESRF) to participate at XAFS beam time. Proposal n. 08-01 921, titled: “Local atomic structure at the interface between cerium oxide and Pt(111)”.

May 2011 - October 2011: Scientific stage activity at SESAMo laboratory at University of Modena and Reggio Emilia to study nanostructured oxide systems with photovoltaics applications.

December 2009: Short visit to Fritz-Haber-Institut der Max-Planck-Gesellschaft in Berlin within the framework of the international research project in collaboration with Dr. N. Nilius and Professor H.-J. Freund, concerning metal/oxide systems with photocatalytic applications. Title of project: “Study and control of optical properties in clusters and thin films of silver and magnesium on oxides, oriented to photocatalytic and nanolithographic applications”.

May 2009 - September 2009: Scientific stage activity at SESAMo laboratory at University of Modena and Reggio Emilia to study Mg/MgO/Mo system.

Other activities

Teaching Assistant to the course “Istituzioni di Struttura della Materia” (Physics Bachelor Degree, Prof. F. Manghi). October - December 2012. October - December 2013.

Correlator assistant to Elisabetta Serpini’s Bachelor Degree Thesis (Relator: Prof. S.Valeri, Correlator: Dr. S. Benedetti), June - September 2012.

Correlator assistant to Anna Valentini’s Bachelor Degree Thesis (Relator: Prof. Sergio Valeri, Correlator: Dott. Stefania Benedetti), June - September 2013.

List of publications

S. Benedetti, N. Nilius, P. Myrach, I. Valenti, H. Freund, and S. Valeri, "Spontaneous Oxidation of Mg Atoms at Defect Sites in an MgO Surface", *J. Phys. Chem. C* 115: 3684-3687, 2011.

I. Valenti, S. Benedetti, A. di Bona, and S. Valeri, "Morphology, composition and structure of ZnO thin films on Mo(001)". Under review.

I. Valenti, S. Benedetti, A. di Bona, V. Lollobrigida, A. Perucchi, P. Di Pietro, S. Lupi, S. Valeri, and P. Torelli "Enlightening conductivity origin in Al-doped ZnO films". Under review.

Conferences participations and contributions

EMRS-Fall Meeting 2014, 15th - 18th of September 2014, Warsaw - Poland. "Unraveling conduction mechanism of Al-doped ZnO films", I. Valenti, S. Benedetti, P. Torelli, A. di Bona, S. Valeri (oral).

COST Action CM1104 WG1+WG2 meeting, 28th- 30th of April 2014, Zaragoza - Spain. "Growth and morphological analysis of Ag nanoclusters on ultrathin ZrO₂ films", I. Valenti, J.-I. J. Choi, U. Diebold, P. Luches, M. Schmid (poster).

FisMat 2013, 9th - 13th of September 2013, Milano - Italy. "ZnO nanostructured metal/oxide systems for solar energy conversion", I. Valenti, S. Benedetti, S. Valeri (oral).

EMRS-Spring Meeting 2013, 27th - 31st of May 2013, Strasbourg - France. "Nanostructured metal/ZnO systems for Dye-Sensitized Solar Cells", I. Valenti, S. Benedetti, S. Valeri (poster). Best poster presentation award for Symposium O: "Synthesis, processing and characterization of nanoscale multi functional oxide films IV".

International School of Solid State Physics, 56th Course: "Materials for Renewable Energy", 18th - 28th of July 2012, Erice, Trapani - Italy. "Nanostructured Oxides for Dye-Sensitized Solar Cells", I. Valenti, S. Benedetti, A. di Bona, E. Serpini, S. Valeri (poster)

Conferences contributions by coauthors

DPG Spring conference, 30th of March - 4th of April 2014, Dresden - Germany. “Metal nucleation and clusters on ultrathin ZrO₂ films”, J. I. J. Choi, I. Valenti, W. Mayr-Schmölzer, F. Mittendorfer, J. Redinger, U. Diebold, M. Schmid (oral).

ECOST 2nd general meeting, COST ACTION CM1104, 6th - 8th of November 2013, Uppsala - Sweden. “ZnO nanostructured metal/oxide systems for photocatalysis and photovoltaics”, S. Benedetti, I. Valenti, S. Valeri (poster).

ECOST first WG2 meeting, COST ACTION CM1104, 21st - 22nd of March 2013, Modena - Italy. “Oxide nanostructures for catalysis and photovoltaics”, S. Benedetti, I. Valenti, N. Nilius, and S. Valeri (oral).

FWF SFB F45 FOXSI PhD meeting, 18th - 22nd of March 2013, Hochkar - Austria. “Oxygen vacancies and water adsorption: STM studies on ultra-thin ZrO₂/Pt₃Zr(0001)”, J. I. J. Choi, I. Valenti, U. Diebold, M. Schmid, W. Mayr-Schmölzer, F. Mittendorfer, J. Redinger (oral).

DPG Spring conference, 10th - 15th of March 2013, Regensburg - Germany. “Water and atomic H adsorption on ultra-thin ZrO₂/Pt₃Zr(0001)”, J. I. J. Choi, I. Valenti, U. Diebold, M. Schmid, W. Mayr-Schmölzer, F. Mittendorfer, J. Redinger (oral).

NanotechItaly 2012, 21st - 22nd of November 2012, Venezia - Italy. “Oxide nanostructures for energy applications”, S. Benedetti, P. Luches, A. di Bona, S. D’Addato, I. Valenti, F. Pagliuca, E. Serpini, S. Valeri (oral).

1st workshop on photovoltaics: new frontiers and applications, 28th - 30th of September 2011, Lecce - Italy. “Metal/Oxide nanostructured systems for photovoltaic applications”, P. Luches, S. Benedetti, A. di Bona, S. D’Addato, I. Valenti, D. Pinotti, S. Lumetti, S. Valeri (poster).

ECOSS27, 29th of August - 3rd of September 2010, Groningen - The Netherlands. “Morphology and interface properties of metal clusters on MgO film for plasmonic applications”, S. Benedetti, I. Valenti, S. Altieri, S. Valeri (oral)

Scientific experiences and interests

Knowledge in using experimental techniques for manipulation and study of nanoscaled materials, analysis of chemical, structural and optical properties of nanostructures, surfaces and interfaces. Study of nanostructures and thin films growth in metal/oxide systems. Experience in preparation and treatments of single crystal and thin films in UHV conditions and low pressure ambient, Molecular Beam Epitaxy (MBE) and radiofrequency magnetron sputtering. Preparation of porous oxide films by paste sintering. Experience in Ultra-High Vacuum (UHV) systems and related techniques. Knowledge in using the following techniques: X-ray Photoemission Spectroscopy (XPS), Low-Energy Electron Diffraction (LEED), X-ray Photoelectron Diffraction (XPD), X-ray Powder Diffraction (XRPD), Scanning Tunneling Microscopy (STM), Auger Electron Spectroscopy (AES), Electron Energy Loss Spectroscopy (EELS), Infrared absorption spectroscopy, 4-point probes method and optical measurements. Experience in data analysis softwares: IGOR Pro, WSxM, ImageJ and GranFilm.

Languages and personal skills

Italian (mother-tongue)

Advanced level in English language. Trinity College London: Graded Examinations in Spoken English for speakers of other languages. Level C1.

Elementary knowledge of German and French languages. 5-years high school courses.

Expert user of MS Office and data analysis software (IGOR pro and WSxM)

University courses on Matlab, Fortran 95 and Java.

Ringraziamenti

In conclusione a questa tesi, voglio dedicare un momento a chi ha contribuito attivamente non solo alla qualità di questo lavoro, ma anche, e soprattutto, alla qualità della mia vita in questi 3 anni così intensi.

Innanzitutto grazie, di cuore, al Prof. Sergio Valeri per avermi dato la possibilità di lavorare in un contesto così stimolante ed interessante.

Grazie a Stefania, con la quale è stato un piacere lavorare ed il cui contributo è stato prezioso per la mia formazione personale, non meno che per il lavoro svolto. Grazie per la pazienza ed il supporto in questi quasi 4 anni di lavoro insieme.

Grazie alle persone con cui ho avuto occasione, per un motivo o per l'altro, di interagire lavorativamente e non, a tutti coloro che hanno dato un contributo o anche solo un consiglio. Grazie a Paola, Ale ed a tutto il gruppo SESAMo. Grazie ai miei vicini di ufficio, e compagni di (s)ventura. Grazie anche ai tecnici, il cui lavoro è fondamentale per quello di tutti noi.

Grazie a tutto il fantastico gruppo del pranzo, con cui abbiamo condiviso interessanti discussioni (quasi) mai lavorative, pranzi deluxe, file alla mensa e terribili quanto necessari caffè. Grazie soprattutto a Pesce, Alberto, Diego, Gufo ed Elisabetta. Grazie a Maria Chiara, che prima che una collega è un'amica, per i momenti a Milano, Londra, Modena e con la quale spero di dividerne ancora molti altri.

Grazie a chi mi ha fatto sorridere, a chi ha condiviso con me libri, film, mostre emozionanti, viaggi, caffè e cene, a chi mi ha dato qualcosa su cui riflettere, o aiutata a riconoscere un errore, chi non si è stancato di ascoltarmi anche se mi ripeto sempre. A chi è stato presente, in qualsiasi modo ne fosse capace. Grazie a Chiara, sempre eterna compagna di corso, non importa quanti anni ed oceani ci dividano. Grazie a Fabio ed Alberto, per il loro modo di affrontare la vita così differente e simile al mio. Grazie a Marta e Giulia per le conversazioni sempre stimolanti. Grazie a Martina, Federica, Francesca, per essere state così vicine, anche se lontane. Grazie ad Elisabetta, che è stata una presenza costante nella mia vita e nonostante questo mi sopporta ancora: grazie per non aver mai dubitato.

Ringrazio la mia famiglia, naturale ed acquisita, per il supporto che non è mai mancato, prima di tutti mia madre, che mi ha insegnato a volere sempre il massimo da me stessa ed ha sempre creduto che potessi ottenerlo.

Ad Alessandro, che più di ogni altro ha avuto cura di me, in ogni momento di buona o cattiva sorte, va il ringraziamento più importante. Grazie di tutto.

